

**Characterization of Dome Processes at Soufrière Hills Volcano, Montserrat:  
Synthesis of Infrared Remote Sensing Data with a Multi-parameter Database**

by

Sally Susan Kuhn

BS, University of Pittsburgh, 1997

Submitted to the Graduate Faculty of

Arts and Sciences in partial fulfillment

of the requirements for the degree of

Masters of Science

University of Pittsburgh

2003

UNIVERSITY OF PITTSBURGH  
FACULTY OF ARTS AND SCIENCES

This dissertation was presented

by

\_\_\_\_\_  
Sally Susan Kuhn

It was defended on

\_\_\_\_\_  
December 4, 2003

and approved by

\_\_\_\_\_  
Thomas Anderson

\_\_\_\_\_  
Ian Skilling

\_\_\_\_\_  
Michael Ramsey  
Dissertation Director



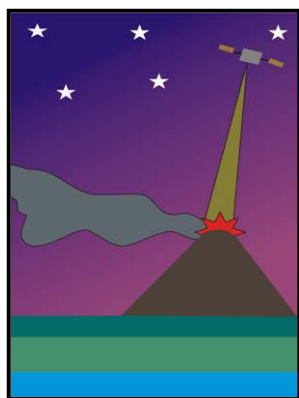
# **Characterization of Dome Processes at Soufrière Hills Volcano, Montserrat: Synthesis of Infrared Remote Sensing Data with a Multi-parameter Database**

**Sally S. Kuhn, M.S.**

**Department of Geology and Planetary Science  
University of Pittsburgh, 2003**

The Advanced Spaceborne Thermal Emission Reflectance Radiometer (ASTER) is a high resolution multispectral imager ideal for discerning physical variations on the active Soufrière Hills volcanic dome. Five band thermal infrared data at 90 meter spatial resolution can produce accurate temperature and emissivity data. These data can potentially provide information of glass and vesicle distribution across the changing dome, and therefore on internal processes. One cloud-free image is captured every three months on average, with increased frequency in 2002, where the volcano was a high priority target. Six nighttime ASTER scenes of the dome have been chosen based on coverage of the entire dome, the presence of thermal infrared anomalies, and pyroclastic flow activity, as well as a relative lack of cloud cover over the active dome. Montserrat Volcano Observatory (MVO) weekly reports from 1999 to present (available online) were also ingested into a multi-parameter, searchable database. These data, which detail specific volcanic activity, were compared against the ASTER data. The database fields include SO<sub>2</sub> flux, high temporal resolution weather satellite-derived radiance measurements, description of dome growth and collapse, and intensities of pyroclastic flows, rockfalls, fumarolic activity, and seismic activity. This database provides a unique cross-reference for the interpretation of the spaceborne data, as well as highlighting observable trends in each of the volcanic activity types. Results from this study will provide a better understanding of the capabilities of the ASTER instrument to accurately describe active dome processes and to characterize these and other processes statistically. This knowledge can be applied to other active areas to study potential indicators of volcanic activity, dome collapse, the generation of hazardous pyroclastic activity, as well as the transition from effusive dome growth to explosivity.

## Acknowledgements



Sometimes when I can't sleep, I think about what a fortunate person I am. In my life, I have been graced with an incredible family, incredible friends, and during the last two years, a terrific and supporting network of professors and instructors in the Department of Geology and Planetary Sciences at the University of Pittsburgh. There is no question in my mind that I would not be where I am today without these important people. I am a lucky girl.

First and foremost- **thank you** to my incredible parents, Dayle and George Kuhn, whom have stood by me, loved me, supported me, gave me money, kind words, encouragement, sympathy, back scratches, and tried **SO** hard to understand my project. I know no matter what I do next, I can count on you to be there. **Thank you** to my brother, Noah, for being excited for me at every turn. Thank you for the support, encouragement, and being the best brother a girl could have. To my grandparents, Bill and Esther Norris, **thank you**. Nobody else on this planet has grandparents like you. Thank you for teaching me, supporting me, and loving me so much that I can feel it even a million miles away. Thank you for being so generous. You are wonderful role models to everyone, young and old. Thank you grandma, for slipping me \$20's when grandpa isn't looking. (That won't stop just because I get a job, right?). Thank you to my Aunt Lynne and Uncle Jake Staton (my favorite aunt and uncle in Pittsburgh) for love and the incredible gift of school books as an undergrad. Thank you to my Aunt Winky and Uncle Don McQueen for love and supporting my "wild side".

My friends have been there for me above and beyond the call of duty....and believe me, I called on them a lot!! Tamara Misner (The Taminater) - I can say with confidence that I would not have made it through grad school without you!! Your patient and kindness is unmatched. Not only are you a smart and talented person, but you have been such a great and thoughtful friend. Thank you for making many long nights of hard work full of laughter. You've got the poster tube, right? ; ) Jessica Bluth, a.k.a. Schmessica. Again, I couldn't ask for a nicer friend. Thank you for keeping my pool game sharp and being in charge of the sharking! Thanks for being there and not ever letting me quit. To Dr. Kristine Coleman- thank you also for being a great friend beyond the call of duty. Not only do you listen to me rant for hours, but you stay awake and then answer me in coherent sentences!!!! (Wink wink.) You rock. Danielle Deemer, thank you. YOU are a quality person. Thanks for giving me kind words and little presents when

I needed it most. Sherry Stafford, you have been a great role model. You are kind and patient and made my life at school fun (and dirty ;)). How many other people would accompany me on a singles night at the shooting range? Thank you to Wandi Bruine de Bruin and Carolyn Fletcher for being wonderful friends and incredible people. Thank you, Wandi, for taking an interest in my academic ventures and coming to my boring talks! Thank you to my former boss, Dr. Judy Cameron, for teaching me how to be a scientist and a better person. (I am now fluent in monkey.) You are more than a boss, you are a friend. Matt Lamm and Robert Ferguson- thank you for not only thinking I would do great in grad school, but for thinking that I am capable of ruling the world if I wanted to! Beer and fish tacos have a whole new meaning to me. Thank you for plotting to blow up a west coast volcano so I would move out there to study it- what a super sweet plan!

Thank you to my advisor, Dr. Mike Ramsey, for providing me with such an incredible project, support to concentrate on it, and many, many, many opportunities. Thank you for leading the volcanology trip to Long Valley Caldera and vicinity in 2001, for this is what made me want to study volcanology. You set the bar high. I know you will miss your favorite student (me!!!). May pig whistles always be your friends.

Thank you to my committee members, Dr. Ian Skilling and Dr. Anderson (TA). Thank you for supporting and encouraging me. TA- you are also more than a committee member. You are never above the grad students that look up to you, and I thank you. Ian- thank you for not relentlessly making fun of me for almost getting swept out to sea in Hawaii. It was really mostly Jessica's fault anyway! Thank you for making things fun.

Thank you to the Department of Geology office staff- especially Dolly Chavez and Deanna Hitchcock for the continuous support and just for making my day brighter. Thank you to the department chair, Dr. Bill Harbert, for opportunities and most of all, believing in me.

Thank you to Tat Suki in the department of Statistics for many hours of help and advice with the statistical analysis of my database. Thank you Sonya Brady, also for database assistance.

## Table of Contents

<b>Section 1: Introduction .....</b>	<b>1</b>
<b>Section 2: Background .....</b>	<b>5</b>
2.1 Volcanology .....	5
2.1.1. Silicic Lava Domes .....	5
2.1.2. Soufrière Hills, Montserrat .....	10
i. Geologic Setting .....	10
ii. Eruptive History .....	11
iii. Montserrat Volcano Observatory .....	14
2.2 Thermal Infrared Remote Sensing .....	17
2.2.1. Instrumentation .....	22
i. Advanced Spaceborne Thermal Emission and Reflection Radiometer.....	22
ii. Geostationary Operational Environmental Satellite .....	25
2.3 Multi-parameter Database .....	26
<b>Section 3: Methodology .....</b>	<b>28</b>
3.1 Spaceborne Data .....	28
3.1.1. Image Processing....	28
3.1.2. Georectification.....	31
3.1.3. Spectral Deconvolution.....	33
3.1.4. GOES and ASTER Temperature Comparison.....	34
3.2 Database .....	34
<b>Section 4: Results .....</b>	<b>39</b>
4.1 Statistical analysis of database .....	39
4.2 Spectral deconvolution and Dome Characterization .....	40
4.3 GOES and ASTER temperature .....	48
<b>Section 5: Discussion .....</b>	<b>49</b>
<b>Section 6: Conclusions and Future Work .....</b>	<b>52</b>
Appendix 1.....	105
Appendix 2.....	110
Appendix 3.....	113
References .....	144

## List of Figures

<b>Figure 1.</b> Cross-sectional view of rhyolite dome .....	56
<b>Figure 2.</b> Crease structure .....	57
<b>Figure 3.</b> Location map .....	58
<b>Figure 4.</b> MVO hazard map .....	59
<b>Figure 5.</b> Blackbody radiance curve .....	60
<b>Figure 6.</b> TIR spectra of silicates .....	61
<b>Figure 7.</b> Laboratory emission spectra of quartz .....	62
<b>Figure 8.</b> Threshold of deconvolution results .....	63
<b>Figure 9.</b> Photon interaction with void spaces .....	64
<b>Figure 10.</b> Two-temperature sub-pixel mixing .....	65
<b>Figure 11.</b> Atmospheric windows.....	66
<b>Figure 12.</b> ASTER system response functions.....	67
<b>Figure 13.</b> End-member spectra with sulfur dioxide.....	68
<b>Figure 14.</b> November 1, 2000 ASTER scene.....	69
<b>Figure 15.</b> December 28, 2000 ASTER scene .....	70
<b>Figure 16.</b> January 13, 2001 ASTER scene.....	71
<b>Figure 17.</b> April 13, 2002 ASTER scene.....	72
<b>Figure 18.</b> August 3, 2002 ASTER scene.....	73
<b>Figure 19.</b> October 29, 2002 ASTER scene.....	74
<b>Figure 20.</b> Image processing.....	75
<b>Figure 21.</b> ASTER DEM .....	76
<b>Figure 22.</b> End-member spectra.....	77
<b>Figure 23.</b> November 1, 2000 end-member distribution .....	78
<b>Figure 24.</b> December 28, 2000 end-member distribution .....	79
<b>Figure 25.</b> January 13, 2001 end-member distribution.....	80
<b>Figure 26.</b> April 13, 2002 end-member distribution.....	81
<b>Figure 27.</b> August 3, 2002 end-member distribution .....	82
<b>Figure 28.</b> October 29, 2002 end-member distribution.....	83
<b>Figure 29.</b> November 1, 2000 emission spectra.....	84
<b>Figure 30.</b> December 28, 2000 emission spectra .....	85
<b>Figure 31.</b> January 13, 2001 emission spectra.....	86
<b>Figure 32.</b> April 13, 2002 emission spectra.....	87
<b>Figure 33.</b> August 3, 2002 emission spectra.....	88
<b>Figure 34.</b> October 29, 2002 emission spectra .....	89
<b>Figure 35.</b> GOES image with resampled ASTER image .....	90
<b>Figure 36.</b> Rockfall occurrence graph.....	91
<b>Figure 37.</b> Long rockfall occurrence graph .....	92
<b>Figure 38.</b> Hybrid earthquake occurrence graph.....	93
<b>Figure 39.</b> Long period earthquake occurrence graph .....	94
<b>Figure 40.</b> Volcano-tectonic occurrence graph.....	95
<b>Figure 41.</b> Sulfur dioxide output graph .....	96
<b>Figure 42.</b> Gas venting versus rockfall statistical analysis.....	97

<b>Figure 43.</b> Hybrid earthquake events versus explosions statistical analysis.....	98
<b>Figure 44.</b> Hybrid earthquake events versus rockfall statistical analysis .....	99
<b>Figure 45.</b> GOES and ASTER temperature comparison .....	100

## List of Tables

<b>Table 1.</b> Instrument specifications .....	101
<b>Table 2.</b> GOES versus ASTER temperature data .....	102
<b>Table 3.</b> Metadata for ASTER images .....	103
<b>Table 4.</b> Spectral deconvolution results .....	104

## **Section 1. Introduction**

Volcanic hazards produced by large historical strato-volcano eruptions such as Mt. Pelee, Martinique (1902), Soufrière, St. Vincent (1902), and Santiaguito, Guatemala (1902) have directly and indirectly affected many populations around the globe, commonly destructively (Nakada, 2000; Small and Naumann, 2001). The potential of future eruptions (i.e., Popocatepetl) combined with increasing population centers in high risk areas has produced a very clear supporting argument for improving volcanic monitoring and mitigation efforts (De La Cruz-Reyna et al., 2000; Small and Naumann, 2001; Tilling, 1989). Historically, pyroclastic flows are the most lethal of volcanic hazards (Tilling, 1989). They can originate during both effusive and explosive phases and can potentially be forecasted by changes in surface features (Cole et al., 1998; Fink et al., 1992; Fink and Manley, 1987; Tilling, 1989). The most important aspect of preparedness is to identify these conditions or precursors.

Satellite remote sensing instruments have played an important role in monitoring efforts by safely providing image data with various spatial, spectral, and temporal resolutions (Glaze et al., 1989; Harris et al., 2001a). The Advanced Spaceborne Thermal Reflection and Emission Radiometer (ASTER) is the first sun-synchronous, polar-orbiting spaceborne satellite to collect more than two bands in the thermal infrared region (TIR) at high spatial resolution (Table 1) (Ramsey and Fink, 1999; Yamaguchi et al., 1998). The TIR data have been shown capable of discerning textural variations on both inactive and active silicic lava domes (Ramsey and Dehn, 2003; Ramsey and Fink, 1994, 1999). This methodology has now been applied to an active dome on a populated



island in the Caribbean. Soufrière Hills, Montserrat, has provided a unique opportunity for study because of the almost continuous surface changes due to silicic dome growth and collapse and heavy monitoring by the Montserrat Volcano Observatory (MVO) and associated scientists (Aspinall et al., 2002; Kokelaar, 2002; Sparks and Young, 2002).

Satellite remote sensing has played an integral part in monitoring and characterizing active volcanic processes or in aiding to identify preliminary stages of activity (Dozier, 1981; Glaze et al., 1989; Harris et al., 2001b; Oppenheimer, 1998). Previous remote sensing of active volcanoes using bands in TIR focused on temperature-based measurements using weather satellites. Examples include identifying and monitoring such processes as: 1) thermal flux within lava lakes (Harris et al., 1999), 2) effusion rates of active basaltic flow fields (Flynn et al., 2001; Harris et al., 1998), 3) volcanic domes (Abrams et al., 1991), and 4) the onset of fumarolic activity (Dozier, 1981; Glaze et al., 1989; Harris et al., 2000; Oppenheimer, 1998). Satellites used primarily for weather monitoring commonly have low spatial and spectral resolutions and various temporal resolutions. The Geostationary Operational Environmental Satellites (GOES) offer low spatial (1-4 km) and spectral resolution (2 channels in TIR), but high (15 minutes) temporal coverage (Table 1). The Advanced Very High Resolution Radiometer (AVHRR) satellite is polar orbiting (rather than geostationary) with two channels in the TIR, and having 1.1 km spatial resolution with a 4-6 hour repeat time (Table 1). The much higher spatial resolution Enhanced Thematic Mapper Plus (ETM+) instrument currently has the highest spatial resolution in TIR (60 meters with only one channel) of any commercial satellite (Table 1). It is

aboard the Landsat 7 satellite in a sun-synchronous orbit with 16 day repeat time.

Increased spectral and spatial resolution in TIR allows for better quantitative constraints on size and extent of lava flows and associated temperature derived activity (Flynn et al., 2001).

These satellites do not provide the TIR spectral resolution to accurately examine emission from surfaces. The spectral and spatial capabilities of ASTER provide improvement upon temperature and emissivity data for volcanic applications. Thermal infrared radiance is a function of temperature and emissivity of a material. For most surfaces, temperature is isothermal for each pixel and therefore can be derived from a minimum of one TIR band. Hot targets such as volcanoes, can have variable temperatures per pixel and require at minimum two channels to derive sub-pixel temperature differences (Dozier, 1981). Emission is a material property that varies with wavelength and is independent of temperature. Materials have a unique TIR spectral signature used for identification. The higher the spectral resolution, the more accurate the identification of that material becomes. Silicate materials have been positively identified with as few as 4 to 5 TIR bands (Ramsey and Christensen, 1998; Ramsey and Fink, 1999).

Features and textures of silicic dome surfaces, such as the distribution of vesicular pumice and obsidian, are manifestations of sub-surface processes such as stress, strain, degassing rate, temperature, and eruption rate. These features are important to the interpretation of spaceborne remotely sensed image data and hazard assessment (Fink et al., 1992). Ramsey and Fink (1999) have shown that using a high

spatial and spectral TIR resolution instrument, such as ASTER, the distribution of vesiculated rock can be mapped over an inactive dome surface. Their linear spectral deconvolution technique employs the spectral signatures of two known end-member materials to resolve the unknown spectrum into areal abundances of each end-member. Their methodology combined with the high spectral and spatial resolution of ASTER was applied to the active Soufrière Hills dome to determine changes in surface vesicularity.

The temporal resolution of cloud-free ASTER image acquisition for Soufrière Hills is low and can be enhanced by other datasets. ASTER has collected approximately thirty-seven images of the island of Montserrat since its launch in December 1999. The Soufrière Hills dome is relatively or completely cloud-free in only six images. Data collected by the MVO and associated scientists enhance interpretation of image data and aid in assessing volcanic activity in between image acquisition. Ideally, high temporal resolution, seismic records would provide the data necessary to interpret the state of activity of the volcano, providing corresponding information at the moment of satellite image capture. These data are unavailable for this study at that resolution; however the MVO does provide a weekly comprehensive summary of volcanic activity available on-line (<http://www.mvo.ms/>). This information has been converted into a database to serve as a framework for image analysis and characterizing any longer term cyclic trends in behavior. High temporal resolution GOES temperature data are also compared to that of ASTER to potentially serve as an additional comparison resource.

The primary focus of this work is to apply the spectral deconvolution technique of Ramsey and Fink (1999) to an active volcanic dome using a multispectral, high spatial spaceborne satellite. The intention of this study is to accomplish the following: 1) describe the distribution of vesiculated rock and glass over time on the Soufrière Hills silicic lava dome using ASTER, 2) link the remote sensing results to the multi-parameter database and GOES temperature data, and 3) statistically analyze the database to identify correlations between a variety of behavioral characteristics. The satellite remote sensing techniques utilized in this study coupled with statistical analysis of a multi-parameter database will augment and improve current monitoring techniques at Soufrière Hills. These methods can easily be applied to other volcanoes that are re-activating or to other active areas that have the potential of transitioning from effusive to explosive dome growth, subsequent collapse and ensuing pyroclastic activity.

## **Section 2: Background**

### **2.1 Volcanology**

#### **2.1.1. Silicic Lava Domes**

Silicic lava domes are potentially very hazardous volcanic features characterized by extruded viscous lava that has cooled and amassed near vent. Domes are generally characterized by a blocky surface, steep sides, and relative proximity to the source. The lava may range in composition from basaltic andesite to rhyolite (Fink and Anderson, 2000). Four principle types of lava domes (pelean, lobate, endogenous, and

axisymmetric) are identified by Fink and Anderson (2000) based upon small and large scale surface features, eruptive style, and physiography. Pelean domes are very steep sided and blocky, circular in form, and commonly produce spines that are surrounded by a smooth surface in the immediate vicinity. Lobate domes have less steep sides, lobate extrusions, and an irregular form. Endogenous domes have carapace variations between platy and very blocky, numerous surface ridges, and a relatively lower profile. The last type, axisymmetric, is controlled by topography and therefore may have a highly irregular form and an almost flat surface. Dome morphology (from the Pelean to the axisymmetric end-member) is constrained by an increase in eruption rate, a decrease in cooling rate, and a decrease in the carapace yield strength. For example, surface features and textures of a Pelean dome (spines) are manifestations of a relatively low eruption rate and relatively high cooling rate and yield strength. Two other categories of domes, cryptodomes and coulees, are not based on the previously stated characteristics: 1) cryptodomes accumulate beneath the surface and push up material, occasionally producing a visible mound and 2) coulees which are also categorically lava domes, but are typified by flow due to steep topography.

The characteristics of surface features of the four principle types of lava domes are indicative of the eruption style and hazard potential. Changes in these features indicate a change in eruption mechanisms and potentially increased or decreased risk of collapse, explosions, or other hazards. For example, an increase in eruption rate may translate into an increase in rockfalls and pyroclastic flows. Small scale features and textures of the silicic dome surface, such as the distribution of glass and vesiculated

rock, are also indicative of sub-surface processes. Textural changes detected on the surface using remotely sensed image data have therefore been hypothesized to aid in hazard assessment (Fink et al., 1992; Ramsey and Fink, 1999).

The cross-sectional view of a rhyolite dome (Figure 1) reveals discrete layering comprised of coarsely vesiculated pumice (CVP), finely vesiculated pumice (FVP), and obsidian in a distinct order (Fink and Manley, 1987). The layering is as follows: the outermost several meters of FVP (<0.5mm non-connected vesicles) are followed by obsidian, CVP with 1-10mm distorted vesicles comprising approximately 50% vol., a second layer of obsidian, a layer of crystalline rhyolite with anhydrous phenocrysts of quartz and feldspar, and a lower layer of obsidian. The density contrast between the CVP (less dense) and the overlying obsidian (more dense) allows the CVP to rise buoyantly as a diapir along with an outside layer of obsidian (Figure 1) (Ramsey and Fink, 1999). Two fundamentally different models have been proposed to explain the layering in silicic lava domes based upon petrographic studies and visual and physical observations. (Eichelberger et al., 1986; Fink et al., 1992) states that the layering is created by the deflation of an erupted "permeable foam" lava that compresses under its own weight during flow. Other workers have refuted this model, suggesting that the lava is volatile-rich at eruption and vesiculates during flow (Fink and Anderson, 2000; Fink et al., 1992). Each layer forms separately based on the amount of bubbles and their ability to migrate during flow. If the latter model is true, monitoring of silicic domes becomes very important due to their probability of explosive decompression (Fink and Anderson, 2000; Fink et al., 1992). Monitoring the surface features of a silicic

dome long term, during eruption and after extrusion has ceased can effectively be accomplished using satellite data.

Andesite and dacite lava domes exhibit variation in surface texture from simpler layering of scoriaceous lava underlain by smooth lava. The six year formation (1980-1986) and nearly 20 separate eruption episodes of the dacite lava dome on the crater floor of Mt. St. Helens provided opportunity for surface texture analyses and identification of smooth and scoriaceous end-members. The uppermost scoriaceous layer contained irregular and deformed bubbles (elongated in the direction of flow) which comprised up to 50% of the volume. The smooth layer contained less than 15% vesicles that were not elongate (Anderson and Fink, 1990). The dominant surface feature observed were crease structures (also observed on rhyolitic domes), which are paired convex walls exposing the smooth surface underneath (Figure 2). These structures tend to form where lava spreads laterally and indicate flow down slope, strain rate, and thermal and mechanical conditions during flow (Fink and Anderson, 2000). The distribution of volcanic units with scoriaceous textures and smooth surfaces also reflects the fluctuation of volatile content (Anderson and Fink, 1990). The surface features likely indicate how well the magma is degassing during ascent rather than the existence of a stratified magma chamber as previously thought (Anderson and Fink, 1990; Fink and Anderson, 2000).

Exogenic (effusive) lava dome growth can signal a change in the state of the volcanic system. The extrusion indicates either: 1) re-activation of the source or an influx of new magma into the chamber (signaling possible future explosive activity), or

2) forming as a late stage phase following a large eruption, such as at Mount St. Helens. Lava domes can grow in a relatively short period of time or in episodes separated by years to decades. In some cases, the period of quiescence is somewhat proportional to the amount of lava extruded in an episode (Fink et al., 1990). Volcanic hazard risk increases where effusive changes to explosive extrusion or the dome becomes unstable (Kaneko et al., 2002). Pyroclastic flows and surges may be generated by either dome collapse or from fountain collapse of an explosive eruption. Dome collapse is related to a) over-pressurization of volatiles high in the conduit that initiate failure or b) instability related to such factors as hydrothermal alteration, fracturing (Elsworth and Voight, 2001), gravitational forces (Cole et al., 1998), seismicity (Cole et al., 1998), or high extrusion rates (Fink and Anderson, 2000). Sustained dome collapses at Soufrière Hills have produced pyroclastic flows with as much as 6.5 km run out distance traveling 15-30 m/s (Cole et al., 1998). Pyroclastic flows and surges generated by column collapse, partial column collapse, or “boiling over” near the vent generally have longer run out distances, higher temperature, higher travel speeds, and lower frequencies than those due to dome collapse (Tilling, 1989). The signals that may indicate the transition from effusive to explosive behavior are not well understood. Hypotheses on the degassing of silicic magma are varied and it is quite possible that not one model fits all volcanic domes. Magma may lose gas either in shallow feeding conduits, along the ascent path through fractures in the wall rock of the conduit, and/or after eruption has ceased (Fink and Anderson, 2000; Menand and Tait, 2001; Sparks et al., 2000). In the latter case, seemingly stable flow fronts can produce explosions and



pyroclastic flows after growth has ceased (Fink et al., 1992). These conditions are derived from zones of increased vesiculation that migrate and coalesce beneath the cooled carapace (Fink et al., 1992).

This style of eruption and subsequent hazard concern is a primary reason for this application of remote sensing. Risk of volcanic hazards does not necessarily cease when extrusion of lava has ended. The high spatial and spectral resolution of the ASTER instrument allows for better constraints to be placed upon the small scale distribution and change in distribution of glass and vesiculated rock. ASTER provides a safe means of monitoring changes in surface features of lava domes and will likely play an important role in mitigation efforts.

### **2.1.2. Soufrière Hills, Montserrat**

#### **2.1.2.i. Geologic Setting**

The Lesser Antilles arc extends from the island of Sombrero in the north to Grenada, approximately 800 km south, between the Atlantic Ocean and Caribbean Sea (Figure 3). The arc bifurcates north of the island of Martinique with the apex at the island of Guadeloupe. The western or inner arc is volcanically active whereas the outer extinct remnant arc was active from Eocene to mid-Oligocene and is now limestone capped (Sigurdsson and Carey, 1991). The southern portion of the active arc is bounded to the west by the Grenada trough, a back-arc basin, and the Aves Ridge, presumably another and older extinct island arc. The east is bounded by the Tobago Trough, a smaller fore-arc basin, and the Barbados Ridge, a thick accretionary wedge

(20 km) fed by sediments from the Orinoco River in Venezuela (Kearey and Vine, 1996; Sigurdsson and Carey, 1991). The subducting Atlantic Plate is sectioned into three segments, all of which have differing dip angles and slip vectors. The Benioff Zone dips westward between 50-60° below the northern segment containing Montserrat eastward at 45-50° in the middle segment, and near vertically in the less active south (Kokelaar, 2002; Sigurdsson and Carey, 1991). Convergence rates vary from 20-40 mm/year (Kokelaar, 2002).

The island of Montserrat is 16.5 km north to south by 10 km east to west and is a United Kingdom overseas territory in northern Lesser Antilles (Figure 3). Soufrière Hills volcano (Figure 3), situated in the southern part of the island, is the youngest of four volcanic centers (Silver Hill, Centre Hills, Soufrière Hills, and South Soufrière Hills) ranging in age from Pliocene to Holocene (Roobol and Smith, 1998). The volcano is comprised of five andesitic lava domes: Gage's Mountain, Chance's Peak, Galway's Mountain, Perches Mountain, and the youngest, Castle Peak. Castle Peak occupies English's Crater, a horse-shoe shaped depression approximately 1 km in diameter that opens to the East (Sparks and Young, 2002) and is the location of the most recent (1995- present) volcanism.

### **2.1.2 ii. Eruptive History**

Three periods of volcanism, during the past 31,000 years (not including the present day activity) have been identified based on stratigraphic studies, petrographic analysis, and radiocarbon dating (Roobol and Smith, 1998). The first period ranges from

approximately 31,000 - 16,000 BP and is characterized by andesitic block and ash flows, which are divided into three discontinuous units (Roobol and Smith, 1998). The second period commenced approximately 4000 years ago and is characterized by a dense ash flow deposit that forms a thin veneer of deposits east, northeast, and southwest (Roobol and Smith, 1998). The third and most recent period (770 - 200 years B.P.) is expressed by block and ash flows, but the deposits are overall finely-grained and ash-rich. Surge deposits are also included in this unit, but are not extensive (Roobol and Smith, 1998).

In addition to previous volcanic activity, three major seismic crises have been identified, in addition to few minor earthquakes. Hot springs and fumaroles (soufrières), minor changes in tilt, and earthquakes along an ESE-trending zone comprised the activities during the three major crises in 1897-98, 1933-37 (MacGregor, 1938; Perret, 1939) and 1966-67 (Shepherd et al., 1971). A seismic event 30 km from Soufrière Hills resulted in low levels of seismicity in 1985 (Young et al., 1998).

Soufrière Hills has undergone three different eruptive periods from 1995 to present, based upon severity of growth and collapse (Young et al., 1998). The current activity at Soufrière Hills initiated in 1992 with seismicity characterized by several swarms of volcano-tectonic earthquakes that increased in November 1994. Phreatic activity began on July 18, 1995, and included the jetting of steam, increased seismicity, the expulsion of a spine of oxidized rock later in September. On November 15, 1995 juvenile magma first reached the surface (Sparks and Young, 2002). The first period, from 1995 through 1998, was characterized initially by semi-continuous dome growth

and later by cycles of growth and collapse. The first prominent dome collapse occurred in July, 1996 (Sparks and Young, 2002). June 25, 1997, marked another major collapse of the dome, which large produced pyroclastic flows. These traveled to the central and eastern areas in three separate pulses, killing 19 people and injuring several more. In early August, 1997, Vulcanian explosions occurred repeatedly and resulted in a fountain collapse event which generated more extensive pyroclastic flows (Sparks and Young, 2002). Two large dome collapses occurred on November 4 and 6. A very large sector collapse occurred on December 26, 1997 (Boxing Day) and produced a pyroclastic density current that devastated 10 km<sup>2</sup> of southern Montserrat (Sparks and Young, 2002). Dome growth continued, accompanied by energetic ash-venting, but then ceased. It was during this period that the island population diminished from initially 10,500 to just over 3,000. The duration of the second period, from early 1998 to late 1999, is characterized by no extrusion, but the occurrence of dome collapse, ash venting, block and ash flows and small Vulcanian explosions (Sparks and Young, 2002). The third period, from late 1999 to present, shows renewed extrusion and two large collapses occurring on March 20, 2000 and July 29, 2001 (Sparks and Young, 2002). Kokelaar (2002) presents a detailed temporal account of emergency related responses and volcanic activity history from 1995-1999.

Kokelaar (2002) identified five eruptive phases from the 1995-1999 period based upon how material was extruded: 1) phreatic explosions, 2) dome growth with subsequent pyroclastic flows from collapse, 3) magmatic explosions with pyroclastic flows generated by column collapse, 4) sector collapse with pyroclastic density currents

and explosions (Sparks and Young, 2002), and 5) ash venting. Phreatic explosions refer to the interaction of heated groundwater early in 1995, due to the rise of magma and the release of volatiles. It is unlikely that juvenile magma was produced during this phase. Lava dome growth and collapse has occurred mostly during 1996, 1997, and 1998. Larger collapses removed higher volatile content material deeper within the dome. Collapses of this magnitude produce highly fragmented deposits, small eruptive columns, and pyroclastic surges (Cole et al., 1998). This degree of dome collapse and subsequent pyroclastic flow generation is also referred to as 'Merapi style' (Cole et al., 1998). Magmatic explosions follow very large dome collapses which expose volatile-rich magma and consequently produce large and sustained eruptive jets. Column collapses produce radially directed deposits that are pumiceous. Sector collapse (such as the Boxing Day collapse) is a large, sudden failure due to structural instability. Sector collapse results in rapid depressurization and disintegration of the dome material that produces a pyroclastic density current. Ash venting occurred periodically but was prominent during the calmer growth phase post mid-March, 1998, and attributed to magma fragmentation from the release of volatiles.

### **2.1.2.iii. The Montserrat Volcano Observatory**

The following description of the Montserrat Volcano Observatory (MVO) history, responsibilities, and associated science was adopted from a very detailed account in Aspinall (2002).

Seismic stations existed on Montserrat before the volcanic crisis in 1966, but it was not until the phreatic explosions in July, 1995, that an observatory was established. The Seismic Research Unit (SRU) of the University of West Indies, whom had been monitoring seismicity prior to 1966, established a base for monitoring purposes and to interact with the local authorities (Aspinall et al., 2002). The United States Geological Survey (USGS) Volcano Disaster Assistance Program (VDAP) and Guadeloupe Volcano Observatory scientists joined the SRU for monitoring assistance in a temporary facility in Plymouth (the capitol destroyed by pyroclastic flow in July 1997). In the first six weeks, the pre-existing seismic network was reinforced with a short-period seismograph and three electronic tiltmeters, and correlation spectrometer (COSPEC) monitoring was established. Scientists and volunteers were employed to help monitor Soufrière Hills 24 hours/day. Details of the infrastructure (social, political, and economic) can be found in Clay et al. (1999). The three main aims of the MVO monitoring efforts comprise managing the seismic and tiltmeter networks as well as visual observations. Other objectives include petrographic study, gravity surveys, dome morphology and volume calculation, rock-strength measuring, and environmental monitoring using groundwater, rainwater, and ash analysis and geochemical analysis. Sparks and Young (2002) provide a detailed account of the scientific results stemming from the 1995-1999 period of activity.

Direct measurements of eruption temperatures and analysis of the vesicle content of dome rock are importance to this study. Ideally, these data would be most helpful if analyzed at the corresponding time of image acquisition, but they do provide a

framework for analysis. A recent paper by Formenti and Druitt (2003) characterize vesicle connectivity and related pyroclastic flows by scanning electron microscope (SEM). Temperature measurements of dome collapse blocks a few hours after emplacement on September 21, 1997, range from 365-640 °C. Seven samples from this event were analyzed with SEM and showed a range from 0-50% vesicle content. More recently, vesicularity was reported as approximately 2%, most likely from pyroclastic flow samples (M. Edmonds, personal communication, 2003). Glass content ranges from 25-30% for rapid emplacement and 5-15% for samples that have spent a significant time within the dome (Sparks et al., 2000).

The MVO crisis management effort requires frequent interaction among scientists, public authorities, and residents. The Montserrat Alert System was instituted in December 1995 and is an established means of communication between authorities and scientists. A hazard map aids in this communication by geographically outlining areas on the island of various risk levels and the exclusion zone (Figure 4). Examples of interaction with the public include regular reports, interviews, and call-in programs on the radio, newspaper reports, lectures, a magazine, and television shows that contain updates on activity and risk factors. The MVO maintains an "open door" policy with the public (Aspinall et al., 2002).

The Caribbean Andesite Lava Island-volcano Precision Seismo-geodetic Observatory project, or CALIPSO, is designed to monitor the Soufrière Hills volcanic system with an array of specialized instruments intended to withstand high temperatures over the course of a few (>3) decades (2003). The project is a joint effort

between scientists from Penn State University, Carnegie Institute of Washington, University of Arkansas, Duke University, the MVO, Bristol, and Leeds made possible with funds from the National Science Foundation. The objective is to install an instrument package including a strainmeter, a tiltmeter, and seismometers into each of four 200 meter boreholes, coupled with a continuous global positioning system at each site, to aid in data collection on short (6-18 hour), meso (~7 weeks), and long-term (~30 year) time scales. This project will enable scientists to monitor magma chamber and conduit processes in an active andesitic stratovolcano for the first time with such intensity (2003).

## **2.2 Thermal Infrared Remote Sensing**

Energy impinging upon a surface will be altered by that surface by one of the following ways: reflected, scattered, transmitted, or absorbed and re-radiated, generally to longer wavelengths. Energy emitted from a surface in the thermal infrared region of the electromagnetic spectrum (6-100  $\mu\text{m}$ ) possesses properties inherent to the surface and consequently make identification of the material and its temperature possible (Salisbury and D'Aria, 1992). Both temperature and emissivity data are employed in this study and will be addressed in this section. (The technique used by the ASTER team to derive Level 2 temperature and emissivity data products is addressed and discussed in detail in the algorithm theoretical basis document (ATBD) (Gillespie et al., 1999)).

Radiant energy (L) in TIR is a function of the kinetic temperature of an object as well as its wavelength dependent emissivity, which can be separated from each other



by a number of techniques (Gillespie et al., 1999; Kahle and Alley, 1992; Salisbury and Walter, 1989; Schmugge et al., 1998). A blackbody (B) is an ideal object that absorbs all energy impinging upon it and re-emits 100% of that energy as a function of temperature and wavelength (Siegal and Gillespie, 1980). This relationship is described by the Planck equation:

$$L_{(\lambda,T)} = \epsilon_{\lambda} B_{(\lambda,T)} = \epsilon_{\lambda} \{C_1 \lambda^{-5} / [\exp (C_2/\lambda T) - 1]\}$$

where  $C_1 = 3.74 \times 10^{-16} \text{ W m}^2$  and  $C_2 = 0.0144 \text{ m K}$ . A blackbody curve is featureless at all temperatures and wavelengths, and shifts to shorter wavelengths with increasing temperature (Figure 5). Real materials generally do not emit perfectly at all wavelengths and hence have emission lows (absorption bands). Emission at discrete wavelengths is an inherent trait of a material and can be used for identification. Because the Planck equation used to separate temperature from emissivity is underdetermined (one more unknown than the number of possible equations), either the temperature or one wavelength-dependent emissivity must be assumed. This has lead to the multiple techniques previously mentioned (Gillespie, 1992; Glaze et al., 1989; Kahle and Alley, 1992; Salisbury and Walter, 1989).

Emissivity is described as the ratio of radiant flux from an object to that of a blackbody at the same kinetic temperature (Sabins, 1996). Emission varies with wavelength because the intensity is conditional upon the vibrational properties of the molecular bonds of the material, such as spatial geometry, bond strength, and number and type of atoms (Siegal and Gillespie, 1980). These conditions promote selective absorption of energy at discrete wavelengths (Salisbury et al.). Silicates, specifically,

have absorption features due to the bending, stretching, and vibration of the Si-O and silica-cation bonds. The wavelength range (7-11  $\mu\text{m}$ ) of the primary absorption feature, or reststrahlen band, is dictated by the bond strength and degree of polymerization of the silica tetrahedra. The feature shifts to shorter wavelengths (Figure 6) from isolated to framework structures, or in other words, from mafic to felsic compositions (Salisbury and Walter, 1989). Silicate glass spectra display a broadening and shallowing of this feature because of the randomness of the tetrahedra due to quenching and lack of a long-range ordering of the polymerization.

This primary feature is a function of the real and imaginary components of the optical properties of the material (index of refraction ( $n$ ) and absorption coefficient ( $k$ )) and remains constant in position and not morphology with variations in particle sizes (Figure 7) (Lyon, 1965; Moersch and Christensen, 1995; Ramsey and Christensen, 1998). Common rock forming minerals have high absorption coefficients ( $k$ ) and therefore little to no volume scattering above a threshold of approximately 60  $\mu\text{m}$  (Ramsey and Christensen, 1998). Photons typically interact with particles only once and consequently combine linearly in the TIR. Hence, the resulting emission spectrum of a pixel will be a combination of the areal percentage of each end-member spectrum present on the surface (Adams et al., 1993; Gillespie, 1992). If the end-members are known, the spectrum can be deconvolved into the constituent spectra and their abundances (Figure 8). In the 10-60  $\mu\text{m}$  range, spectra combine linearly only where end-member spectra are derived from material of a similar particle size (Ramsey and Christensen, 1998).

Ramsey and Fink (1999) applied the linear spectral deconvolution method to Little Glass Mountain, a Holocene rhyolitic flow, near the summit caldera of Mount Shasta in northern California. Vesicle percentage was estimated using a sub-pixel analysis with two end-members, obsidian and blackbody, using the airborne Thermal Infrared Multispectral Scanner (TIMS) instrument. The absorption feature from 7-11  $\mu\text{m}$  is widened in spectra derived from obsidian being caused by the lack of Si-O tetrahedral polymerization. Vesicles, on the other hand, are concave voids, much greater in size than the emitted wavelength. This promotes a photon to interact with the surface more than once and consequently, a shallowing of the absorption feature, or increased emission (Figure 9). A blackbody spectrum provides a proxy for the surface texture caused by vesicles and is used as an end-member to determine areal vesicle percentage. Presuming that emission spectra combine linearly in the TIR wavelengths, areal percentages of obsidian and vesicles were estimated using the linear spectral deconvolution technique. Ramsey and Fink (1999) were able to map the distribution of finely and coarsely vesiculated pumice on the surface of the flow with good agreement to laboratory results of collected samples. This surface distribution of end-member textures showed an area of the dome of increased vesicularity. In preparation for the launch of ASTER, the TIMS data was degraded from 10.4 meter to 90 meter pixels. The lobe of high vesicle content was still detectable at that lower resolution. It was hypothesized that this area on an active or recently active dome may be prone to explosive behavior and ensuing hazards.

Wein's Law demonstrates the shift in the radiance peak to shorter wavelengths as temperature increases (Figure 5). Because a remote sensing instrument detects one radiance value per pixel, a heterogeneous temperature distribution would produce a mixture of multiple radiant curves (Figure 10). Temperature can no longer be accurately derived solely from the Planck equation with one assumption (Dozier, 1981; Glaze et al., 1989; Harris et al., 2000; Ramsey and Dehn, 2003). The two-temperature model, or radiant mixing described by Dozier (1981) constrains the background temperature value, the elevated temperature, and the percentage each value contributes to the radiance. However, that work did not deal with emissivity of the surface due to the limited spectral resolution of the satellite instruments available at the time. Where temperature and emissivity are separated in multispectral TIR data, the resulting emissivity spectra for a mixed temperature pixel will show a marked decrease (or "roll-off") in emissivity at longer wavelengths (Figure 31, pixel 1). Therefore, the spectral shape of the recovered surface emissivity spectrum would retain its gross morphology, but have higher values in shorter wavelengths and lower values in longer wavelengths (a drop in Band 14). Two-temperature mixing was not a factor for the work done by Fink and Ramsey (1999) but should be considered where examining data from an active volcano.

Most thermal sensors collect energy in the 8-14  $\mu\text{m}$  range in a region of high atmospheric transmissivity (window) (Figure 11). This region also corresponds to the primary absorption feature of silicate structures (Figure 6) (Dozier, 1981; Kahle and Alley, 1992; Kahle et al., 1991). There are two other thermal wavelength regions with

some remote sensing potential (3-5  $\mu\text{m}$  and 17-25  $\mu\text{m}$ ). The 17-25  $\mu\text{m}$  wavelength region is subject to atmospheric attenuation and only transmits approximately 20-50% incoming energy, whereas the 3-5  $\mu\text{m}$  region overlaps with reflected solar energy during the day, making interpretation difficult (Harris et al., 2000). The radiation reaching the sensor is a product of emission, scattering, and absorption of particulates and gasses of the atmosphere as well as emission from the ground surface. This energy needs to be removed to isolate the ground radiance by using an atmospheric correction model. Correction models used for ASTER Level 2 data are described by (Abrams, 2000).

## **2.2.1 Instrumentation**

### **2.2.1.i. Advanced Spaceborne Thermal Infrared and Reflection Radiometer**

The ASTER instrument, aboard NASA's first Earth Observing System (EOS) platform (Terra), was launched December 18, 1999. ASTER is a high spatial resolution, multispectral instrument with stereo capabilities and five spectral bands in the TIR (Kahle et al., 1991). The satellite was designed and built by the Japanese government under MITI (Ministry of International Trade and Industry). The scientific team consists of Japanese, American, and Australian scientists whose responsibilities include designing algorithms for data management, reduction and analysis (Abrams, 2000). These objectives of the scientists consist of the assessment and monitoring of natural or anthropological processes and hazards with an emphasis on volcanoes, glacial dynamics, climatology, resource exploration, land cover modification, and vegetation

change (Abrams and Hook, 1995). Comprehensive research plans and targeted areas of science are detailed by Yamaguchi et al (1998).

ASTER consists of three instrument sub-systems covering fourteen bands over three wavelength regions: three visible and near-infrared (VNIR) bands, six short-wavelength infrared (SWIR) bands, and five TIR bands (Table 1). The VNIR sub-system includes a separate, backward pointing ( $27.6^\circ$ ), single-band telescope that permits stereo capability and the production of digital elevation models (DEM) at 30m posting resolution (Abrams, 2000). Cross-track pointing of the sensors, up to  $\pm 116$  km from nadir, also allow for a repeat time of less than sixteen days. For a target near the equator at maximum pointing the repeat time can drop to four days from the normal sixteen days (Yamaguchi et al., 1998). The image swath width is 60 km and the orbital altitude is 705 km. Images are acquired at approximately 10:30 AM/PM local time for scenes at the equator. The TIR sub-system has a fixed telescope with pointing and scanning done by a rotating mirror. The system uses a staggered array of ten mercury-cadmium-telluride (HgCdTe) detectors with five bandpass filters (Figure 12) (Kahle et al., 1991). Increased data acquisition of a specific target area can be requested by approved EOS investigators. ASTER is capable of collecting approximately 1.7 million scenes throughout the six year mission.

Several levels of data products are provided by the science team. (Abrams, 2000) provides detailed information on data architecture and standard data products. Validated Level 2 product data AST 05 (surface emissivity) and AST 08 (surface kinetic temperature) were chosen for the primary analysis in this study. (Level 1B non-

atmospherically corrected data was also used in conjunction with the GOES satellite. The temperature and emissivity products are produced using the ASTER temperature/emissivity separation (TES) algorithm. The algorithm entails running two input data sets (land-leaving TIR radiance and down-welling sky irradiance) through four modules consisting of the normalized emissivity method, ratio for spectral shape, min-max difference for improved accuracy, and finally quality assurance. The TES algorithm is explained in greater detail in the ATBD (Gillespie et al., 1999). The atmospheric correction algorithm employs the Moderate Resolution Atmospheric Radiance and Transmittance Model (MODTRAN) code and can use additional input information from the MODIS (Moderate Resolution Imaging Spectrometer) and MISR (Multiangle Imaging SpectroRadiometer) instruments, also on the TERRA platform. Other methods of atmospheric correction, NASA EOS (GEOS-1) and the EMC (Environmental Monitoring Center) global assimilation forecast system, have been utilized in absence of the preferred option above. These were projected only be used where necessary and requested on-demand (Gillespie et al., 1999).

Despite robust atmospheric correction applied to ASTER data, interference from certain gasses still need to be considered in retrieving accurate surface radiance, emissivity, or temperature. Montserrat is situated near the equator, in a tropical climate. The wet months are April-May and July-September, but humidity remains high throughout the year. ASTER Band 10 is near the edge of the atmospheric window, where energy is absorbed by water vapor (Figure 11). High levels of atmospheric water vapor could therefore result in a lower emissivity value for Band 10. Sulfur dioxide

output is also common from Soufrière Hills. A large absorption feature of the spectrum (Figure 13, 11) overlaps with that of the glassy spectrum and may deepen the emission value in Bands 10, 11, and 12. This may be compensated for by an atmospheric correction algorithm, specific to sulfur dioxide.

The reported absolute accuracy of the temperature product is 1-4° K and the relative accuracy is to 0.3° K at 300° K. The emissivity product is absolutely accurate from 0.05-0.1 and relatively accurate to 0.005. A quality assessment (QA) plane is common to all ASTER Level 2 products and includes Level 1B processing information. Pixels that fail certain algorithm processing are flagged in the QA plane. This failure can be due to a number of reasons described by an associated binary code for each pixel in the metadata. Pixels that are beyond the limitations of the instrument appear black in the image and are assigned a null value (Gillespie et al., 1999).

### **2.2.1. ii. Geostationary Operational Environmental Satellite**

The Geostationary Operational Environmental Satellite (GOES) program was started in 1974 as a joint effort between the National Aeronautics and Space Administration (NASA) and the National Oceanic and Atmospheric Administration (NOAA). These spacecraft, initially only observed weather patterns and the Earth's surface (GOES 1-3), however the recent satellites employ new technological innovations (Imager and Sounder instruments) for 3-D modeling of temperature and moisture content, and search and rescue capabilities (GOES 4-11) (2001). The GOES system is currently comprised of two geosynchronous satellites, GOES-8 (Goes-East) at 75° west



longitude and GOES-10 (GOES-West) at 135° west longitude, launched in 1994 and 1997, respectively (Harris et al., 2001b). Both satellites are positioned at an altitude of approximately 35,790 km and together cover 60 percent of the Earth, imaging approximately every 15 minutes (2001). Data are collected and received at the primary command and data acquisition station (CDAS), processed, transmitted back to the satellite and rebroadcast to users (2001). Data are available in five channels with various pixel sizes and band widths (Table 1).

### **2.3 Multi-parameter Database**

The database of volcanic activity provides a qualitative and quantitative foundation for the remote sensing image data as well as a means for statistical analysis of volcanic activity. The MVO provides current and archived information about Soufrière Hills on-line (<http://www.mvo.ms/>) intended for scientists, residents, and enthusiasts (Aspinall et al., 2002). Reports in the form of a weekly summary of volcanic activity from December 31, 1999 to April 11, 2003 were utilized and converted into a database (Appendix 1) using statistical software. The purpose of the database is to offer 1) a rapid means of viewing quantitative volcanic activity levels with a graphic representation for the week the image was captured, 2) a look-up table to view qualitative and quantitative data, and 3) statistical analysis in order to monitor trends of activity over an extensive period of time (two and a half years) on a weekly time scale.

Ideally, up-to-the-minute MVO monitoring information, such as seismic records, would provide the most accurate and desirable means of interpreting the remote

sensing image data. It is almost impossible to infer the activity level of the dome from the image data alone. For example, a thermal anomaly may represent a fresh and immediately exposed surface, or it may indicate an ensuing eruption, or the aftermath. Seismic signals record not only long-period, hybrid, and volcano-tectonic earthquakes, but also rockfall and pyroclastic events. These records would show the intensity and exact time of the event which could be matched to the time of the image capture, to provide a basis of interpreting the image data. These types of high temporal records were not available, so the weekly summary affords a qualitative baseline.

Other investigations have provided a foundation for the statistical analysis for these database. Positive correlations, listed below, include data points collected on a vastly different time scale than the database; sample times vary from minutes to hours or greater over study durations of days to weeks to months.

1. Gas venting and rockfall (Luckett et al., 2002)
2. Rockfall and long-period events (Cole et al., 1998)
3. Hybrid events preceding dome collapse (Neuberg et al., 1998)
4. Hybrid events preceding major explosions (Neuberg et al., 1998)
5. Long-period events preceding major explosions (Miller et al., 1998)
6. Hybrid events preceding rockfall (White et al., 1998)
7. Hybrid events linked to violent degassing (White et al., 1998)
8. Long-period events precede and follow hybrid events (White et al., 1998)
9. Collapses preceded by long-period and hybrid events (Neuberg et al., 2000)
10. Volcano-tectonic events are low during dome growth (Miller et al., 1998)

Correlations established on a weekly scale will have beneficial implications for a remote volcano with coarse temporal monitoring activities or revealing cyclic trends on larger time scales.

## **Section 3: Methodology**

### **3.1. Spaceborne Data**

#### **3.1.1 Image Processing**

All image processing was completed with the Environment for Visualizing Images (ENVI) software package (version 3.5) by Research Systems Inc. (RSI), except for an image to image registration technique or dome location, which was prepared with ArcGIS (version 8.2) by Environmental Systems Research Institute, Inc. (ESRI).

This study utilized ASTER Level 2 temperature and emissivity products because these are atmospherically and radiometrically corrected. The six images showed good agreement between Level 1B (non-atmospherically corrected, registered radiance at sensor), Level 2 AST 09T data separated with the emissivity normalization technique using an assumed emissivity value of 0.985, and Level 2 AST 05 and AST 08 products. Surface kinetic temperatures compared between the different data processing levels were within one to one and a half degrees K, except for one anomalous pixel near instrument saturation in Jan 13, 2001 image. The shape of the spectra of the four hottest pixels per scene were the same between data sets, except for a minor y-axis scaling difference due to the additional atmospheric correction or additional removal of down-welling sky irradiance with the Level 2 product (Gillespie et al., 1999).

The number of images collected by ASTER that included the Soufrière Hills dome totals thirty-seven from March 29, 2000 to June 12, 2003. From those images, six scenes (Table 3) were chosen based on a low percentage of cloud cover over the dome

area and complete imaging of the summit dome within the scene boundary (Figures 14-19). The only exception is the image from October 29, 2002, which shows the dome partially covered with clouds, but also has an anomaly over the dome center (Figure 19). ENVI version 3.5 does not automatically apply geographic information to the ASTER Level 2 product. Geographic and image data are found in the metadata accompanying each image and were applied to a new working image by editing the header parameters. The following steps outline the image preparation process and are included for the purpose of detailing the procedure. However, newer releases of the ENVI software now handles all of the following automatically.

1. For the AST 05 product, correct band numbers and wavelengths were assigned. ENVI assigns bands 10-14 as 5-1 (if bands are not re-ordered) in the new image. The wavelengths are not preserved and are reported in the header as "0.000". This step is not necessary for the AST 08 product because temperature is reported and loaded in one temperature "band".

band 5 → band 10 = 8.291  $\mu\text{m}$   
band 4 → band 11 = 8.634  $\mu\text{m}$   
band 3 → band 12 = 9.075  $\mu\text{m}$   
band 2 → band 13 = 10.657  $\mu\text{m}$   
band 1 → band 14 = 11.318  $\mu\text{m}$

2. Geographic information is edited under map registration. Image coordinates are enter as 0.5 for the X and Y parameters to center the geographic data in the upper left corner pixel (Figure 20). The map rotation angle was also entered with a positive number for nighttime images and a negative angle for daytime images.

This number may be incorrect in the metadata and can be easily fixed by inverting the positive or negative sign in the header. All images were then projected into UTM, Zone 20 North with a datum of WGS-84.

3. Pixel size was entered as 90 by 90 meters.
4. Sensor type was changed to ASTER.
5. The band scale factors are found in conjunction with the AST 09T product metadata and were applied to convert to decimal numbers (float command) and to scale data by using the band math option with the following formula:

$\text{float}(\text{band\#}) * \text{band scale factor}$

band 14 = 0.005225  
band 13 = 0.005693  
band 12 = 0.006590  
band 11 = 0.006780  
band 10 = 0.006882

6. The AST 05 product output was scaled into the correct range of emissivity:

$\text{band\#}/1000$

7. The AST 08 product was scaled into the correct range of temperature using:

$((\text{float}(\text{b1})/10) - 273.15)$

The GOES non-atmospherically corrected band 4 data were read into ENVI with the following information and required no further image processing:

1. lines and samples: 500 x 500
2. 1 band
3. data type: integer
4. byte order: IEEE

In total, for each ASTER image, eight GOES data points were used that span one hour prior to and hour of ASTER image capture. The only exception was from August 3, 2002, where three GOES data points were unavailable (Table 2).

### **3.1.2 Georectification**

In this case, exact geographic location of the dome in each ASTER image was highly desirable to compare pixel-by-pixel surface changes over time. However, due to metadata or other inaccuracies, exact positioning may not be possible. It was unfeasible to place precisely where within or near English's Crater the anomaly lies because the crater walls are not distinguishable at 90 meter resolution. Initially, a digital topographical map (1996) was manually merged onto each image, by aligning the coastline features and became a template for dome location (Figures 14-18).

Three georectification methods were investigated to correct geometric inconsistencies including 1) an image to image transformation with the RST (rotation, scaling and translation) technique, 2) a point to point warp and geo-rectification to the base topographical map using the ArcMap extension of ArcGIS, and 3) a reversal of the geographic corner points. The RST method requires the user to identify common ground control points between each scene and a common base scene to slide in 2-D space one image to another without warping which can change the values of the pixels. The 90 meter resolution and vague appearance of the land and water boundary only allowed approximately five or six points to be identified throughout the whole scene, which asymmetrically stretched the scene and produced geographic errors. Resampling

each image to 15 meter pixel sizes provided only modest improvement. The second method, similar to the first, was done using ArcMap with the topographic map providing the base image because the coastline was well outlined. The daytime image (Figure 21) was used as the initial base map to assign geographic points to the topographic map. Each image, including April 13, 2002 was then warped to the topographic map by the point-to-point method, similar to selecting ground control points, except that the topographic map can be essentially slid over the image first. This technique allows for greater matching accuracy because irregular or distinct areas around the coastline are readily identified. Great care must be taken in the southern and south-eastern portions of the island because of the dramatic change in the coastline from the build-up of pyroclastic deltas from 1996 to present. Although several ground control points were entered, the accuracy of the method degrades towards the dome, or the interior of the island, and cannot be quantified. This is because the accuracy decreases the further away from the control points. The third and final method was explored due to a reported error in the metadata concerning the possible reversal of one or more geographic corner points, particularly with nighttime data (M. Ramsey, personal communication, 2003). Only one of the six images (April 13, 2002) was found to contain this error (reversed upper right and lower right longitude values). This final step is required to correct the processing error and resulted in the least image to image geographic error. Each image was then cropped by the same input geographic corner points to isolate the dome (Figures 14-18) and to make each image more manageable. The geographic location of the island of Montserrat was the same in each GOES image.

Approximately four pixels in the center of each image covered the entire island, so the lower right-hand pixel was consistently chosen for analysis because it contained the volcano.

### **3.1.3 Spectral Deconvolution**

The methodology used in this study is based upon Ramsey and Fink (1999) who used two spectral end-members to identify areal percentage of glass (obsidian end-member) and vesicles (blackbody end-member). These end-members were degraded to the TIR spectral resolution of ASTER (Figure 22). The glassy end-member is adapted from a laboratory spectrum of Ramsey and Fink (1999). That spectrum has a maximum depth of 0.70, however this study used a spectrum with a reduced depth of 0.85. This accounts for the laboratory derived versus image derived spot size (2 cm versus 90 m). Each image was deconvolved against the two end-members resulting in three images: the areal percentage data for each end-member and the resulting root-mean-square (RMS) error. The corresponding temperature and emissivity images (Level 2, AST-08 and AST-05 products) were linked to all three output images for consistent location of the same pixel over all four images. The temperature image was used to locate the four hottest pixels within the anomaly and an additional “off-dome” pixel at background temperature (Figures 23-28). The glass, blackbody, and RMS error data were recorded for each of selected pixels. The emission spectra were also recorded (Figures 29-34). A density slice color map was created for each of the blackbody and glassy images to



illustrate the distribution of percentages of vesicles and glass over the whole dome and surrounding surface (Figures 23-28).

#### **3.1.4 GOES and ASTER temperature comparison**

ASTER non-atmospherically corrected Level 1B radiance images and atmospherically corrected Level 2 AST\_08 temperature images were spatially resampled to mimic the 4 km resolution of GOES band 5, by multiplying the x and y factors by 0.0225 (Figure 35). Temperature and emissivity were first derived from the ASTER Level 1B radiance data using the normalized emissivity technique with an assumed emissivity value of 0.985 (Salisbury and D'Aria, 1992). ASTER temperatures from the pixel including the dome were compared to a series of eight GOES temperatures from the pixel including the dome and entered on a spreadsheet (Table 2).

### **3.2 Database Development**

Data contained within weekly summaries of volcanic activity from December 31, 1999 to April 11, 2003 were converted to a database (Appendix 1) and analyzed using the Statistical Package for the Social Sciences (SPSS). Key words or phrases (qualitative variables) were identified in each report and assigned a value under a related column heading (Appendix 2). Quantitative data, or number of weekly occurrences, were entered as reported by the weekly summary. Statistical analysis was then performed on variables that have previously been shown to positively correlate by other investigators.

The majority of the summary reports contained the same basic qualitative (categorical) and quantitative (numerical) data. However, there were some exceptions that translated into either assumptions or missing data points. Categorical data was broken down into a range of activity and assigned variables, whereas the majority of the quantitative data was entered as the reported weekly total (Appendix 2). Preliminary boxplot analysis (Appendix 3) showed hybrid earthquake totals (quantitative data) tended to fall within two categories: “low” values or 25 occurrences or below and “high” values, or 26 occurrences and above. A second, third, and forth column of categorical hybrid data (each with a different threshold) was added to accommodate for the dichotomy of values and to contribute different statistical information. In cases where categorical variables have multiple values, the value representing a more extreme behavior was chosen. For example, if dome growth was “small” and “moderate” for equal periods during the week, “moderate” was entered as the value. Reporting of dome growth and the occurrence of spines and lobes depends largely on observational opportunities and may be missing from the summary data. These data points, therefore, are missing and not assumed to have not occurred. Direction of dome growth or pyroclastic flow was missing if unobserved, multi-directional, or un-directional. In the multi-directional case, either an obviously dominant direction was chosen or a variable representing the multi-directions was chosen. Sulfur dioxide data was reported in tonnes per day as one value, a range of values, or multiple ranges of values. The weekly minimum and maximum of a range or ranges are recorded in the database as the corresponding value. Where one value was reported, that value was

recorded as both the minimum and maximum values to assist in maintaining consistency from one summary report to the next. Several sulfur dioxide values are missing due to instrumentation problems, weather difficulties, or volcanic activity. No values are recorded in the database where these values are missing. Tectonic earthquake values are generally few, ranging from zero to forty-three occurrences with an average value of three. Rarely tectonic earthquake information was missing from the summary, so a value of zero was entered in the database. Averages were calculated for the numerical data for the time constraints of the database. Long rock signals were first reported in the weekly MVO summaries the week of January 26, 2001, hence the missing values prior to this date did not contribute to the average. The sulfur dioxide variable was missing several data points. The average was calculated using only values present in the database.

Below is an example of a weekly summary generated by the MVO (activity reports archive) and the corresponding database entry. In the summary report, numeric data are underlined and key categorical words or phrases are in bold.

Report for the period midday, 22 December 2000 to midday, 29 December 2000

Activity at the Soufrière Hills Volcano has remained at an **elevated** level this week with continued **growth of the lava dome** and **high** levels of rockfall activity.

The level of seismic activity remains high. The broadband seismic network recorded a total of 708 rockfall signals, 2 volcano-tectonic, 53 long period and 10 hybrid earthquakes for the reporting period. Rockfall signals were often immediately preceded by long-period events, indicative of explosive onsets. This was confirmed by visual observations of **vigorous ash venting** prior to and during rockfall activity.

Some spectacular views of the dome were obtained this week. Growth continues in the summit area with a large amount of rockfall debris being shed down the **eastern** face of the dome. A small amount of rockfall activity occurred down the **south** side entering the upper reaches of the **White River Valley**. Rockfall activity also occurred in the **western area of the new growth**, although the rockfall debris was still contained by the old dome complex. The summit area evolves continuously but has been dominated by a large **spine** over 60m tall. The top of the spine reached 1071m above sea level.

COSPEC measurements on 28 December indicate an average sulfur dioxide flux of 745 tonnes per day. Values of up to 1100 tonnes per day were recorded following large rockfalls from the dome.

Wind conditions this week have resulted in a small amount of ash being deposited in inhabited areas in the north and west of the island. Whilst this does not reflect an increase in activity, all precautions should be followed when cleaning or dealing with the ash. Ash masks should be worn in ashy conditions or when you disturb ash. Rockfall and pyroclastic flow activity is likely to remain at a high level whilst the dome continues to grow, producing ash clouds which may blow over inhabited areas.

Residents of Montserrat and visitors to the island are advised to tune in to ZJB Radio for up-to-date information on the status of the volcano. Elevated levels of pyroclastic flow activity may develop very rapidly and could affect any valleys around the volcano. In addition to the risk from pyroclastic flows, the Belham valley should also be avoided during and after periods of heavy rain. Everyone is reminded that access to Plymouth, Bramble airport and beyond is prohibited. There is a maritime exclusion zone around the southern part of the island that extends two miles beyond the coastline from Trant's Bay in the east to Garibaldi Hill on the west coast. The daytime entry zone remains closed.

MVO wishes the residents of Montserrat all the best for the New Year.

12 noon, Friday, 29 December 2000

The database column heading is in bold and the variable is immediately following:

**Row 51, date** 22-Dec-00, **day** 358, **aster** 1, **dgrowth** 1, **dsize** (no entry, missing data), **dpat** 1, **directio** (no entry, missing data), **pyrsize** 0, **pyrsource** 0, **dir2** 0, **ash** 1, **explo2** 0, **explo** 0, **fume** 0, **glow** 0, **rkfl** 708, **lonrk** (no entry, missing data), **hy** 10, **loneq** 2, **min** 745, **max** 1100, **nhy** 1, **hy2** 0, **hy3** 0, **mud** 0 (Appendix 1).

Statistical analyses of the eleven pairs of variables are based upon correlations found by the indicated investigators. A clustered boxplot (Appendix 3) was applied to each variable pair to locate any promising relationships on the weekly time scale, prior to more in depth statistical analyses. If a correlation was identified, one of the following operations was performed:

1. categorical vs. categorical
  - a. two-way table
  - b. chi-square
2. numerical vs. numerical
  - a. scatter plot
  - b. regression
3. categorical vs. numerical
  - a. boxplot
  - b. independent sample t-test or ANOVA

Line graphs of the numerical data were created as quick visual reference for the image data (Figures 36-40). Large explosive events and image acquisition were also represented in each graph with a bar. A smoothing curve, using the centered moving average technique, was run on the data to help identify the trends. A centered moving average of 5 (hybrid earthquakes, long period earthquakes, and long rockfalls) averages the values of each data point with two consecutive values to the right and two to the left of the original value. If the average or span was even, each pair in the group was averaged based upon the uncentered means. The centered moving average for rockfalls was ten and for volcanic tectonic earthquakes the average was seven. Sulfur dioxide maximum and minimum values are represented by a bar graph (without a centered moving average) because of so many missing values (Figure 41).

## Section 4: Results

### 4.1. Statistical analysis of the database

Statistical analysis demonstrated three out of eleven previously established variable relationships showed correlations on a weekly time scale and are detailed below:

1. **Gas venting and rockfall (Luckett et al., 2002)** (Figure 42). Regression and ANOVA tests reveal a best line of fit as  $y = 353.986 + 0.164x$ , a p-value of 0.002, and an f-value of 10.375. Approximately five points were outliers (anomalously high values) and were not removed.
2. **Hybrid events preceding major explosions (Neuberg et al., 1998)** (Figure 43). No correlation was found with these two variables, except where hybrid activity was separated into two groups based on occurrence, below 25 and 26 and above. Fisher's exact test shows a p-value of 0.008 between explosive behavior and a high number of hybrid events.
3. **Hybrid events preceding rockfall (White et al., 1998)** (Figure 44). A t-test showed that the average number of rockfalls was fewer with high values of hybrid events (26 occurrences and above) with a t-value of -3.2 and a two-tailed p-value of 0.002.

The other eight variable relationships did not show correlations with preliminary statistical analysis (boxplots) and therefore were not further analyzed. The full statistical

analyses for all ten correlations, including the boxplots, graphs, and tables, can be found in Appendix 3.

Average values for the numerical variables in the database are as follows: rockfall signals 444, long rock seismicity 40 (starting week of January 26, 2001), long period earthquakes 63, volcano-tectonic earthquakes 3, hybrid earthquakes 55, sulfur dioxide minimum value in tonnes per day 332, and sulfur dioxide value in tonnes per day maximum 686.

## **4.2 Spectral Deconvolution and Dome Characterization**

In all six images, the active dome was considered to be at least to the size of English's crater. Data within English's Crater and the immediate vicinity are therefore characterized with the spectral deconvolution results, spectral profiles, temperature, and database results. Areal percentages of blackbody and obsidian for the four hottest (non-saturated) pixels and one pixel on the flank of the volcano are shown in Table 4 with the corresponding spectra in Figures 29-34. This table compares the deconvolution results, RMS error, and temperature distribution of the potentially most active area of the dome to the corresponding spectral results. Figures 23-28 are image subsets of the dome area to show the distribution of temperature, and areal percentages of blackbody (the proxy for vesicles) and glass across the entire dome and immediate vicinity using a density slice. Bright pixels in the blackbody and glassy end-member images represent high percentages of those end-members and dark pixels represent lower values, whereas bright pixels in the RMS error image represent high error and dark pixels

represent low error. A unit sum constraint was used with a weight of 1.000 to fit the unmixing results to 100%. Physically implausible results with respect to deconvolution of the two end-members are considered to be percentages falling below 0 and above 100%. The following entries are summaries of the result of each image.

**November 1, 2000.** The image from November 1, 2000 shows elevated temperatures above background (0-24°C) within approximately 60% of English's Crater (Figure 23). Temperatures above 50°C are concentrated in a small area, suggesting localized activity. Temperatures ranging from 25-49°C are distributed east and west of the central anomaly. The database entry from this week supports the temperature data because dome growth and localized spines were observed. Dome growth was concentrated east-northeast, and west of the central part of the dome. Rockfall occurrences were low (less than 150 occurrences) (Figure 36), and originated from material shed from the growing dome. This is in good agreement with the temperature distribution. Long period and hybrid episodes were both well below average for the week (Figure 38 and 39). Volcano-tectonic signals occurred at the overall average value of three (Figure 40). Sulfur dioxide measurements were unavailable and ash plume(s) below 10,000 ft and dome incandescence were observed.

The spectral deconvolution results (Table 4) shows two sets of pixels of similar temperature: 1 and 2 at 109°C and 2 and 3 at 98°C. The spectra from the high temperature pixels (Figure 29) have data points outside of the boundaries of the end-members (Figure 8), but only pixels 2 and 3 have points below the depth of the absorption feature, in band 12. A sulfur dioxide plume is not present in this image



(Figure 14) and therefore the depth of the spectrum is likely a result of large sub-pixel temperature variations (pixels 1, 2, and 3 also show a drop in Band 14). The deconvolution results for these two pixels are beyond the 0-100% range, with blackbody results falling below 0% and glassy results are greater than 100%. The vesicularity distribution image (Figure 23) shows vesicularity ranging from 0-70%. The glassy percentages ranged from 0-100% (Figure 23). RMS error is variable, though low, throughout the image subset and increases slightly towards the thermal anomaly (Figure 23).

**December 28, 2000.** The December 28, 2000 temperature data illustrates elevated temperature above background within the entire boundary of the crater (Figure 24). Several pixels appear black because the original radiance values were above the saturation temperature for the detectors. Data concerning the size and direction of dome growth was unavailable, so it cannot be correlated with the temperature distribution. Rockfall occurrence was well above average and therefore the dome growth rate is most likely high (Figure 36). The reported minimum and maximum tonnes of sulfur dioxide were elevated well above average (Figure 41). A large plume is visible in the full image (Figure 15) and is represented by a cluster of pixels in the lower left-hand corners of Figure 24.

The four pixels plotted in the spectral unmixing results table (Table 4) are all within about three and a half degrees of each other, ranging from 107-111°C. The spectra from all four pixels have data points outside of the boundaries of the end-members, but only pixel 2 does not constrain the end-members to 100%. The data

point for Band 12 (pixel 2) lies below the threshold of the end-member Band 12 data point. All four pixel spectra include a drop in Bands 13 and 14 (Figure 30). The vesicularity distribution image (Figure 24) shows vesicularity ranging from 0-90%. Vesicle percent outside the 0-100% range extend past the saturated pixels. The glassy end-member ranged from 0-100% (Figure 24). The RMS error is very low for roughly 75% of the dome and all of the surrounding area (Figure 24).

**January 13, 2001.** The January 13, 2001 image consists of a very concentrated thermal anomaly (450m x 450m) in the south central portion of the crater (Figure 25). Two of only 19 thermally elevated pixels are saturated (black). The remaining portion of the dome and surrounding area is at background temperature (0-24°C). This is in contrast to the November 1, 2000 image, which shows evidence of rockfall activity east, towards the Tar River Valley (Figure 3 and 23). The dome growth was moderate and concentrated in the southeast with no evidence of lobes or spines. Pyroclastic activity was small or light from an unknown source and was directed towards Tuitt's Ghaut, or north-northeast (Figure 3). Rockfall was high with over twice the average weekly occurrences (Figure 36). No hybrid seismic signals were reported by the observatory (Figure 38). Values for long earthquakes and sulfur dioxide were well below average (Figures 39 and 41).

The four pixels plotted in the spectral unmixing results table (Table 4) range in temperature from approximately 81-109°C. The spectral deconvolution results for the four highest temperature pixels all fall within the 0-100% range for both end-members possibly indicating a relatively homogenous sub-pixel temperature. The ratio of glass to

vesiculated rock is very variable for these four pixels and the immediate vicinity surrounding the high temperature anomaly. The emission spectra (Figure 31) all show a drop off at longer wavelengths, not just a drop in Band 14. The Band 12 data point lies below the threshold of that of the glassy end-member, possibly due to absorption from water vapor. The vesicularity distribution image (Figure 25) shows values ranging from 0-90%. The glassy end-member ranged from 0-100% (Figure 25). Only four pixels in the entire scene, other than the saturated values, fall outside of the 0-100% range (Figure 25). The RMS error is comparatively low and increases towards the anomaly (Figure 25).

**April 13, 2002.** The April 13, 2002 image shows elevated temperatures above background within approximately 60% of the crater (Figure 26). This image was a daytime scene (Table 3) and has a higher background temperature than any of the three previous images. A large plume is easily detected in Figure 17. Figure 26 shows the plume, bottom left, as a cooler temperature than the land surface. The activity illustrated by the image is similar to that of December 28, 2000 (Figure 24), except for the larger concentration of high temperature pixels immediately surrounding the saturated area (Figure 26). During the week of image acquisition, the dome was growing to the southeast although the degree of growth was unobserved. Spines were observed and active. Rockfall activity was almost twice the weekly average (Figure 36). Long rockfall signals, hybrid earthquakes, and long earthquakes were only slightly elevated (Figures 37, 38, and 39). There were no reported occurrences of tectonic earthquakes (Figure 40). Only one sulfur dioxide value was present in the MVO weekly

summary. This value, almost double the average, was entered in the database as the minimum and maximum values (Figure 41).

The four pixels plotted in the spectral unmixing results table (Table 4) have the same high temperature of 109°C. The pixel 1 (Figure 32) spectrum is shaped almost identically to the glassy end-member but the absorption feature in Band 12 extends beyond that of the end-member to a depth of 0.84 and there is a noticeable drop-off at longer wavelengths. The deconvolution results show an almost entirely glassy pixel with slightly negative amount of blackbody to compensate for the depth of Band 12. Pixel 4 has a similar shape with a slightly higher value, 0.85 emissivity in Band 12 and a relatively slightly lower value in Band 11. All four pixels are sloped to longer wavelengths. The blackbody and glassy end-members are not constrained to 100%, however are slightly below 0% and above 100%, respectively. Overall, Figure 26 results illustrate a very glassy and non-vesiculated dome and vicinity. The RMS error is comparatively low and again increases towards the anomaly (Figure 26).

**August 3, 2002.** The August 3, 2002 image, the second daytime image, shows a very small anomaly (<10% of the crater area) at the western edge of the crater. Three pixels are saturated and clustered within the anomaly (Figure 27). Cloud cover extends over the dome area but does not seem to interfere with the anomaly (Figure 27). Pixels above background temperature extend north and east of the crater. The pixels to the north are not adjacent to one another or within the active dome area. This likely does not indicate an event in progress because of the discontinuous anomaly, but possibly the after effects. The database indicates very elevated activity concerning the

active dome itself. The dome grew at a high rate to the north and produced lobes and/or slabs. Small or light pyroclastic flows originating from the dome were observed traveling in the direction of Tyre's Ghaut to the northwest (Figure 3). Rockfall activity was low, occurring well below the average (Figure 36). Tectonic, long rockfall and hybrid values were also below average (Figures 37, 38, and 40). Long earthquake occurrences were high, occurring more than twice the average value (Figure 39). Sulfur dioxide minimum and maximum tonnes per day values were elevated slightly above average (Figure 41).

The four pixels plotted in the spectral unmixing results table (Table 4) range in temperature from approximately 87-109°C. Deconvolution results for pixels 1-3 are not constrained to 100%. Pixel 2 in particular shows a reversal in the end-member percentages from previous results because the blackbody percentage is greater than 100% and the glassy percentage is less than 0%. One feature (higher emissivity values in Band 11 compared to band 10) of the Pixel 2 spectrum is different from every other spectrum (across all six images). This spectrum was derived from pixels in which the deconvolution results fall out of the 0-100% constraint. Other spectra also show this trend, but have end-member results within the 0-100% range and also do not show a significant Band 14 drop. Pixels 1 and 3 show a drop-off towards longer wavelengths. The vesicularity and glassy distribution images (Figure 27) show that both end-members range from 0-100% across the dome in no particular pattern. The RMS error is relatively low and also not distributed in any particular pattern except for the slight increase towards the anomaly (Figure 27).

**October 29, 2002.** The October 29, 2002 image shows a small anomaly in the western portion of the crater, similar to the August 3, 2002 image, but much less intense (Figure 28). This image was acquired in the daytime (Table 3). The cooler temperatures observed in most of the scene (Figure 28) are due to extensive cloud-cover, ash or sulfur dioxide over the dome area. There appears to be little dome activity derived from the distribution and temperature of the anomaly, but due to the extensive vapor or gas cover, this is only speculation. The database information shows that the dome was growing to the northwest but the rate and size were not observed. Lobes and/or slabs were observed to be active. Pyroclastic flows were moderate or steady, from an unknown source, and directed towards the Tar River Valley to the east and Tuitt's Ghaut, to the north (Figure 3). Rockfalls and long rockfall seismic signals were above average (Figures 36 and 37). Hybrid earthquakes were well below the average and tectonic signals were slightly below average (Figures 38 and 40). Long earthquake occurrences were over twice the average value (Figure 39). The sulfur dioxide minimum value (tonnes per day) was well below average whereas maximum values were only slightly below average (Figure 41).

The four pixels plotted in the spectral unmixing results table (Table 4) range in temperature from approximately 64-79°C. The spectral deconvolution results for these four pixels all fall outside of the 0-100% range for both end-members. The emissivity scale for Pixel 4 (Figure 34) is completely beyond the 0-1 scale which represents a failure of the TES algorithm for that pixel (Gillespie et al., 1999) and therefore invalid results. Pixels 1, 2, and 3 (Figure 34) all have data points in Band 12 well below that of

the glassy end-member. This could be the result of sulfur dioxide or water vapor absorption. All four pixels include flat spectra from Band 12 to band 14, possibly resulting from two-temperature mixing from active lobes/slabs. The majority of the pixels corresponding to the thermal anomaly fall outside of the deconvolution constraints. The vesicularity distribution image (Figure 28) shows vesicularity ranging from 30-60%. The glassy end-member also ranged from 30-60% (Figure 28). The RMS error immediately surrounding the anomaly is comparatively low and increases directly over the anomaly (Figure 28).

#### **4.3 GOES and ASTER Temperature Comparison**

GOES-derived temperatures are consistent per image (15 minute intervals over two hours) and across all six scenes, which span a two-year period (Figure 45). The temperatures for all of the scenes range from 28.42°C to 29.53°C with an average temperature of 29°C. ASTER Level 1B non-atmospherically corrected temperatures are consistently lower than the GOES results with the difference ranging from 1.7°C to 13.7°C below the GOES values. Atmospherically corrected ASTER Level 2 temperatures do not plot consistently higher or lower than GOES values and have a range difference of 1.6°C above to 13.7°C below that of the GOES-derived temperatures.

## Section 5: Discussion

The spectral deconvolution results (Table 4) show a variability of areal percentages of dense glass and vesiculated rock within each image and from image to image (Figures 23-28). Generally, however, all images show a tendency towards lower vesicularity and higher glass content, which is in fair agreement with the petrographic data (Formenti and Druitt, 2003) and observations by MVO staff. There are also no readily apparent patterns of vesicularity or relatively large areas of high vesicle concentration as was found with the Holocene flow results by Ramsey and Fink, 1999. Very small concentrations of 80-90% vesicularity immediately surround the high temperature anomaly in four of the six images (Figure 23, 24, 25, and 27) and may be due to the sub-pixel temperature mixing. Areas to the northeast and east of the dome are preferential for rockfall and pyroclastic activity (Figures 23-28) due to lower relief. Areas in all other directions are less active and therefore may show changes in vesicularity with time, possibly indicating an increase in hazard potential. The December 28, 2000 image was acquired approximately two months after the November 1, 2000 image. An area (approximately 900 m by 500 m) of 30-40% vesicles is observed on the north-northwest flank of the December 28, 2000 image, which is an increase in vesicles from about 10-30% from the November 1, 2000 image. The database (Appendix 1) entries between the image acquisition dates include two collapse events. One of these events was directed east whereas the direction of the other was not observed. Pyroclastic flows traveled north and northwest during this time and may account for the



surface change. The images acquired on December 28, 2000 and on January 13, 2001 are less than one month apart. The area immediately north-northwest of the dome is similar in areal percentage with both end-members but more pixels in the January 13, 2001 image show a high vesicle content. The activity database (Appendix 1) indicates the dome was growing and produced lobes and slabs. The direction of the activity (pyroclastic flows and rockfall) was not observed, so whether or not the surface was recovered by new material is inconclusive. The change of the surface texture may indicate an increase in hazard potential nevertheless. The only other set of images acquired within a few months of each other are from August 3, 2002 and October 29, 2002. The October 29, 2002 is too cloudy for comparative surface analysis.

Table 4 shows areal abundances of the end-members for only the four highest temperature pixels outside of any saturated areas and one pixel off-dome at background temperature. Figures 29-34 display the emission spectra of each of those five pixels. The spectral deconvolution algorithm constrains the unknown spectrum to within the boundaries of the end-members (Figure 8) and produces an RMS error that indicates how well the model fit the data. If most of the unknown spectrum data points fall outside of this boundary, then the resulting RMS error is high and the end-member percentages become unreasonable. Not all data points have to be constrained by this boundary to produce reasonable percentages however (Figures 29-34). Sources of this error may be a drop in one or more of the longer wavelength bands (Ramsey and Dehn, 2003), an increase in emission from Band 10 to 11 from sulfur dioxide and/or water vapor, or perhaps an additional end-member present on the surface and not

accounted for in the model. Pixels corresponding to end-member abundances outside of the 0-100% range (Figure 29 pixels 2 and 3, Figure 30 pixel 2, Figure 32 pixels 1, 3, and 4, Figure 33 1-3, and Figure 34 pixels 1-4) reveal a spectral trend, irregardless of these previously mentioned error sources. In each case but two, the data point for Band 12 is below that of the end-member. This suggests that the five emission data points for the glassy end-member are too high, i.e., the entire spectrum needs to be shifted down to resemble laboratory data of glass. Shifting the end-member spectrum will skew the results however, causing a false increase in glass and a false decrease in blackbody. The two pixels that do not follow this trend are pixel 2 (Figure 33) and pixel 4 (Figure 34). Pixel 2 shows a large drop in emissivity from Band 12 to Band 14 and an increase in emissivity to 0.97 from Band 10 to Band 11. Combined, this produces a very large error and greater than 100% blackbody to resolve. Pixel 4 is scaled beyond emission of 1, to 1.42, which suggests an error in the initial Level 2 data processing algorithm or TES (Gillespie et al., 1999). Pixels that display a drop in Band 14, indicative of two-temperature sub-pixel radiance mixing, do cause end-member percentages to fall outside of the ideal range. The data point for Band 12 may be erroneously high, but the data point for Band 14 may compensate and still produce an accurate abundance of each end-member.

The GOES temperature data does not agree well with that of ASTER Level 1B derived temperature or the Level 2 temperature product. The GOES data was not atmospherically corrected and therefore should correspond most closely with the ASTER Level 1B data, which is not atmospherically corrected. The difference in temperatures is

very variable from image to image. These differences could be due to the higher variability in surface temperature detected with ASTER as opposed to the km-scale averaging of temperature in the GOES data. This variability is what makes the ASTER TIR much more ideal for monitoring and modeling thermal flux from small-scale volcanic features.

## **Section 6: Conclusions and Future Work**

In general, the areal abundances of glassy and vesiculated end-members agree with observations and the aforementioned petrographic study (Formenti and Druitt, 2003). Six images over a two year period provided information on the evolution and distribution of surface glass and vesiculated rock. This time series, although coarse in temporal resolution shows the development of a more vesiculated dome. Although the majority of pixels revealed plausible end-member percentages, the accuracy of the percentages is not completely constrained. Small errors, especially with respect to the very hot pixels, are likely caused by 1) an absorption in Band 10 caused by atmospheric water vapor, 2) a deepening of spectrum in Bands 10 and 11 due to the presence of sulfur dioxide, 3) less significant emissivity in Band 12 of the glassy absorption feature than that of the end-member, 4) the presence of an unaccounted for end-member, and 5) the drop-off of the spectrum at long wavelengths due to elevated sub-pixel temperatures (i.e., exposed magmatic surfaces or fumarolic activity). Although

implausible results center on very small areas of the dome, the errors and solutions still need to be addressed.

Three techniques are proposed to correct for these errors and assess the accuracy of the spectral deconvolution results in the future: 1) eliminate Band 10 from the analysis to remove atmospheric effects, 2) use the inverse Planck equation to account for sub-pixel temperature mixing prior to analysis of the derived emissivity spectrum, and 3) obtain direct measurements of the active dome using a field-based radiometer with the same spectral resolution of ASTER. The latter would provide an accurate glassy end-member spectrum, account for small scale thermal anomalies, and detect the presence of atmospheric water vapor and/or sulfur dioxide. The last proposal will also help identify a possible third end-member by accessing hand samples of dome material. The overlapping absorption feature of the glassy end-member and sulfur dioxide may not be conducive to adding sulfur dioxide as a third end-member. Possibly an atmospheric correction algorithm specific to sulfur dioxide can be applied to those images containing a plume. Fieldwork, that addresses proposal #3, has been planned for this study (Kuhn and Ramsey, 2002) and will likely contribute to the accuracy assessment of the spectral deconvolution results. The highly active state of the volcano has made this difficult.

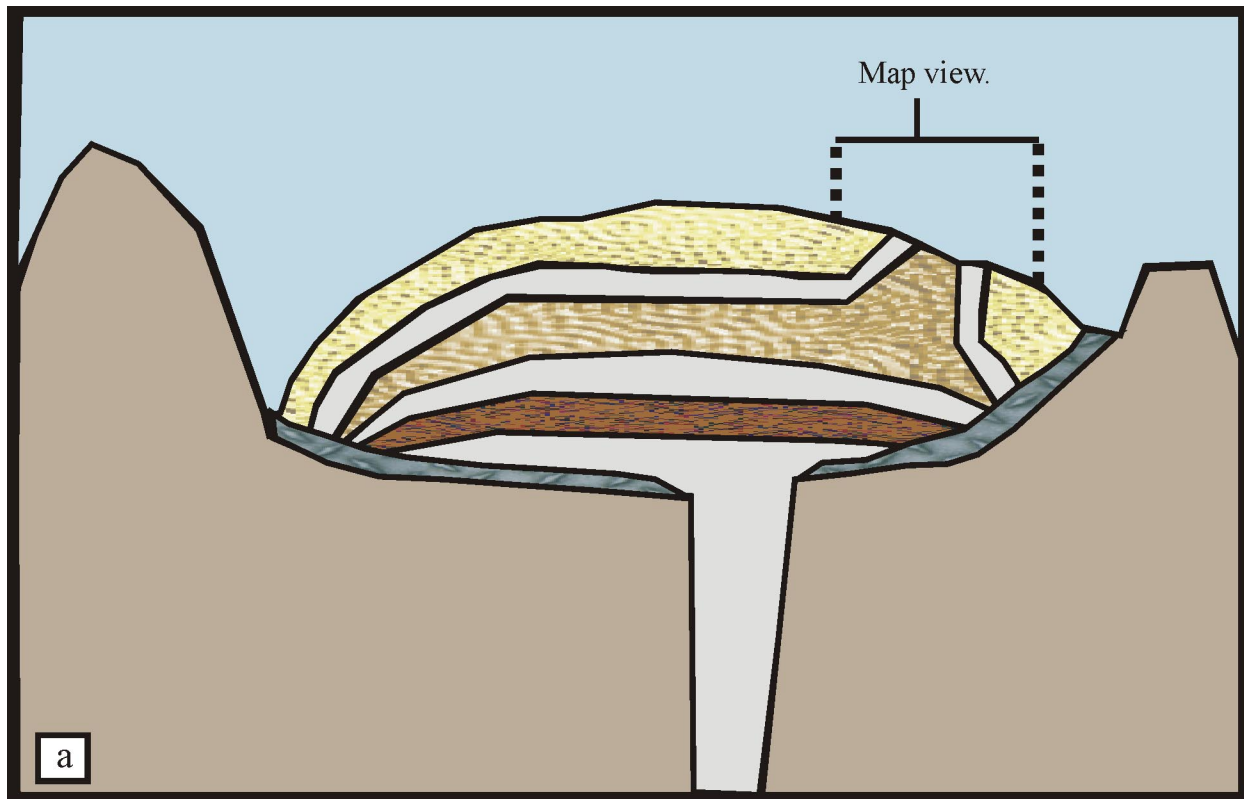
ASTER has contributed a new data set that can be utilized for assisted monitoring of Soufrière Hills and offers a new perspective to the characterization and evolution of dome processes. Due to the very coarse temporal coverage of the image data and the very active state of the volcano, end-member distribution patterns

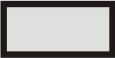
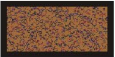



discerned on the dome and vicinity are likely non-sequential, except for images November 1, 2000 and December 28, 2000. Hazard assessment is therefore difficult, but possible as areas of increased vesicularity have been identified. Increased temporal resolution of cloud-free or nearly cloud-free image data would greatly increase accurate hazard assessment. Although this is largely due to chance, assigning ASTER to high priority mode will increase coverage and improve hazard assessment. ASTER has provided new data that cannot be discerned from ground based measurements, and which will greatly improve the study of active dome growth. For the first time, the distribution of thermal anomalies, glass, and vesiculated rock over the dome and vicinity has been evaluated.

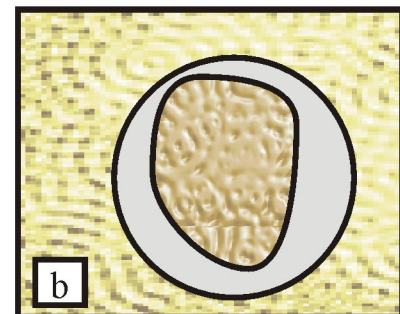
GOES does not appear to be a viable means of enhancing the temporal resolution of ASTER. ASTER results revealed a wide range of temperatures with the six images over the two year period, comparable to the range activity levels of the volcano. GOES revealed relatively steady temperatures over the two years. The spatial resolution of GOES is too large to discern smaller scale temperature fluxes as evident with ASTER at Soufrière Hills. Further, the temporal resolution of ASTER is too poor to track long term trends in thermal flux as compared to GOES.

The activity database does not always provide enough information for image assessment because of the temporal resolution, but does provide a great basis for reference. Seismic data could provide the best information to accurately evaluate the activity state of the dome because of high temporal resolution (Menand and Tait, 2001; Neuberg et al., 1998; Neuberg et al., 2000). Seismic signals also provide information on

the sub-surface processes, which where linked to surface features discerned by remote sensing techniques, provide the most comprehensive model. The database does, however, provide a very good reference for characterizing the dome from image to image, and overall trends in behavior. Statistical analysis showed correlations on the weekly time scale. Likely, with further data mining techniques, more correlations will be identified. This offers a new look into characterizing activity long term and discerning patterns and cycles, with a temporal resolution often not used in analysis. The database coupled with the image data does augment and improve lava dome characterization of the Soufrière Hills volcano.

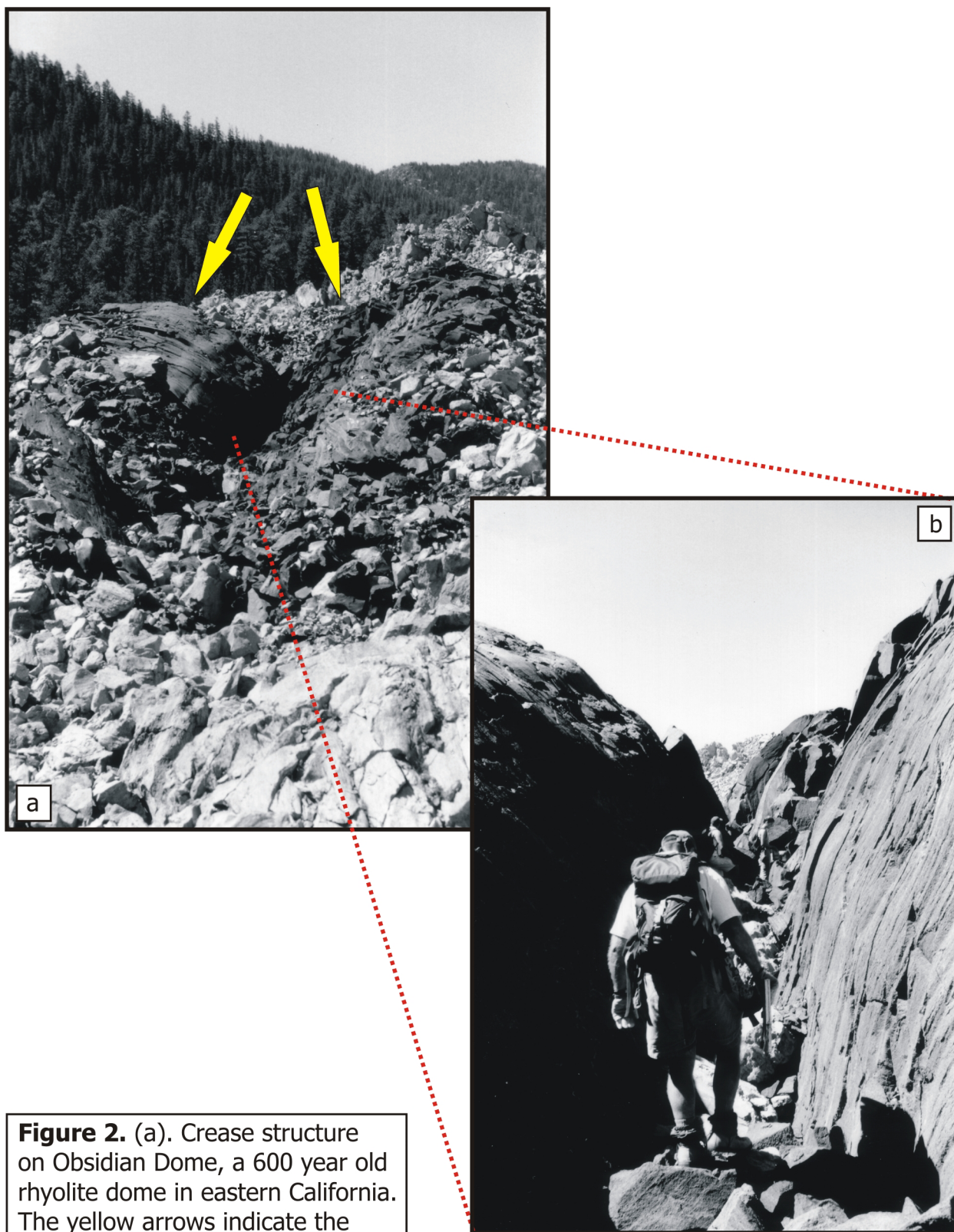


-  = Obsidian
-  = Anhydrous phenocrysts of quartz and feldspar
-  = Coarsely vesiculated pumice
-  = Breccia
-  = Finely vesiculated pumice



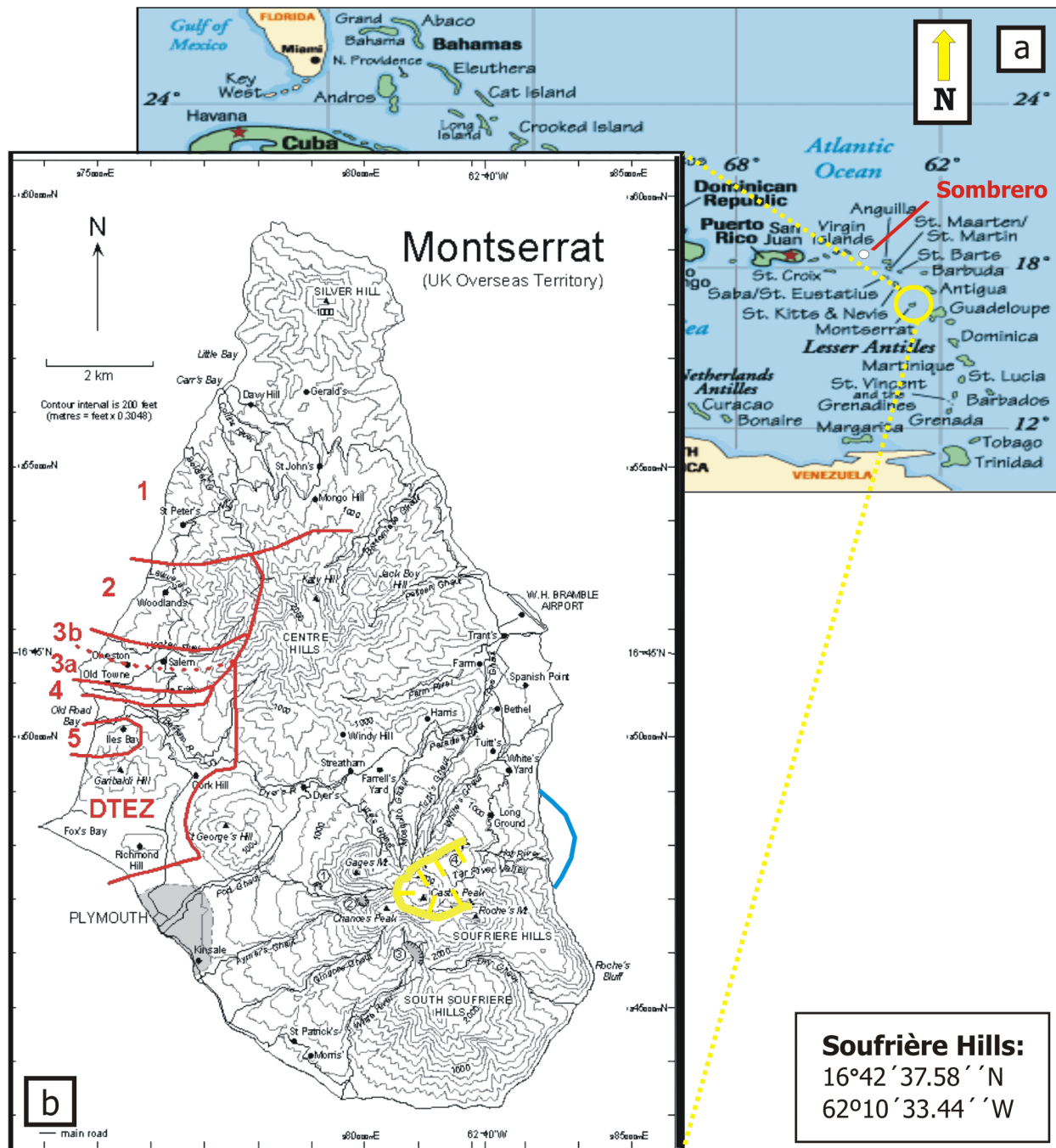
Map view.

**Figure 1.** (a) Cross-sectional view of a rhyolite dome illustrating the sequence of obsidian (glass), phenocrysts, vesiculated pumice, and breccia. (b) Map view of diapir showing "bulls-eye" of finely vesiculated pumice, obsidian, and coarsely vesiculated pumice. (Not to scale.)

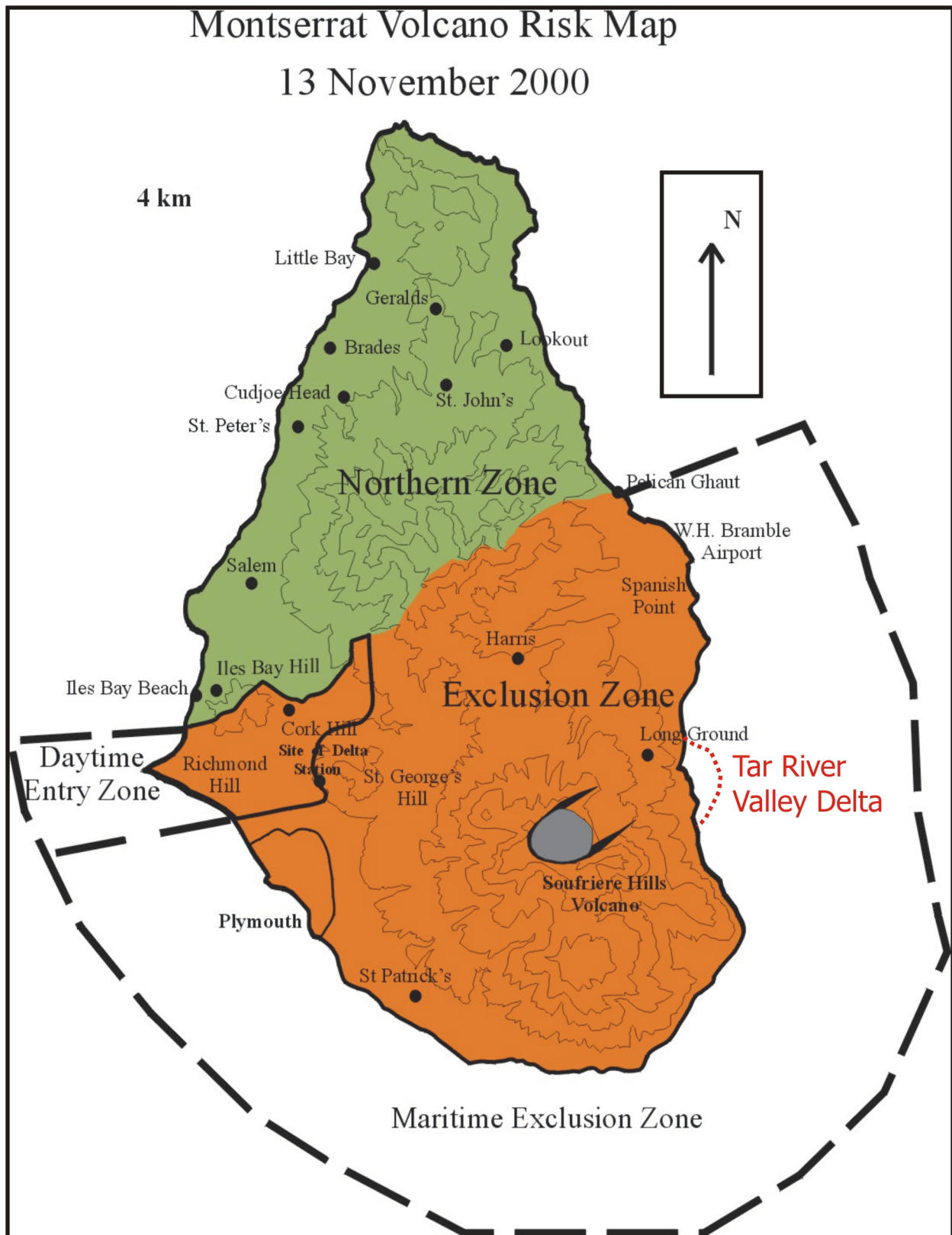


**Figure 2.** (a). Crease structure on Obsidian Dome, a 600 year old rhyolite dome in eastern California. The yellow arrows indicate the paired convex walls exposing the smooth surface underneath. (b) Walking through crease structure.

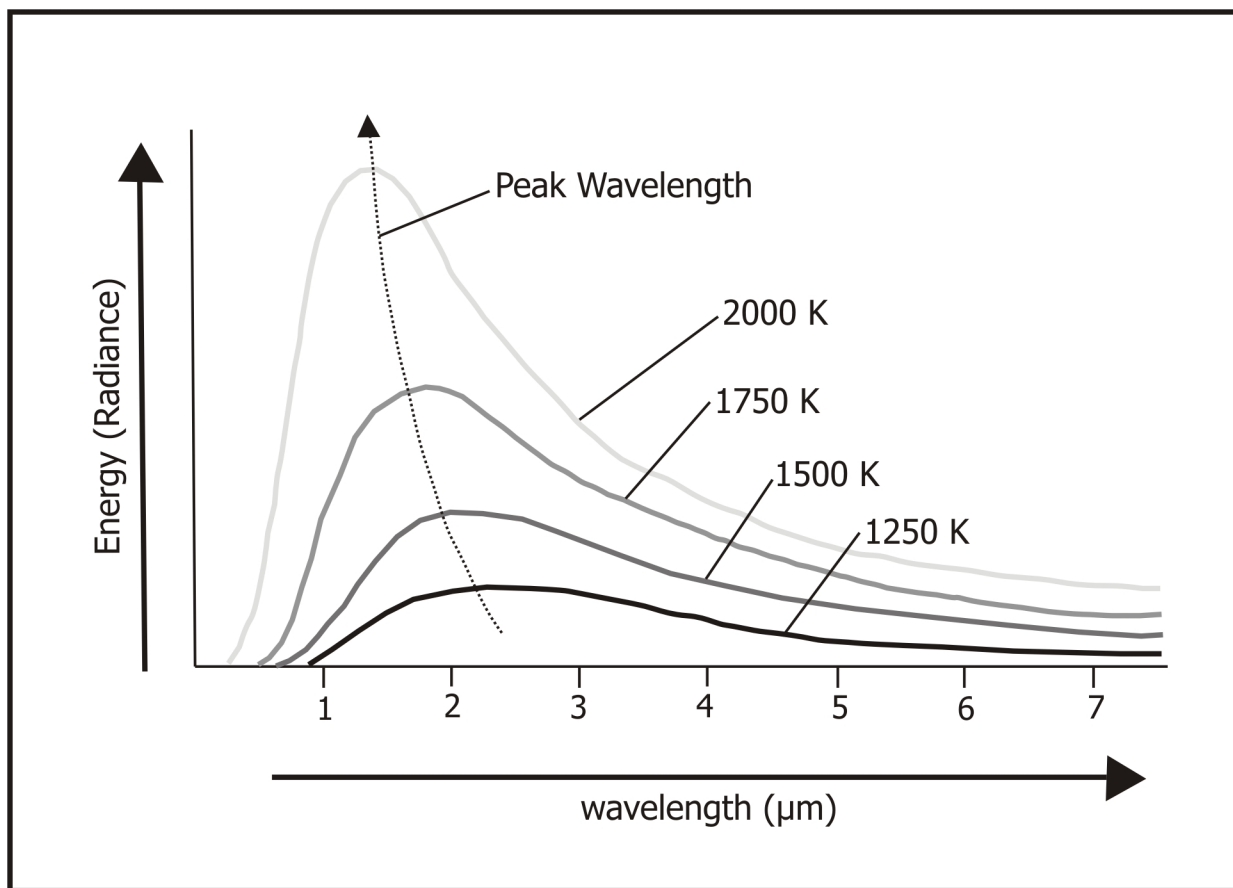




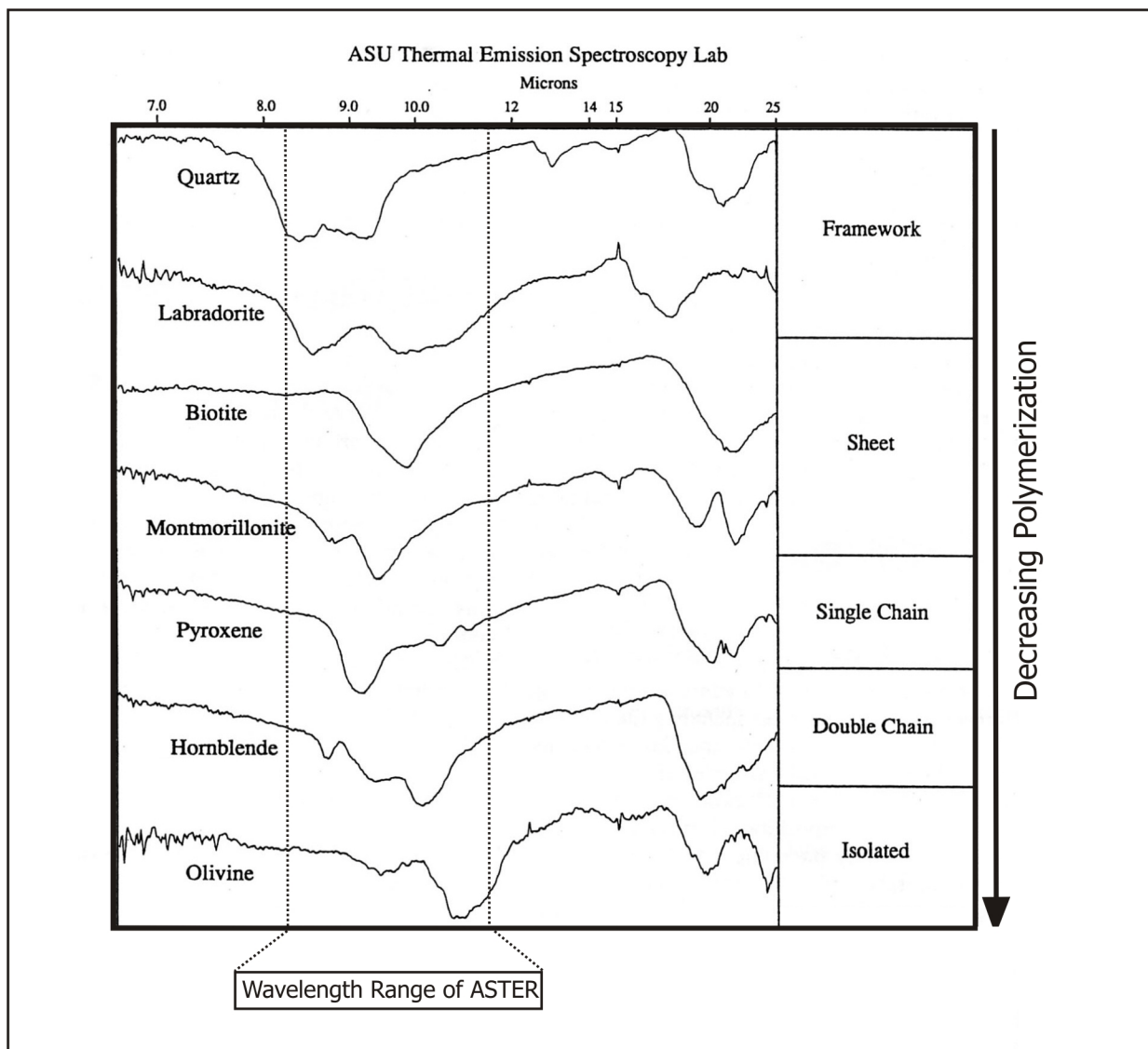
**Figure 3.** Map of Caribbean (www.islandfinder.com, 2003) showing the location of the Lesser Antilles and vicinity (a). The inset (b) is a modified topographical map (1996) of the island of Montserrat used by the MVO for hazard assessment. The restricted zones (shown in red) represent the March 2002 high risk zone status. English's Crater is outlined in yellow. The blue line represents the present day Tar River Valley delta created by numerous pyroclastic flows from 1997 to present. This map was merged with the satellite image data to assist in location of Soufriere Hills.



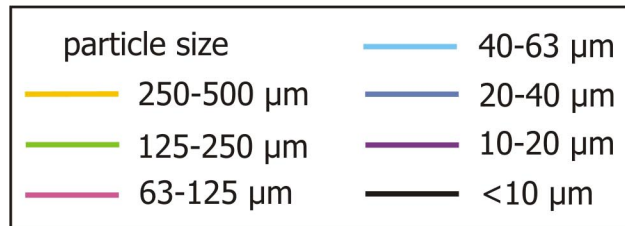
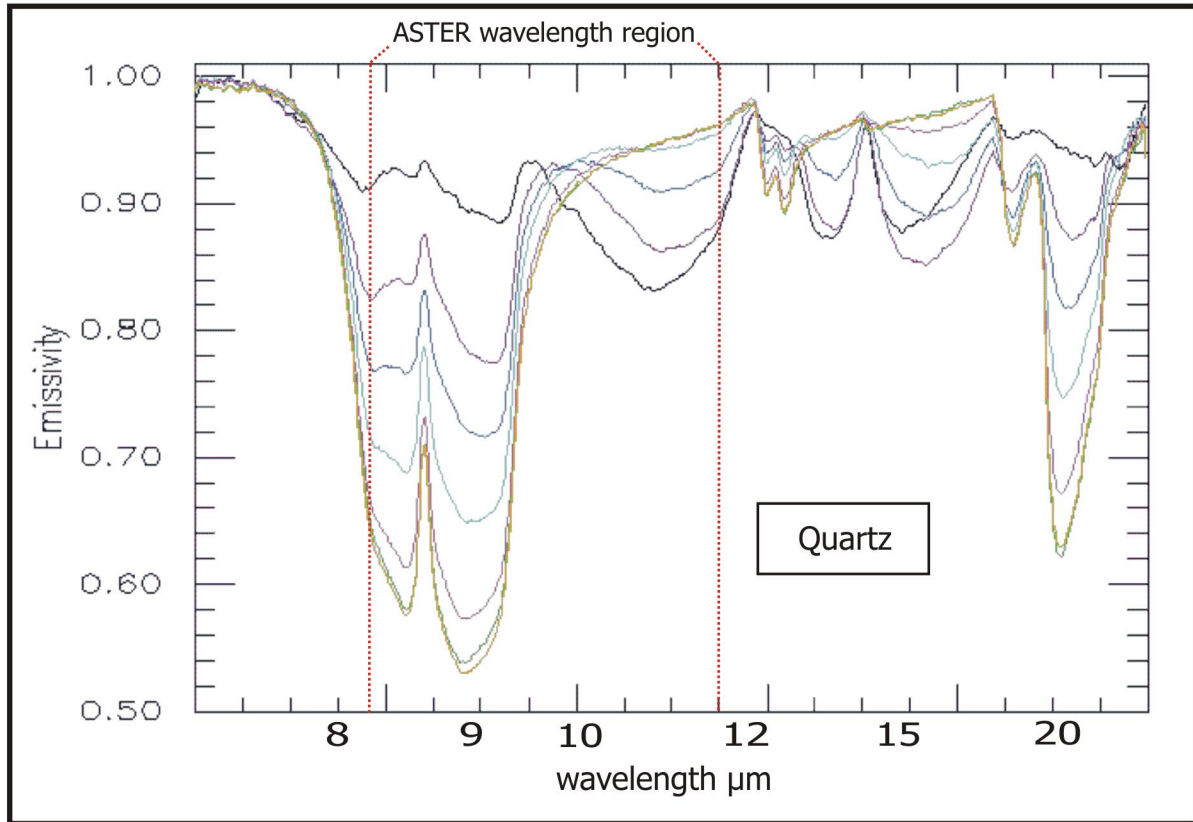
**Figure 4.** Current hazard map of Montserrat from November 2000 ([www.mvo.ms/](http://www.mvo.ms/), 2003).



**Figure 5.** Blackbody radiance curve. Illustration demonstrates the shift in peak radiant energy to shorter wavelengths with an increase in temperature.

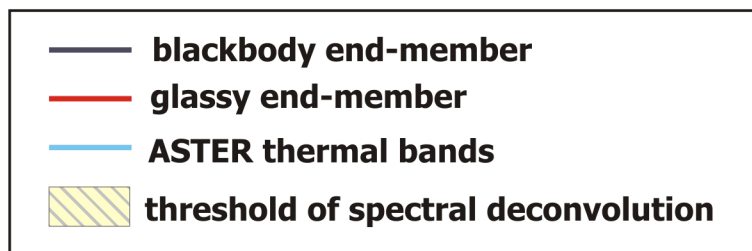
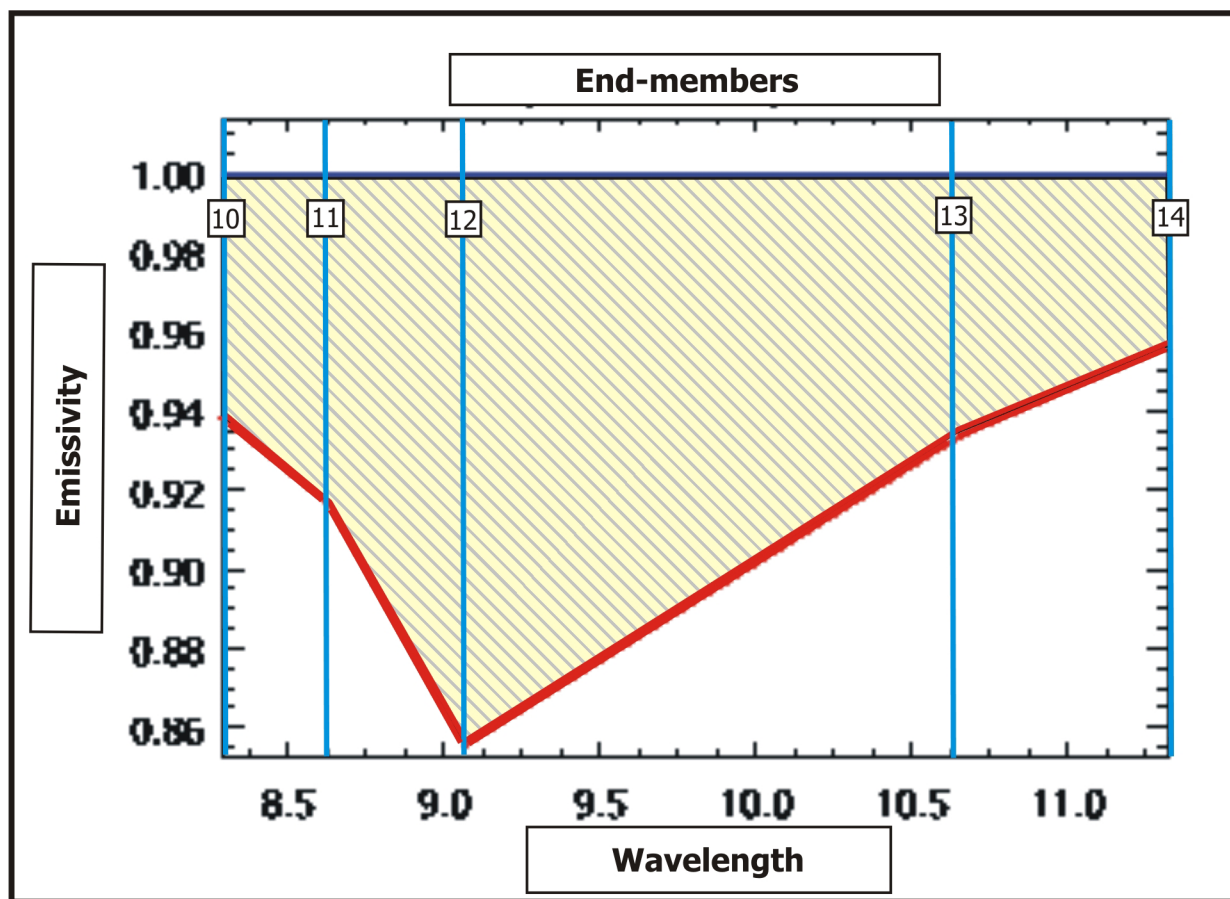


**Figure 6.** Thermal infrared spectra of common rock-forming silicate minerals. This diagram illustrates the shift to longer wavelengths of the primary absorption feature with decreasing polymerization of the silica tetrahedra. (Modified from Christensen et al., 1992).

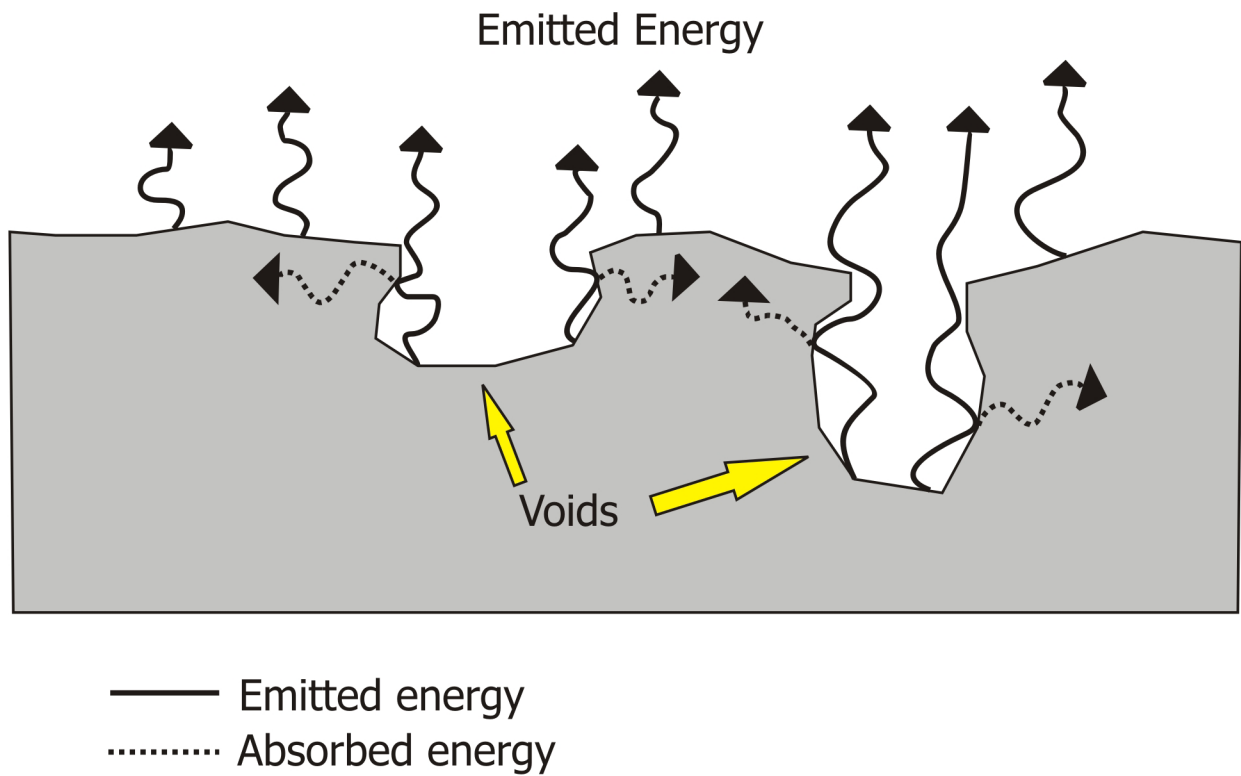


**Figure 7.** Laboratory thermal emission spectra of quartz illustrating the changes in the spectrum as particle size decreases. The ASTER thermal wavelength region is outlined for reference. (Adapted from Ramsey and Christensen, 1998).

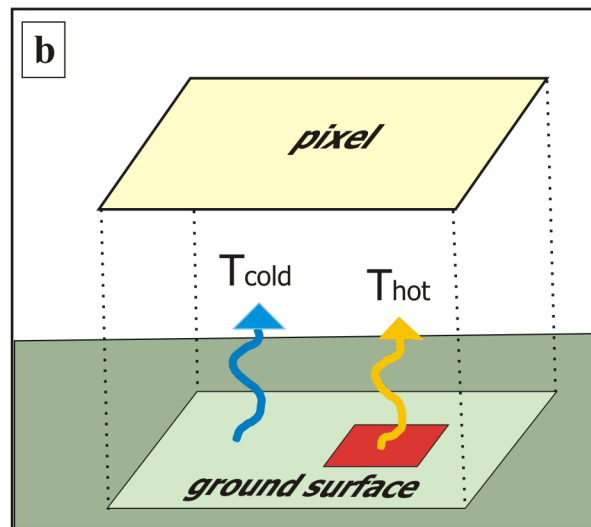
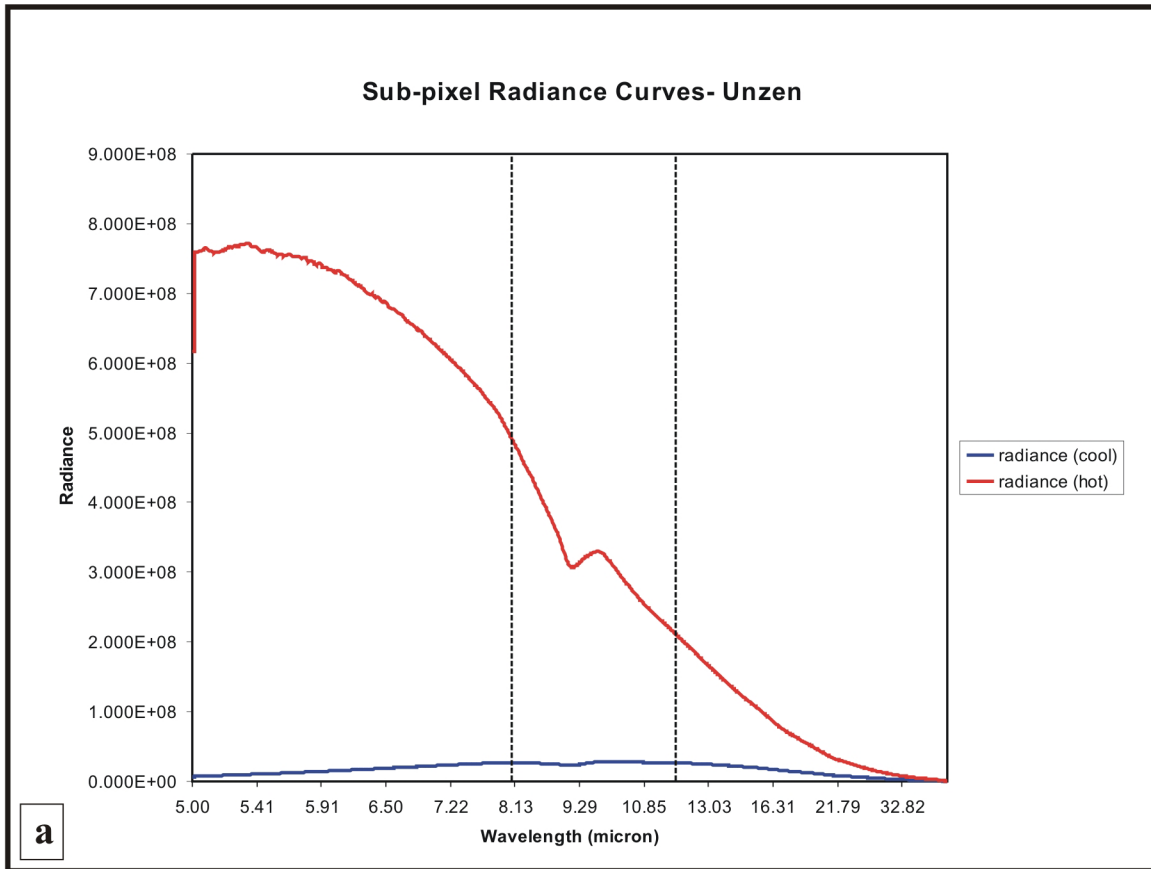




**Figure 8.** Threshold of deconvolution results. Image spectral data should fall within the hatched area on this diagram in order to ideally resolve into the two end-members and total some fraction of 100%. Any image data spectral points falling outside of this threshold, should skew the deconvolution results, cause a higher RMS error, and/or result in aerial percentages to fall below 0 and above 100%. The position of ASTER's TIR bands (10-14) are represented with blue lines.

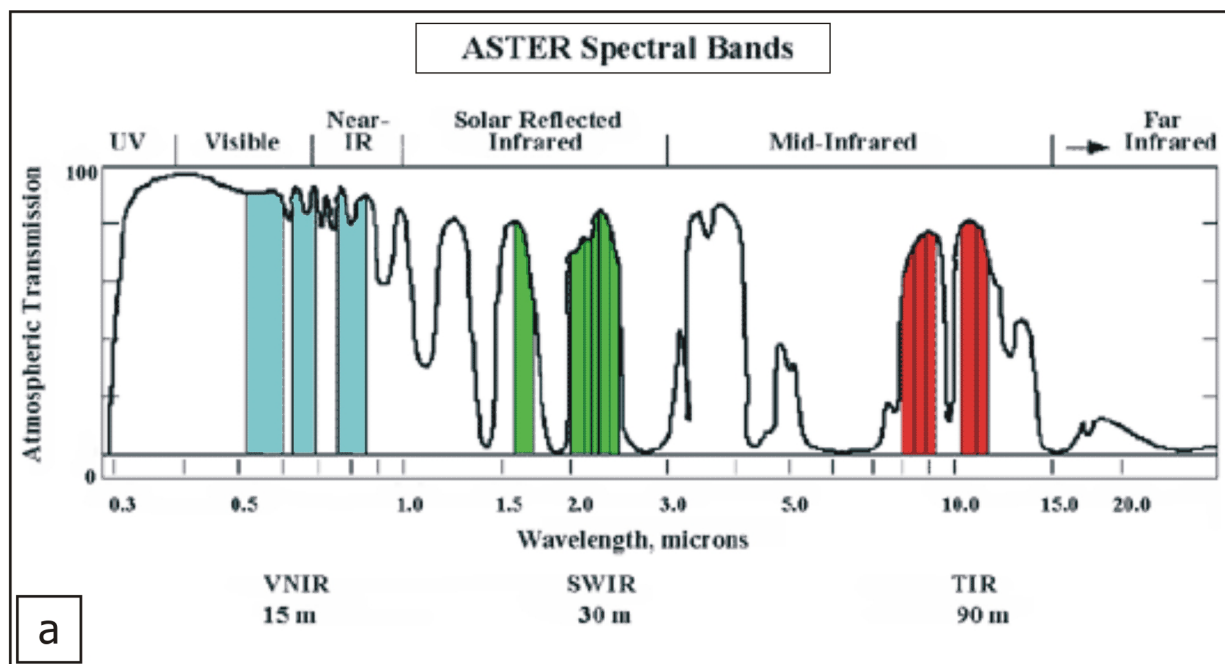


**Figure 9.** Cross-sectional illustration of photons interacting with the surface of void spaces in a vesiculated rock. Upon interaction, a portion of the emitted energy is re-absorbed. This promotes a shallowing of the spectrum that approximates a blackbody.

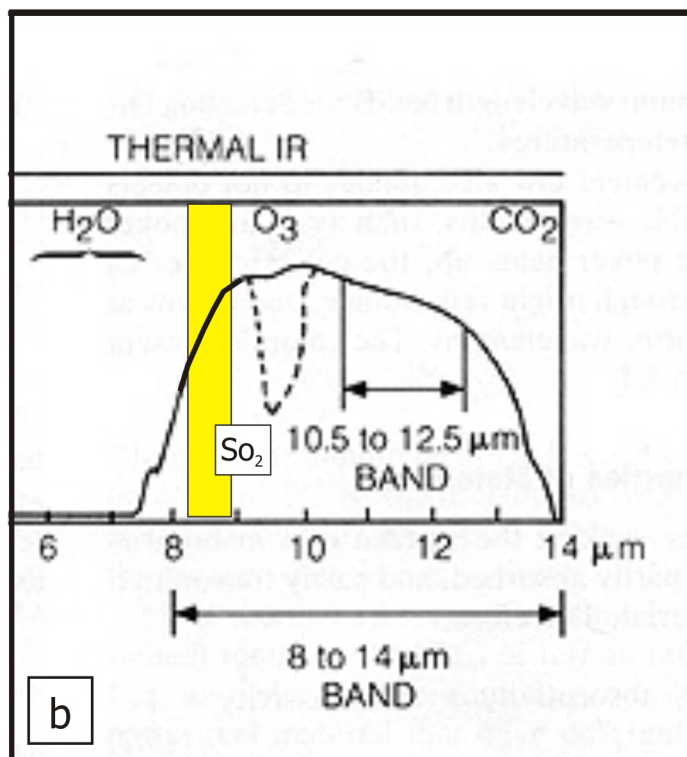


**Figure 10.** Radiance curves (a) derived from two-temperature sub-pixel mixing (b) of a pixel with mixed temperatures. This area (b) is comprised of 90% surface area at 25° and 10% area at 300°C. The 90 meter by 90 meter pixel has one radiance value produced from two very different temperature values. The example graph (a) was created using data compiled from Mt. Unzen (Ramsey, 2003, unpublished data).





**Figure 11.** Atmospheric windows (a) and corresponding wavelength regions and bands covered by the ASTER satellite. The subset (b) centers on the thermal region and illustrates atmospheric absorption regions of water vapor and sulfur dioxide (in yellow). (Modified from Sabins, 2000).



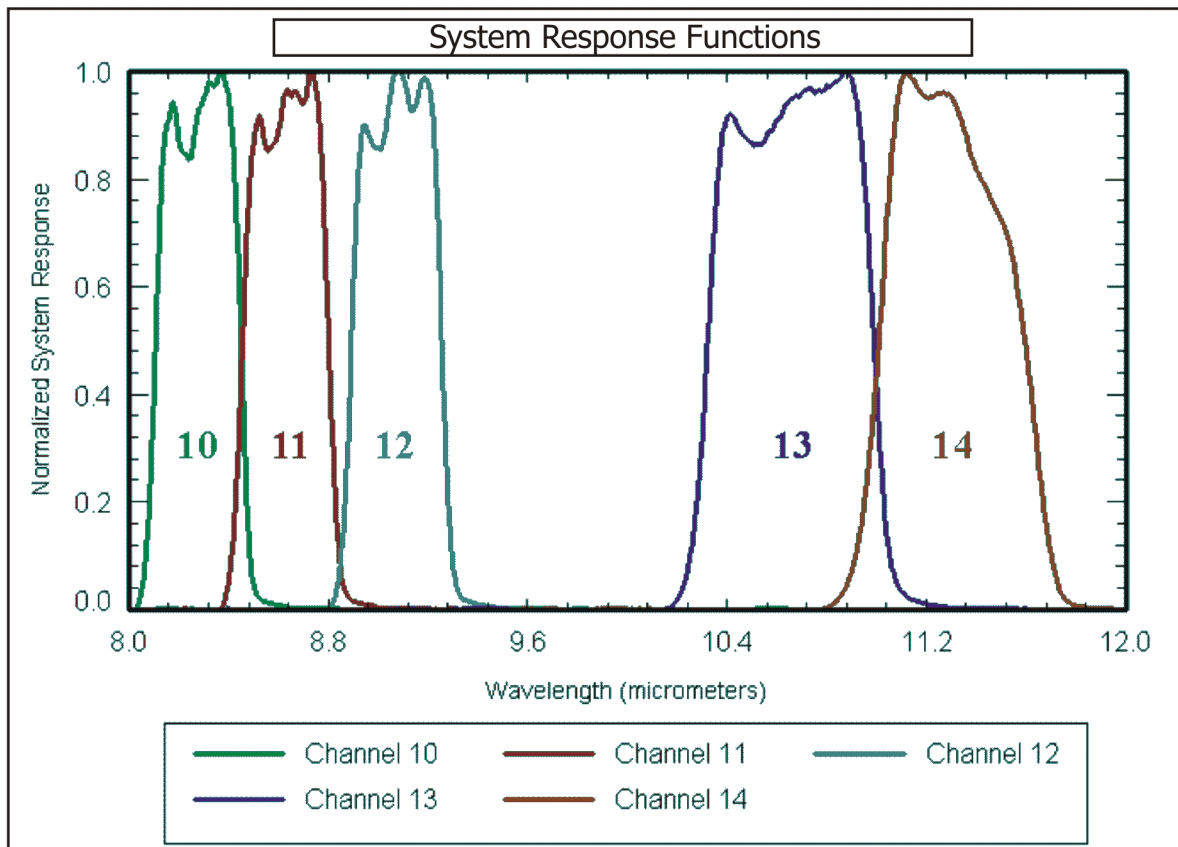


**Figure 12.** ASTER's system response functions for the thermal wavelength region.

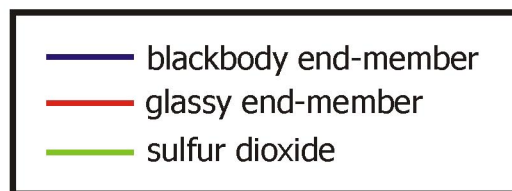
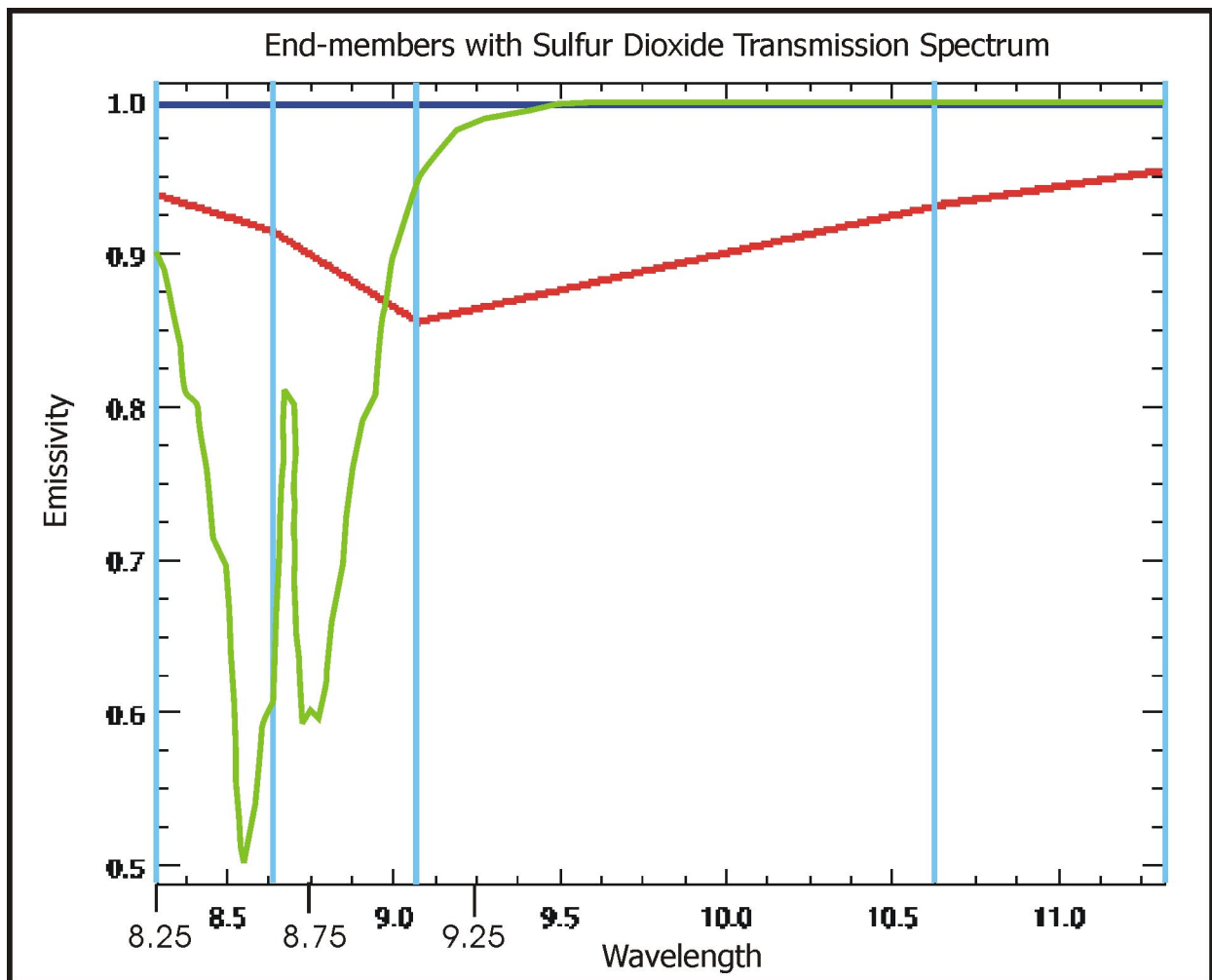
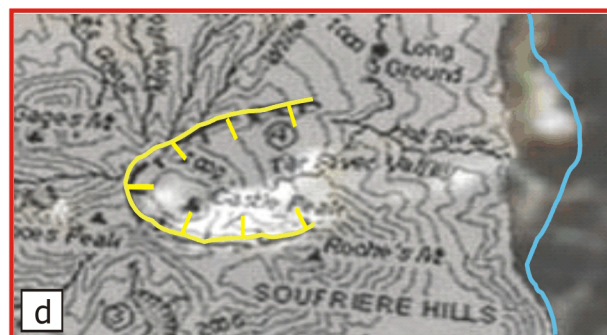
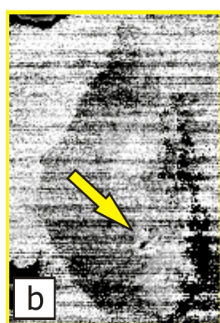
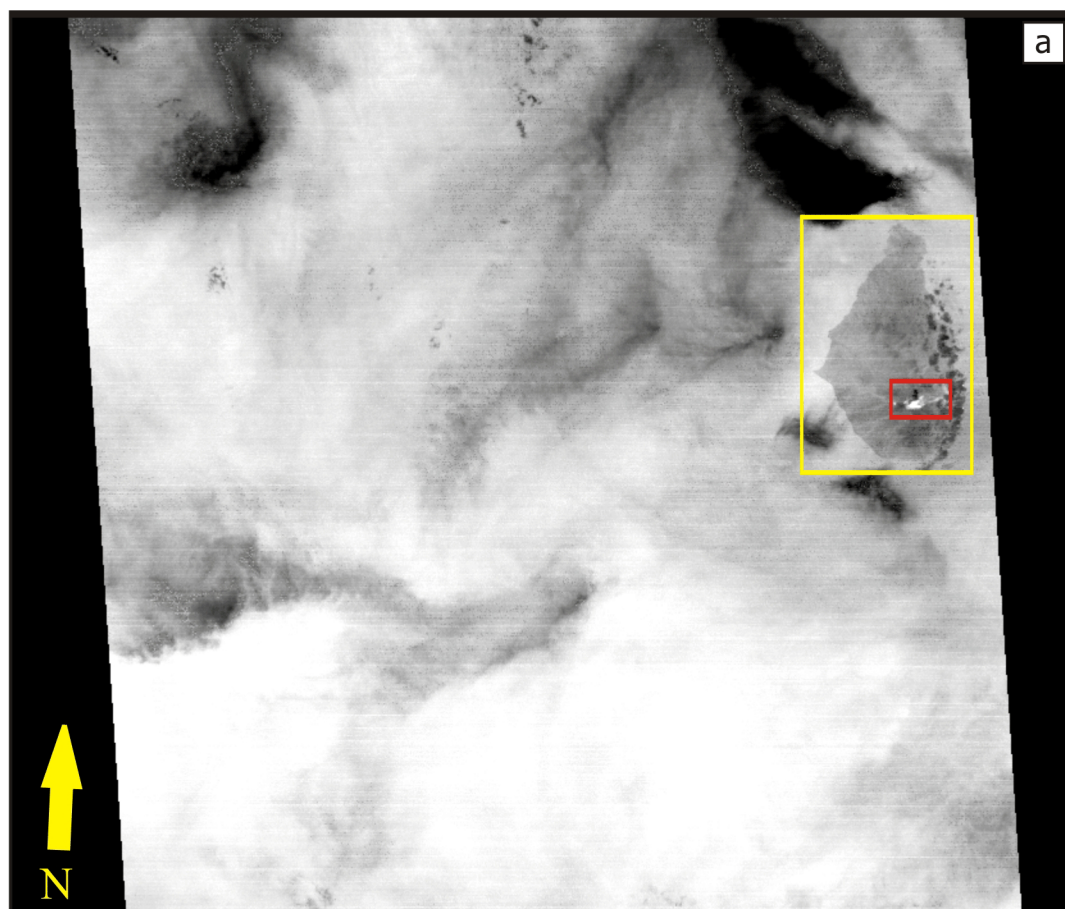


**Figure 13.** End-member spectra with sulfur dioxide spectrum. The blackbody and glassy end-member are degraded to ASTER's five thermal bands. The sulfur dioxide spectrum is multi-spectral data derived from a ratio of transmission through an atmospheric column containing  $10 \text{ g m}^{-2}$  sulfur dioxide to that of a column with no sulfur dioxide (derived from Realmuto and Worden, 2000).



November 1, 2000

**Figure 14.** Full ASTER scene and subsets. (a) The full ASTER Level 2 temperature scene contains the island of Montserrat. Cloud cover (dark) is minimal, except for the east coast, and the thermal anomaly on the dome is distinct. (a, b) Subsets of the emissivity image (b) and the temperature image (c) illustrate the difficulty in locating the position of English's Crater. (d) Subset shows the topographical map merged onto the image data for aid in crater and anomaly location which is outlined in yellow. The new coastline built out by pyroclastic flows is shown in blue.



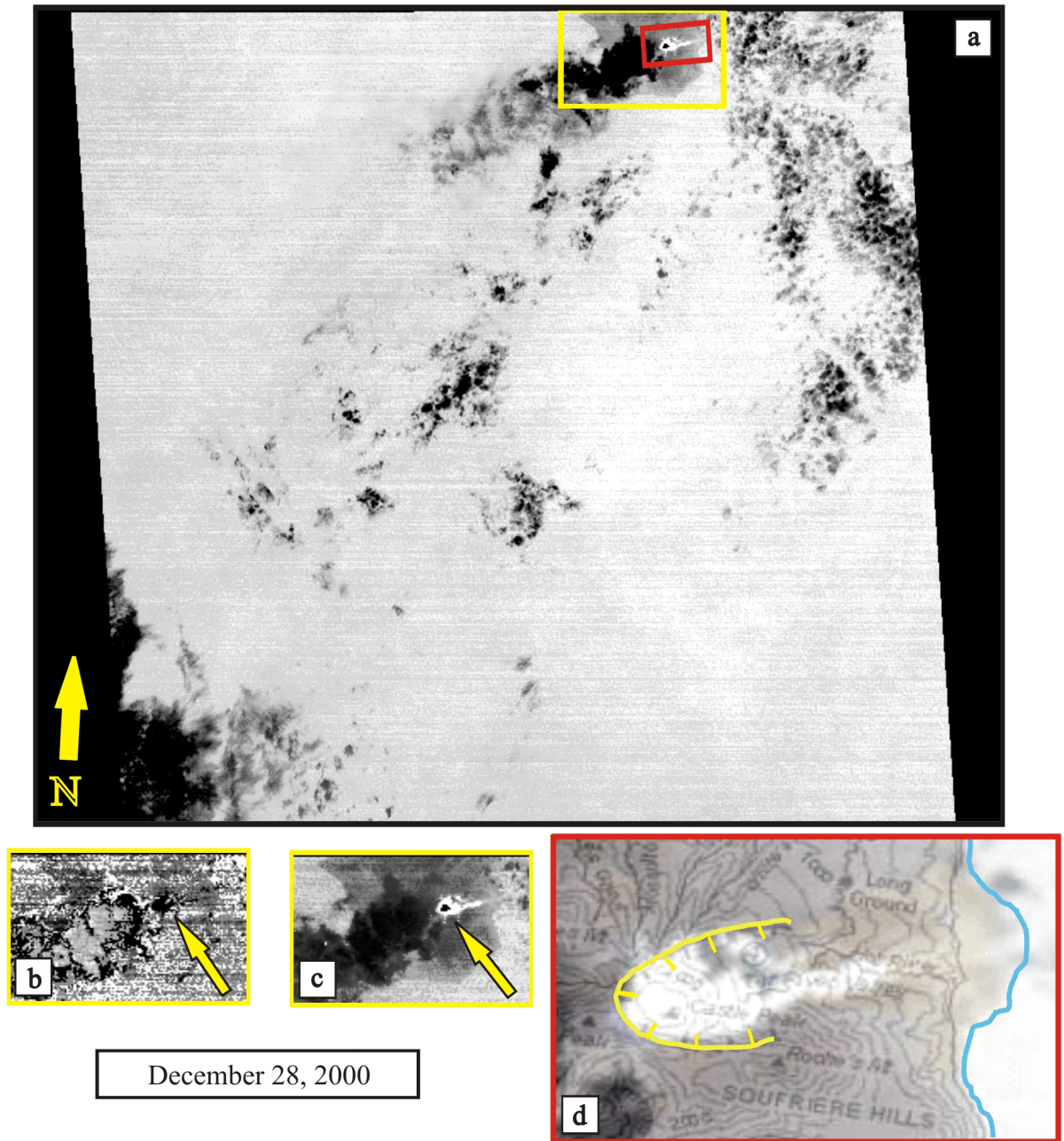


**Figure 15.** Full ASTER scene and subsets. (a) The full ASTER Level 2 temperature scene contains only the southern portion of Montserrat. Cloud cover is minimal and the thermal anomaly on the dome is distinct. A large plume is visible, spreading southwest from the island. (b, c) Subsets of the emissivity image (b) and the temperature image (c) illustrate the difficulty in locating the position of English's Crater. (d) Subset shows the topographical map merged onto the image data for aid in crater and anomaly location which is outlined in yellow. The new coastline built out by pyroclastic flows is shown in blue.

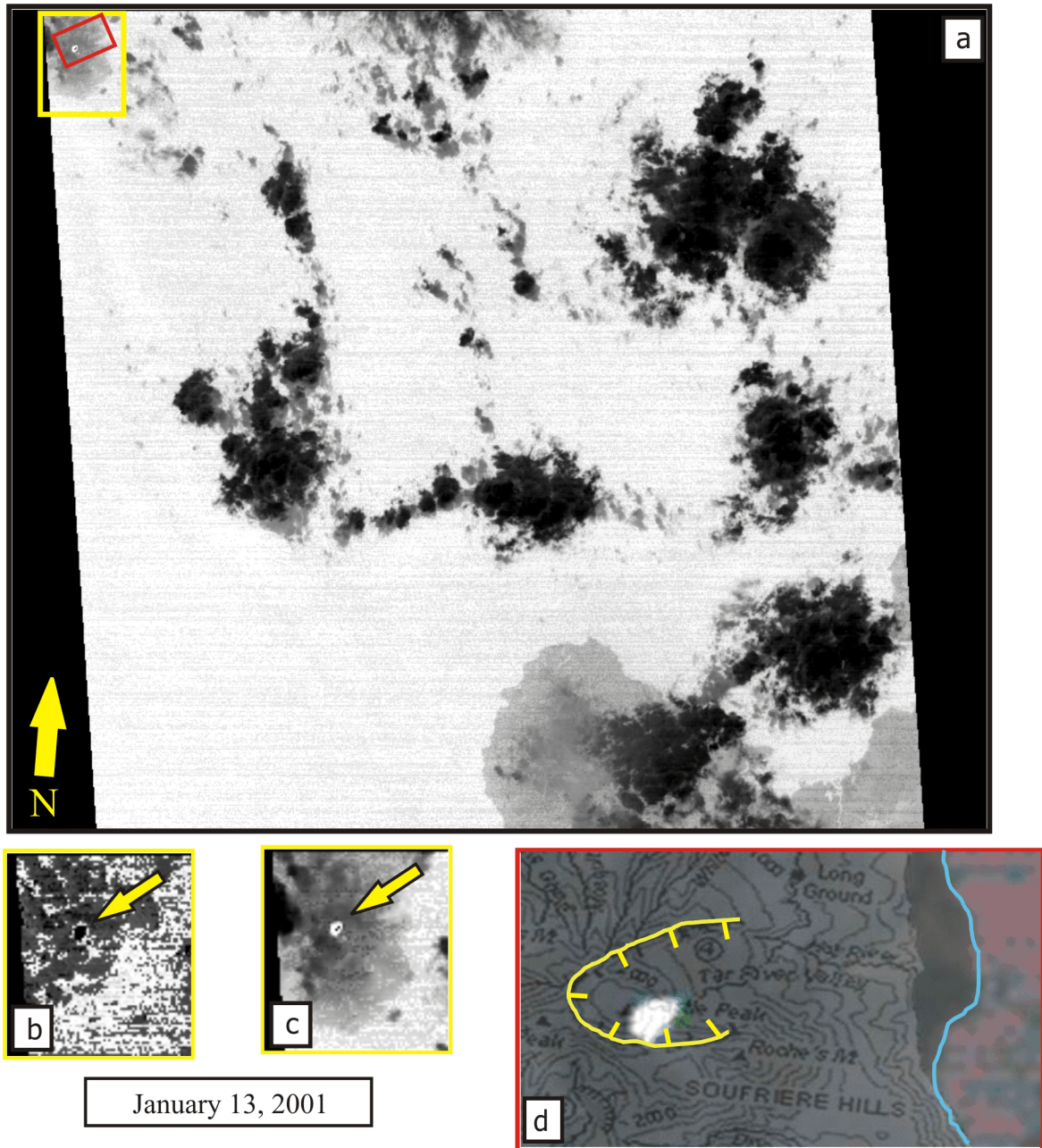


**Figure 16.** Full ASTER scene and subsets. (a) The full ASTER Level 2 temperature scene contains only the southeast portion of Montserrat. Cloud cover is minimal and the thermal anomaly on the dome is distinct. (b, c) Subsets of the emissivity image (b) and the temperature image (c) illustrate the difficulty in locating the position of English's Crater. (d) Subset shows the topographical map merged onto the image data for aid in crater and anomaly location which is outlined in yellow. The new coastline built out by pyroclastic flows is shown in blue.



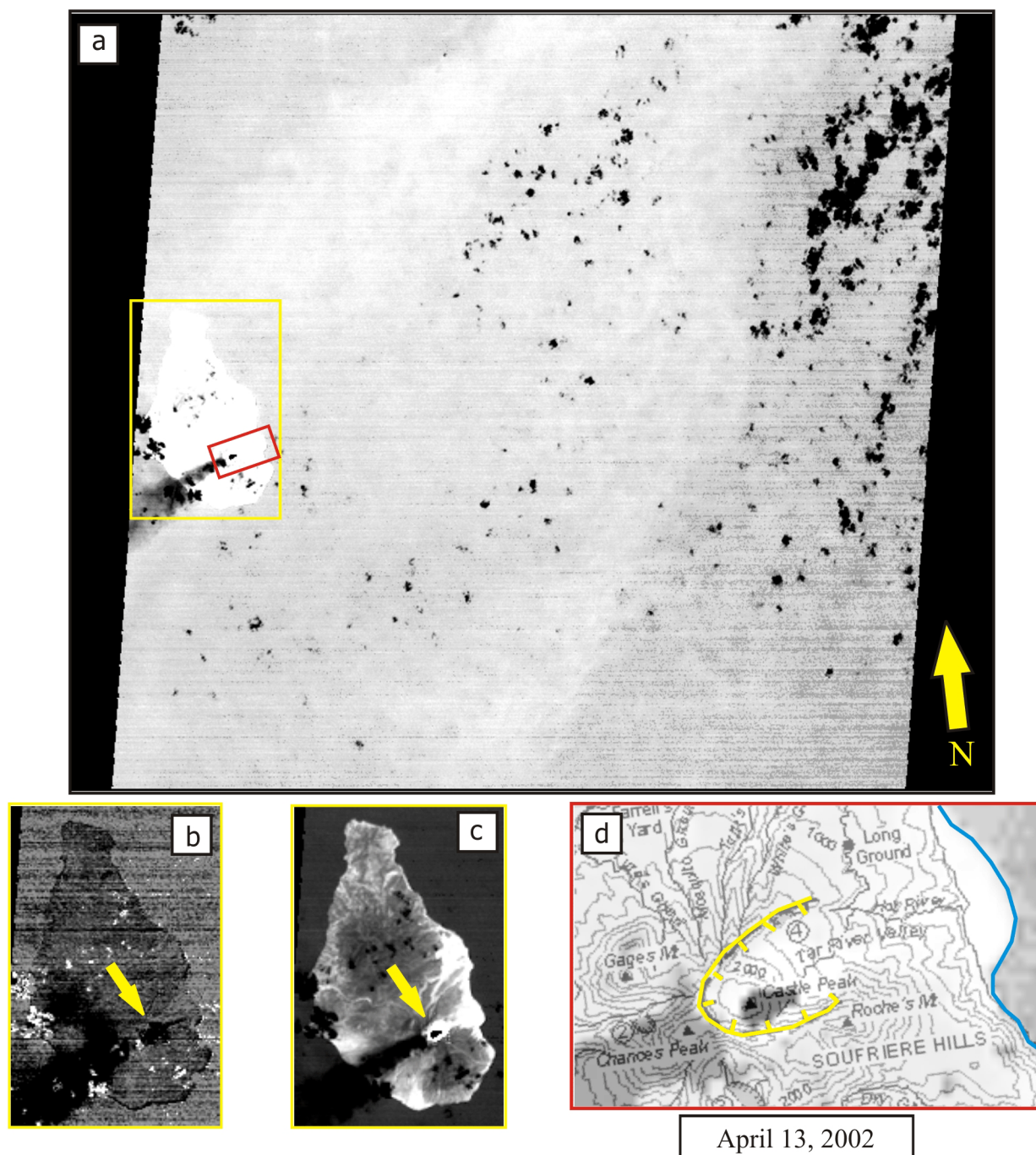


**Figure 17.** Full ASTER scene and subsets. (a) The full ASTER Level 2 temperature scene contains the full island of Montserrat. Cloud cover is minimal and the thermal anomaly on the dome is distinct. A large plume is visible, spreading southwest from the island. (b, c) Subsets of the emissivity image (b) and the temperature image (c) illustrate the difficulty in locating the position of English's Crater. (d) Subset shows the topographical map merged onto the image data for aid in crater and anomaly location which is outlined in yellow. The new coastline built out by pyroclastic flows is shown in blue.

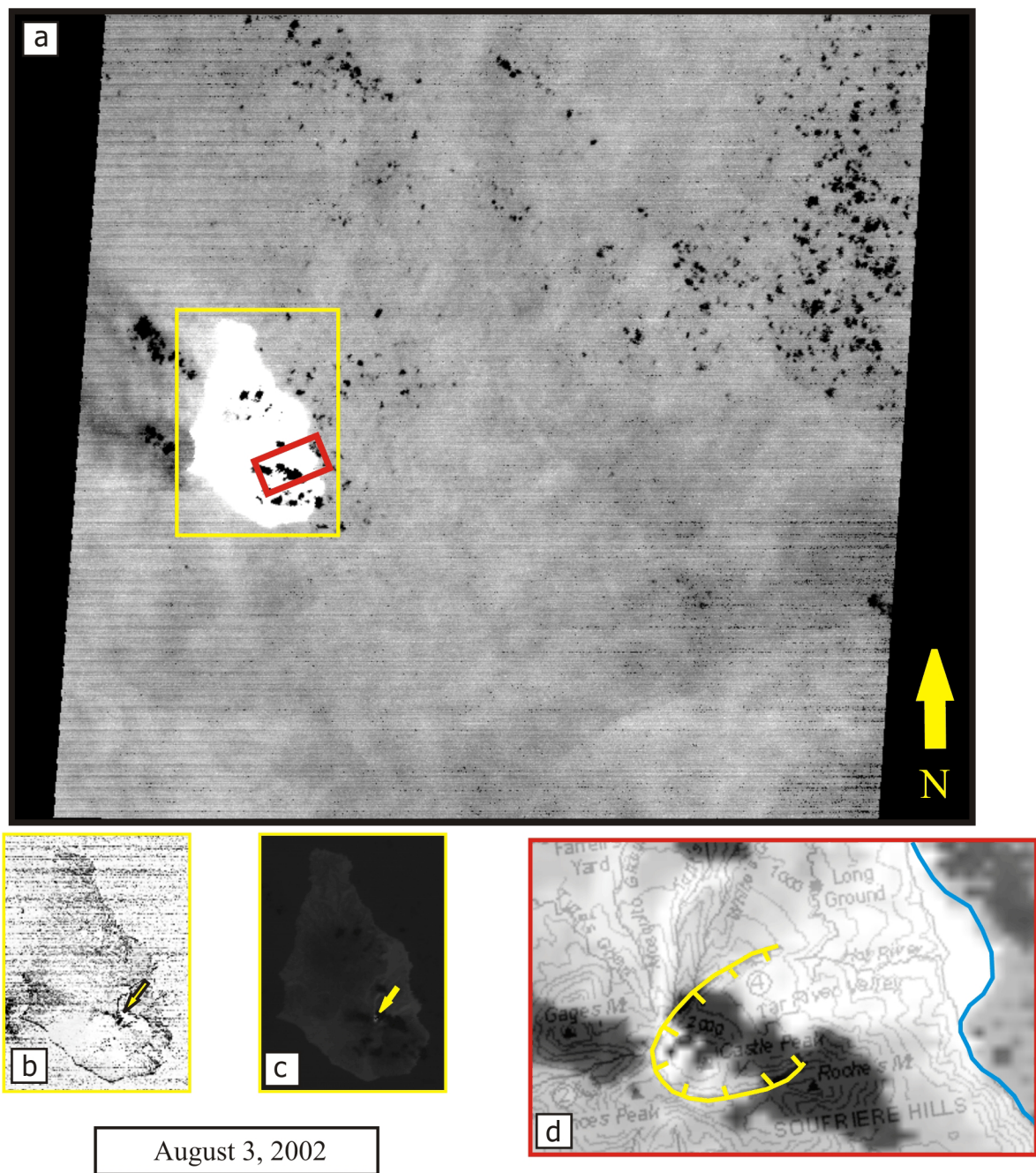


**Figure 18.** Full ASTER scene and subsets. (a) The full ASTER Level 2 temperature scene contains the full island of Montserrat. Cloud cover is minimal, except for a small area directly over the dome (d), and the thermal anomaly is minimal. (b, c) Subsets of the emissivity image (b) and the temperature image (c) illustrate the difficulty in locating the position of English's Crater. (d) Subset shows the topographical map merged onto the image data for aid in crater and anomaly location which is outlined in yellow. The new coastline built out by pyroclastic flows is shown in blue.



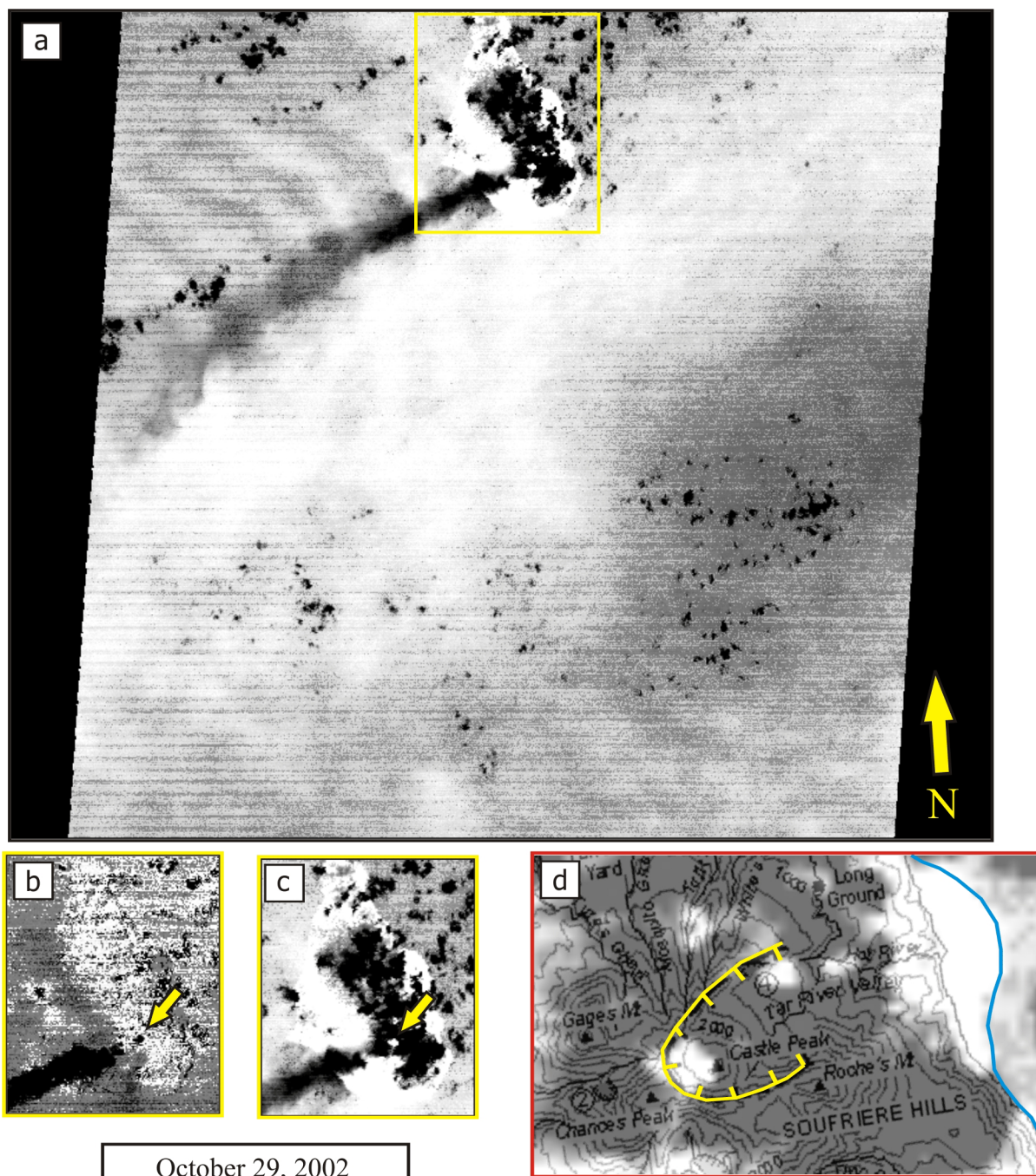


**Figure 19.** Full ASTER scene and subsets. (a) The full ASTER Level 2 temperature scene contains the full island of Montserrat. Cloud cover is extensive, except for a small area directly over the dome (d), and the thermal anomaly is minimal. (b, c) Subsets of the emissivity image (b) and the temperature image (c) illustrate the difficulty in locating the position of English's Crater. (d) Subset shows the topographical map merged onto the image data for aid in crater and anomaly location which is outlined in yellow. The new coastline built out by pyroclastic flows is shown in blue.

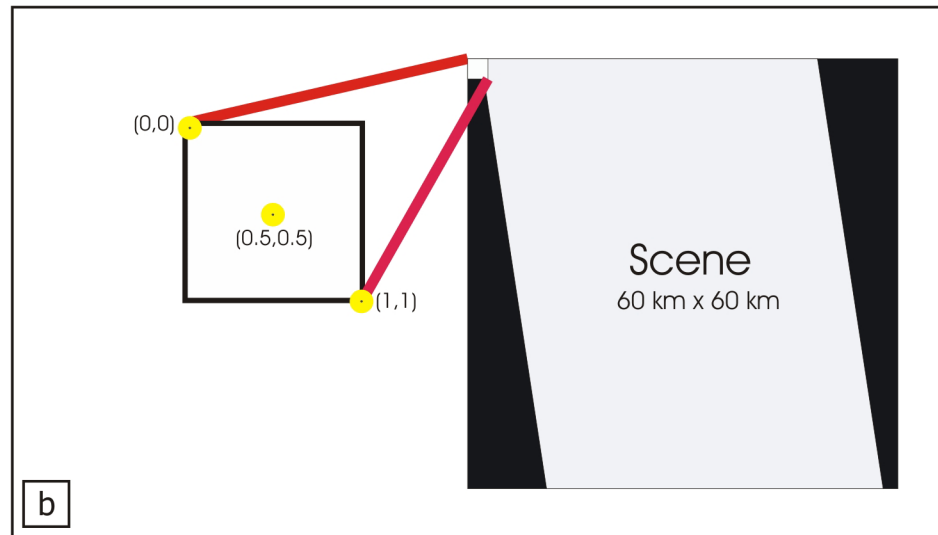
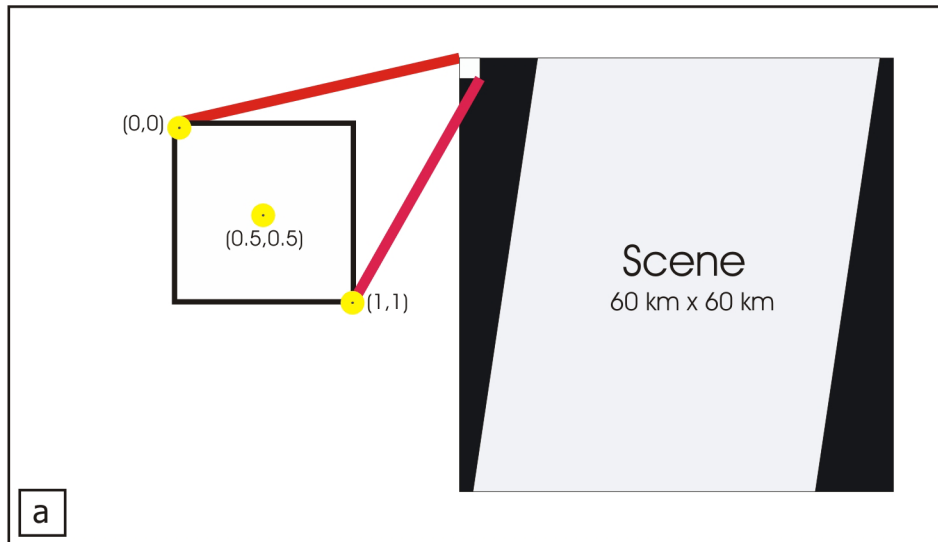


**Figure 20.** Image processing. (a, b) To establish accurate scene coordinates, the upper left pixel X and Y values were entered as 0.5, 0.5 for the descending scene (a) and the ascending scene (b).

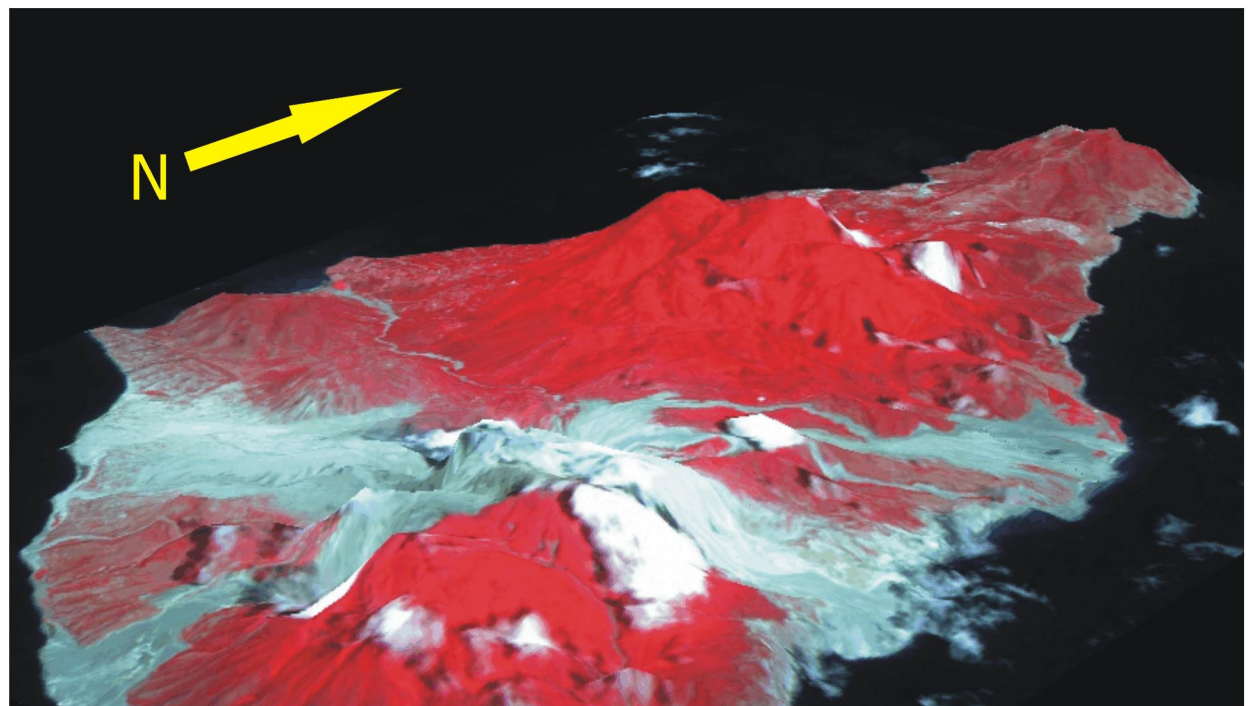
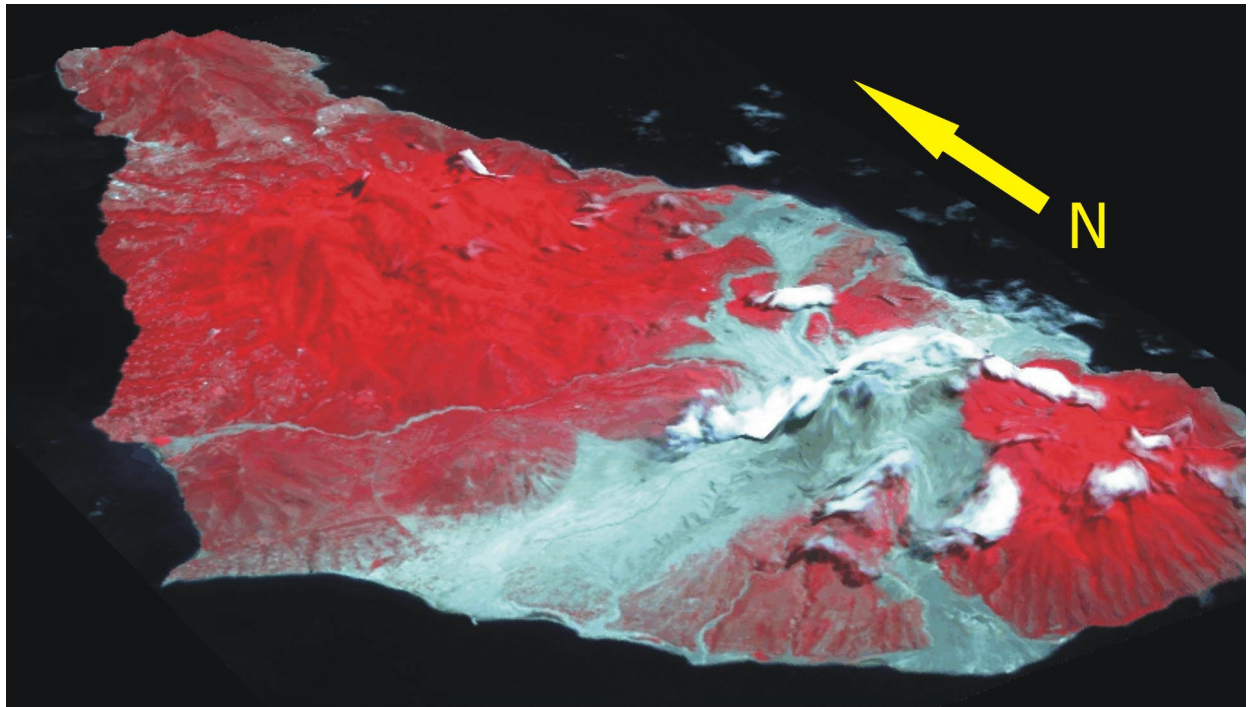


**Figure 21.** Experimentally derived ASTER Digital Elevation Model (DEM) of Montserrat draped with a visible near infrared image. The August 2002 image is loaded with Band 1 in blue, Band 2 in green, and Band 3 in red.



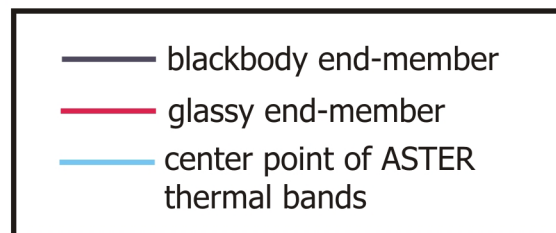
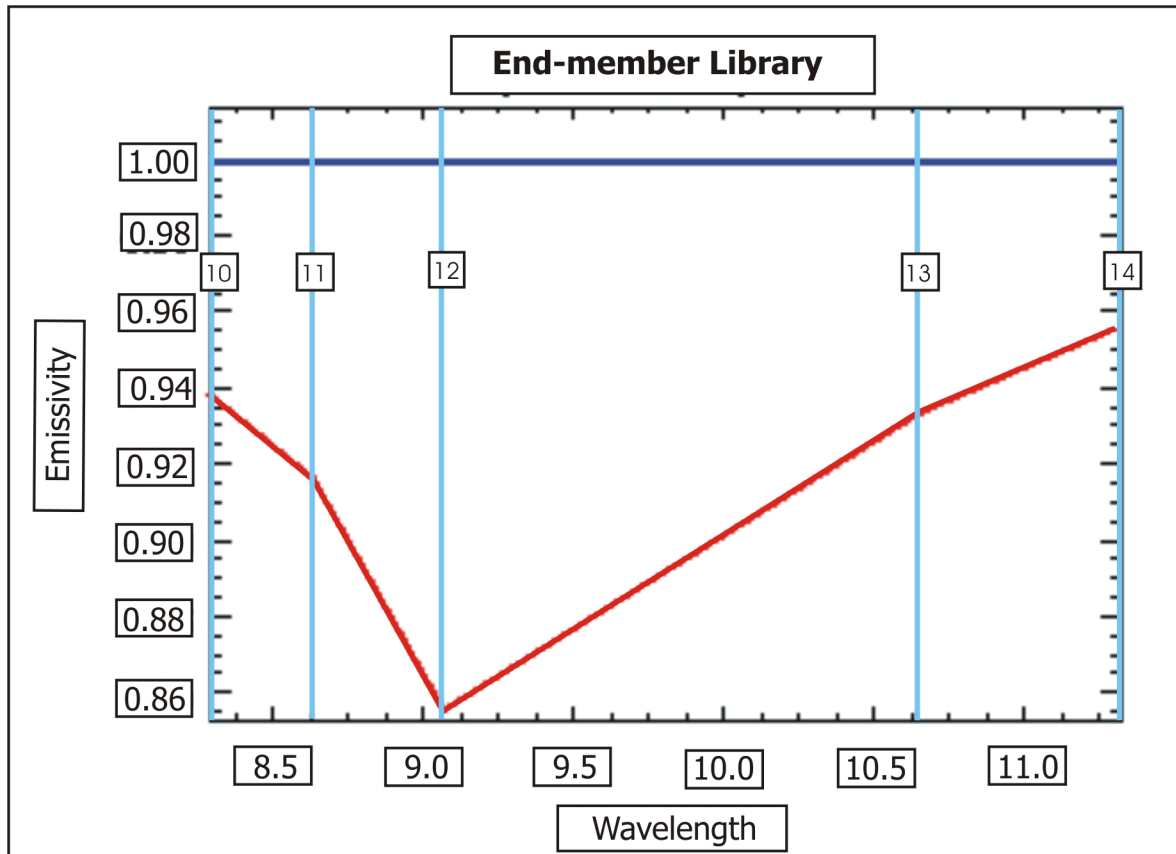


**Figure 22.** The blackbody and glassy end-member spectra used for spectral deconvolution.

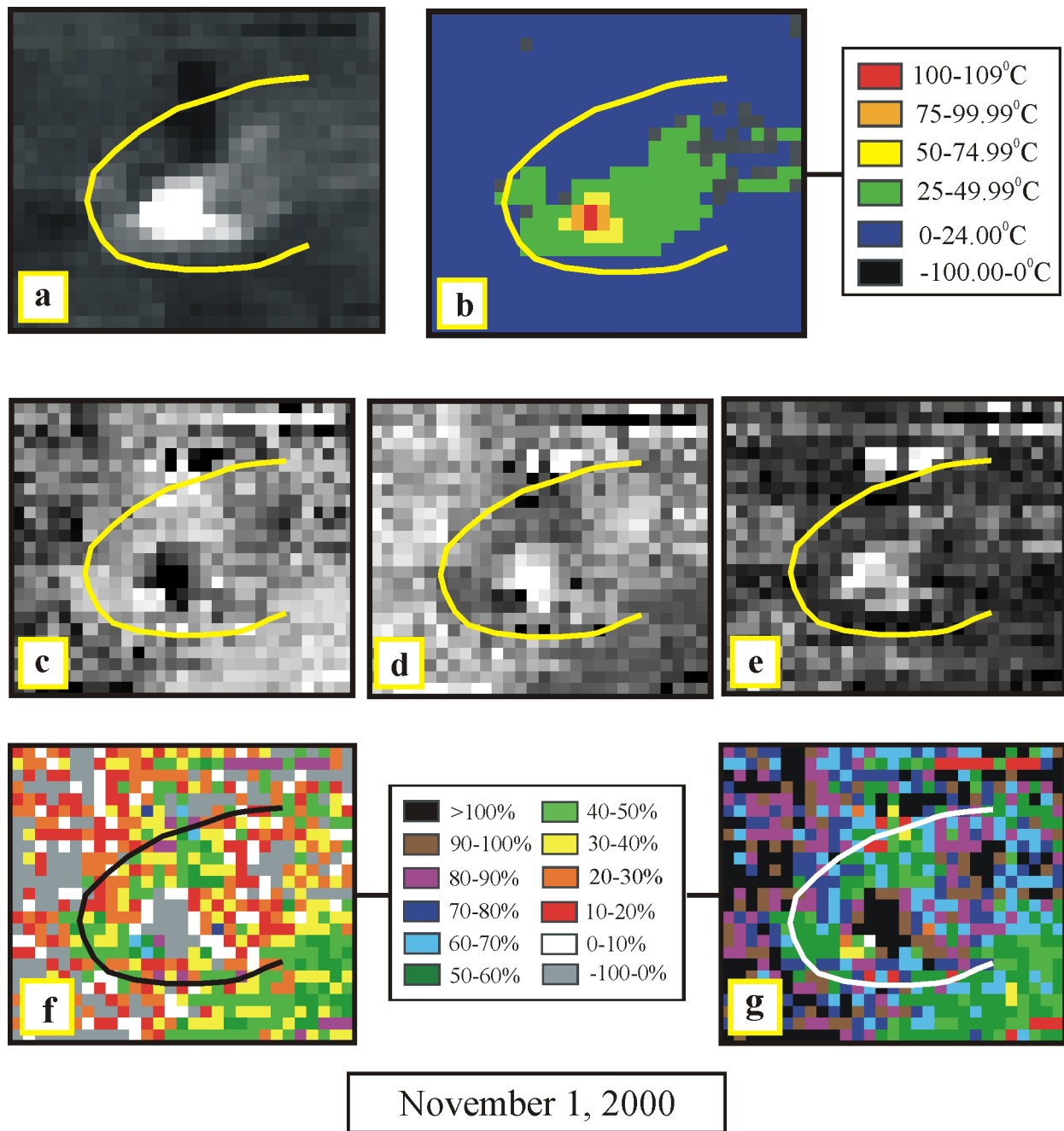


**Figure 23.** The subsets above are cropped to the same geographic area and are 2610m x 2250 m in dimension. The temperature anomaly is easily distinguished (a) and comparatively not hot and spreads to the east in the color map (b). The spectral deconvolution results, blackbody (c) and glass (d) are next to the RMS error results (e). A color map was applied to the blackbody results (f) and to the glass results (g) to illustrate the distribution of each on the dome and vicinity. English's Crater is outlined in yellow to establish the location and size of the thermal anomaly in the temperature and deconvolution results.

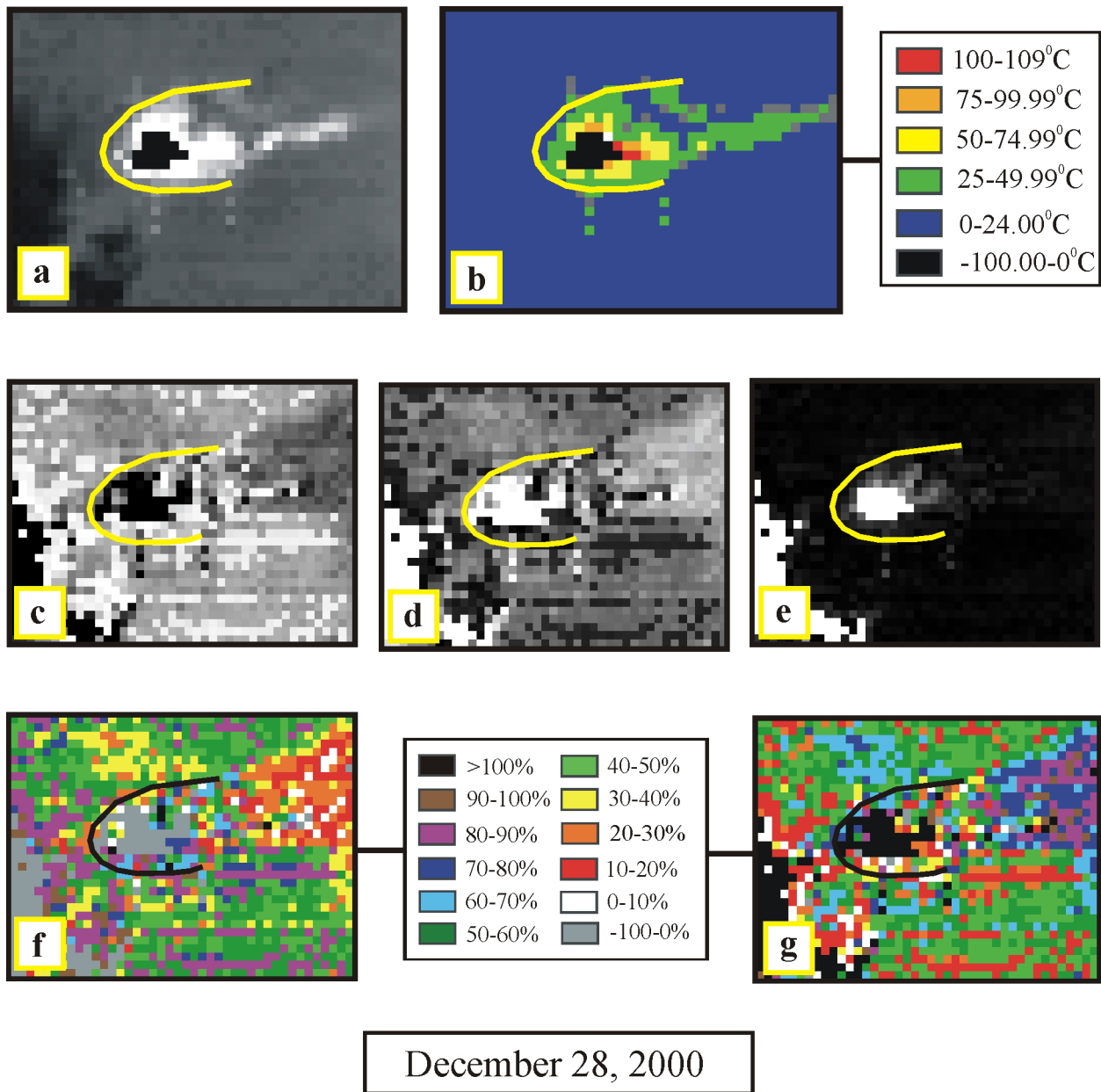


**Figure 24.** The subsets above are cropped to the same geographic area and are 3780m x 2880 m in dimension. The temperature anomaly is easily distinguished (a) and contains a group of saturated pixels (a,b). The spectral deconvolution results, blackbody (c) and glass (d) are next to the RMS error results (e). A color map was applied to the blackbody results (f) and to the glass results (g) to illustrate the distribution of each on the dome and vicinity. English's Crater is outlined in yellow to establish the location and size of the thermal anomaly in the temperature and deconvolution results.

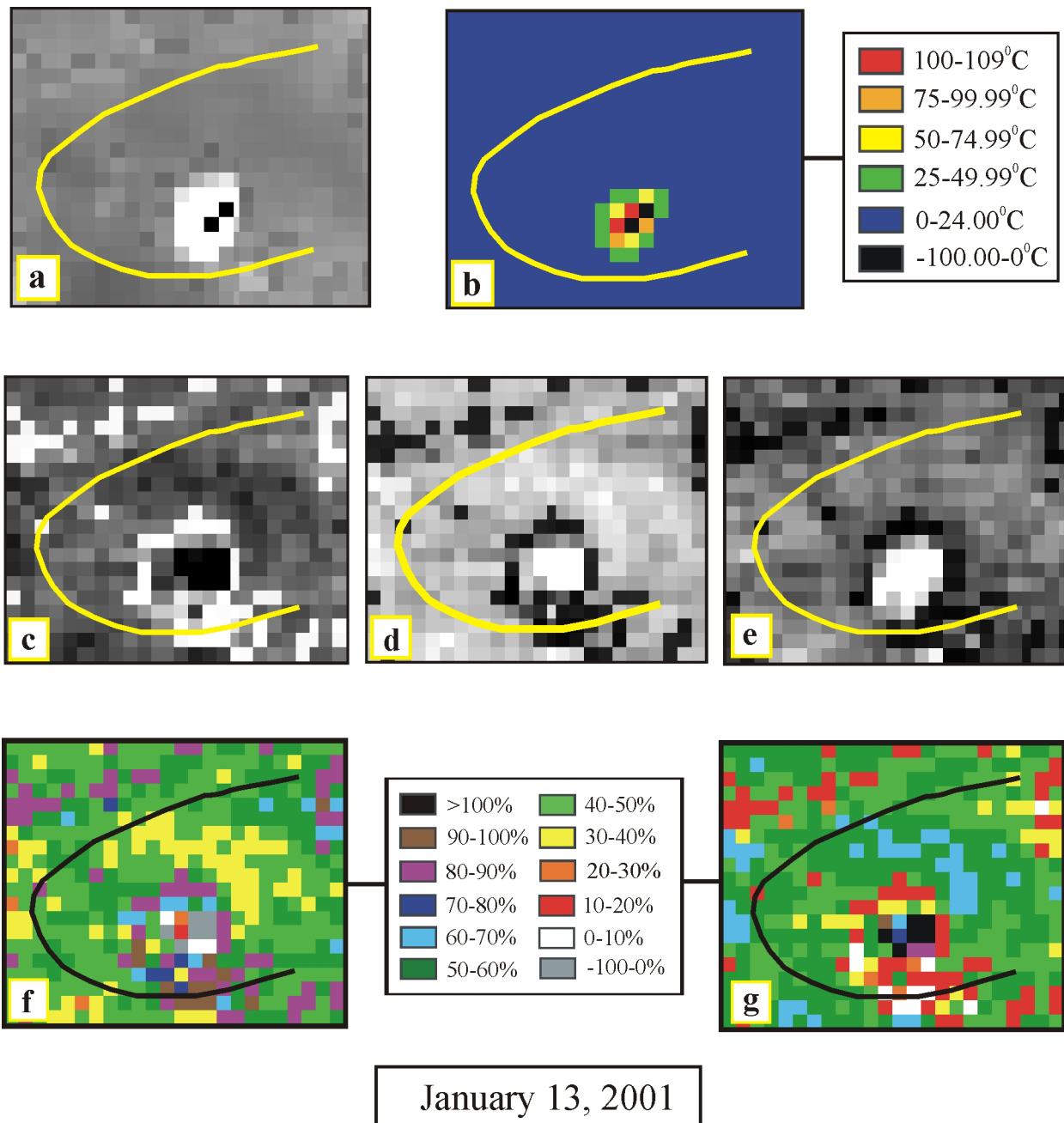


**Figure 25.** The subsets above are cropped to the same geographic area and are 2160m x 1800 m in dimension. The temperature anomaly is easily distinguished (a) and concentrated as seen in the color map (b). The spectral deconvolution results, blackbody (c) and glass (d) are next to the RMS error results (e). A color map was applied to the blackbody results (f) and to the glass results (g) to illustrate the distribution of each on the dome and vicinity. English's Crater is outlined in yellow to establish the location and size of the thermal anomaly in the temperature and deconvolution results.

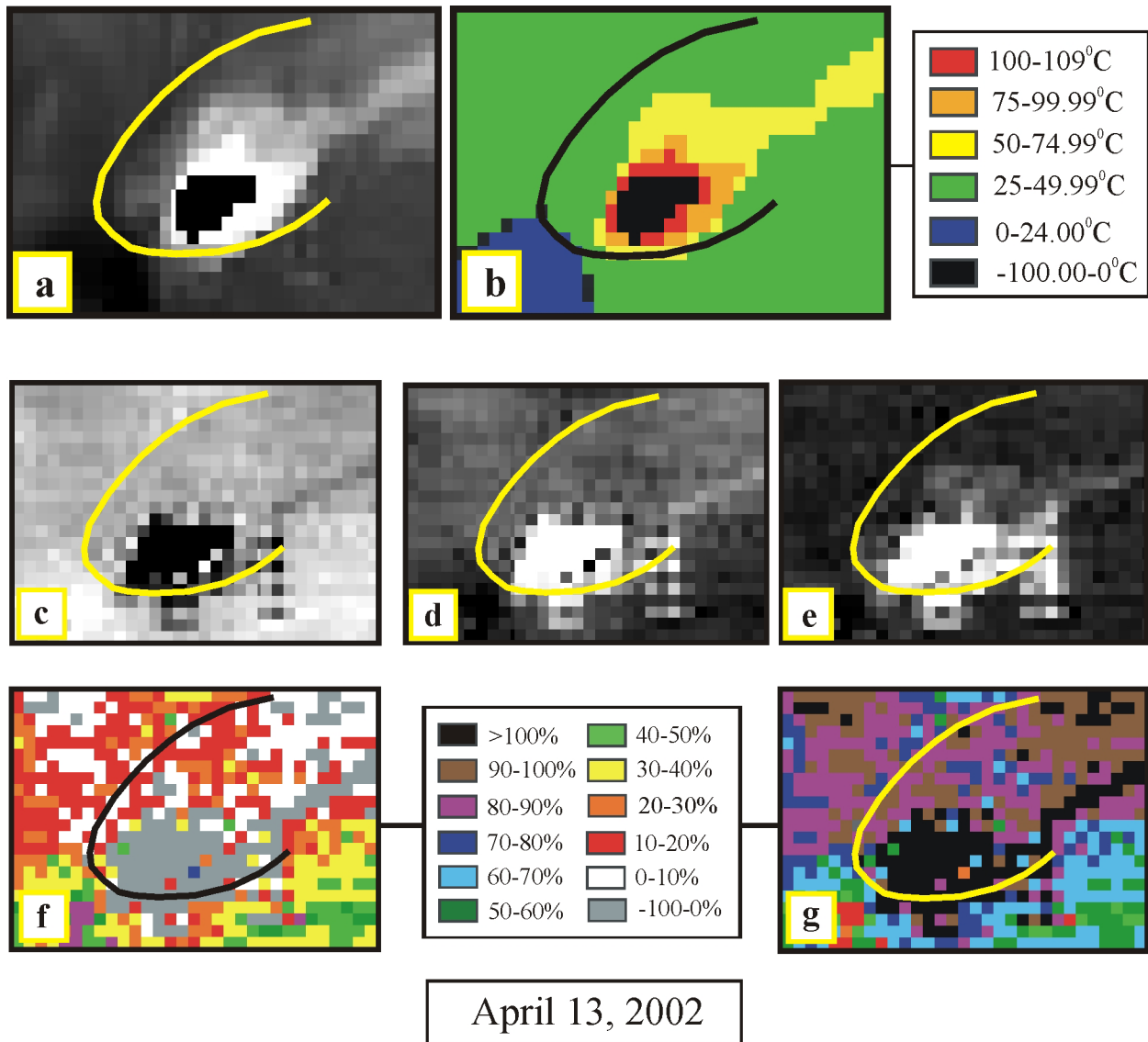


**Figure 26.** The subsets above are cropped to the same geographic area and are 2250m x 1980 m in dimension. The temperature anomaly is easily distinguished (a) and large as seen in the color map (b). Several pixels are saturated (b). The spectral deconvolution results, blackbody (c) and glass (d) are next to the RMS error results (e). A color map was applied to the blackbody results (f) and to the glass results (g) to illustrate the distribution of each on the dome and vicinity. English's Crater is outlined in yellow to establish the location and size of the thermal anomaly in the temperature and deconvolution results.



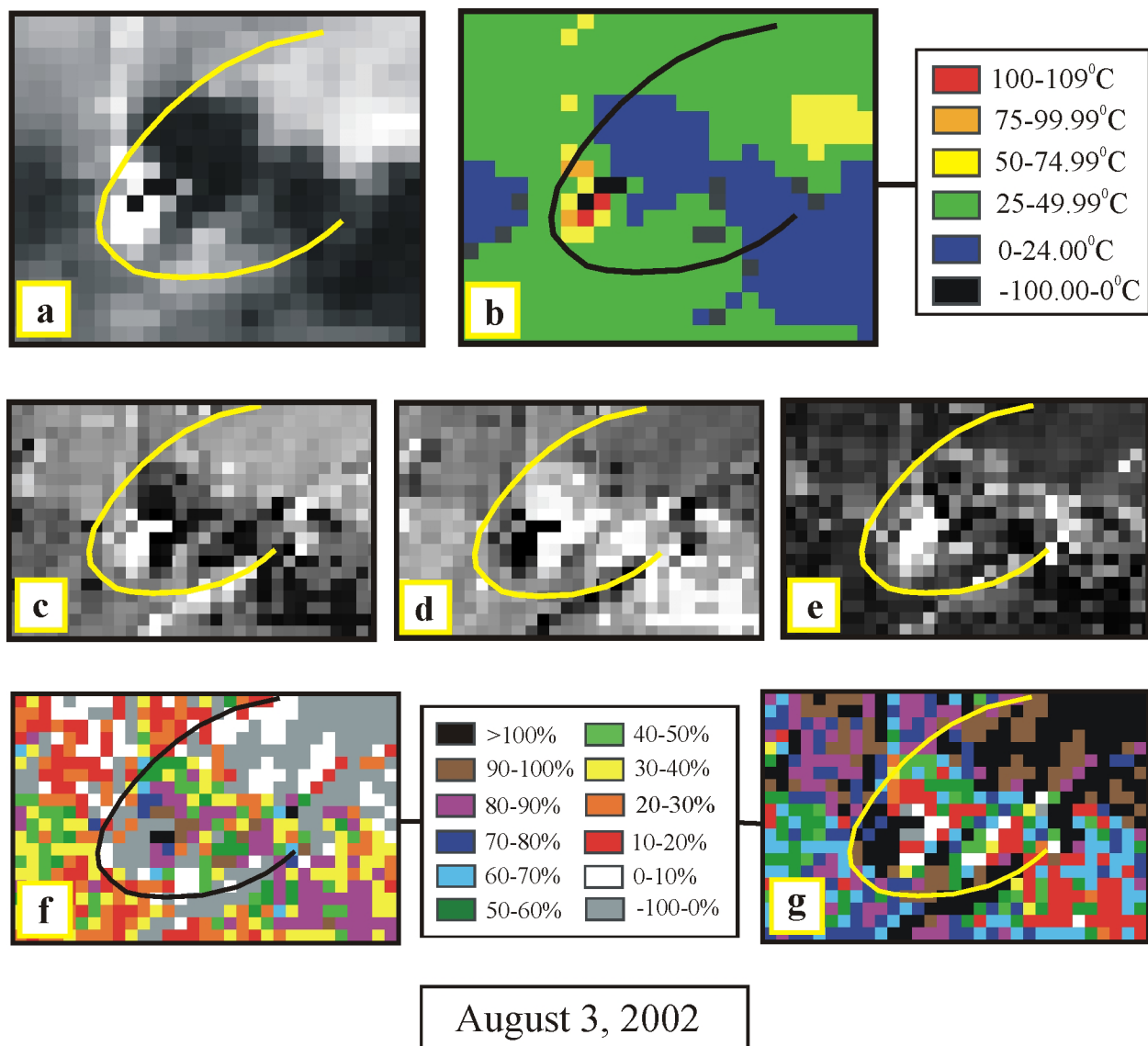


**Figure 27.** The subsets above are cropped to the same geographic area and are 2790m x 1800 m in dimension. The temperature anomaly is easily distinguished (a) and concentrated as seen in the color map (b). Cloud cover is visible (b) over the dome but does not appear to interfere with the view of the anomaly. The spectral deconvolution results, blackbody (c) and glass (d) are next to the RMS error results (e). A color map was applied to the blackbody results (f) and to the glass results (g) to illustrate the distribution of each on the dome and vicinity. English's Crater is outlined in yellow to establish the location and size of the thermal anomaly in the temperature and deconvolution results.

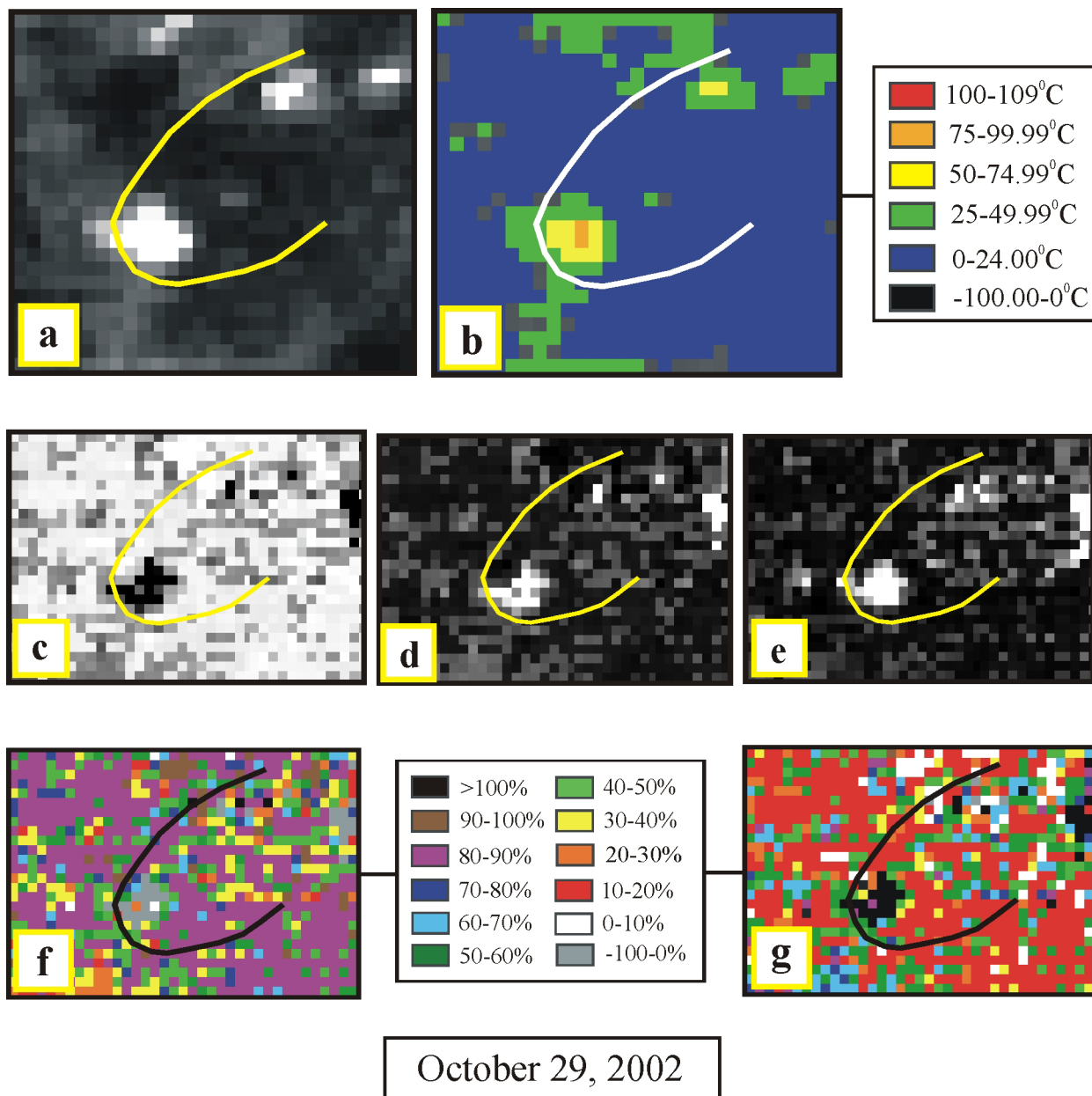
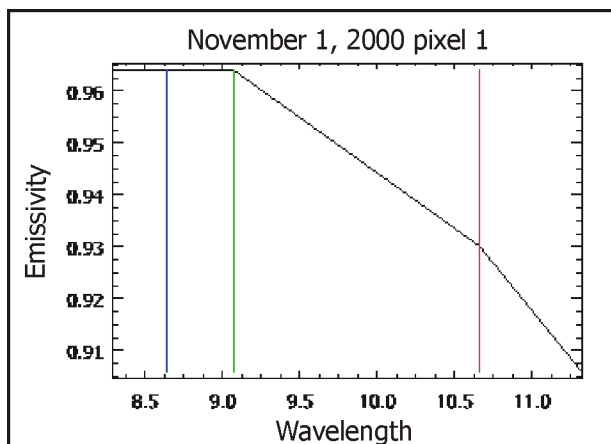
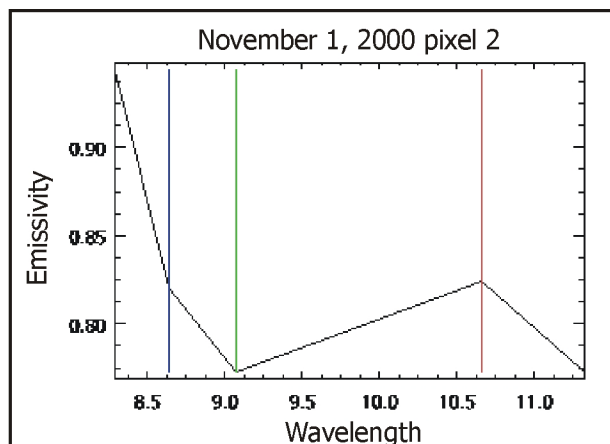


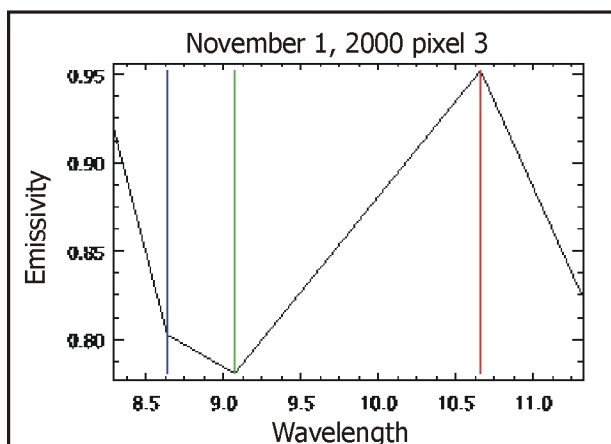
**Figure 28.** The subsets above are cropped to the same geographic area and are 2610m x 2340 m in dimension. The temperature anomaly is easily distinguished (a) and concentrated as seen in the color map, but not very high (b). Cloud cover is seen over most of the dome, but it is likely the majority of the anomaly is visible. The spectral deconvolution results, blackbody (c) and glass (d) are next to the RMS error results (e). A color map was applied to the blackbody results (f) and to the glass results (g) to illustrate the distribution of each on the dome and vicinity. English's Crater is outlined in yellow to establish the location and size of the thermal anomaly in the temperature and deconvolution results.



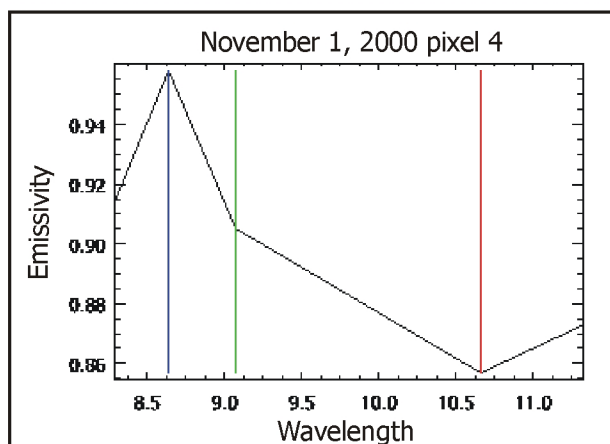
Pixel 1,  $T = 109^{\circ}\text{C}$



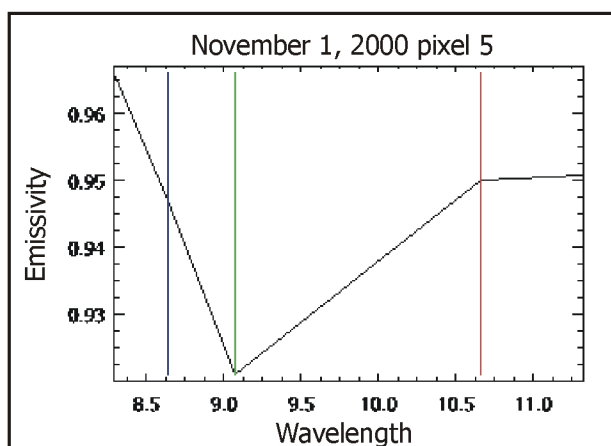
Pixel 2,  $T = 109^{\circ}\text{C}$



Pixel 3,  $T = 98^{\circ}\text{C}$

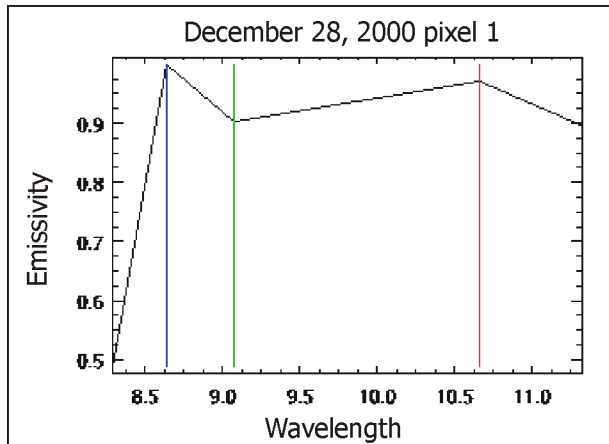


Pixel 4,  $T = 98^{\circ}\text{C}$

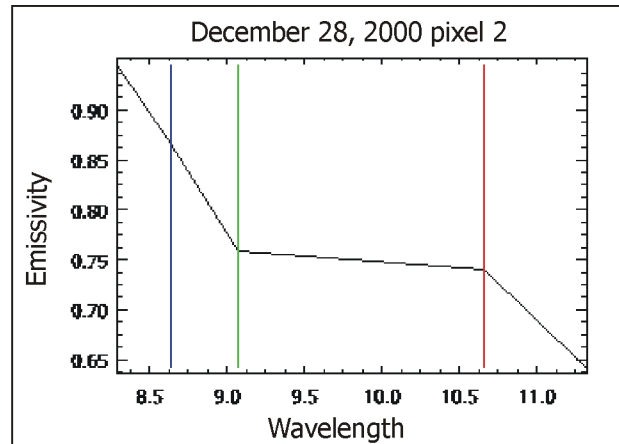


Pixel 5, off dome,  $T = 22^{\circ}\text{C}$

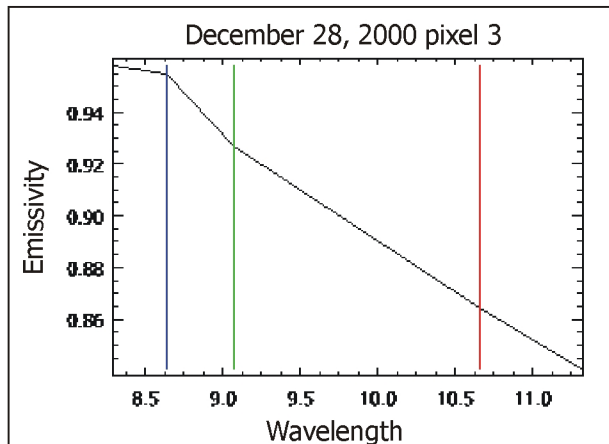
**Figure 29.** November 1, 2000. Emission spectra from the Level 2 emissivity image for the four hottest temperature pixels (pixels 1-4) within the thermal anomaly. Pixel 5 is a location outside of the thermal anomaly and illustrates a near-ideal glassy spectrum at background temperature.



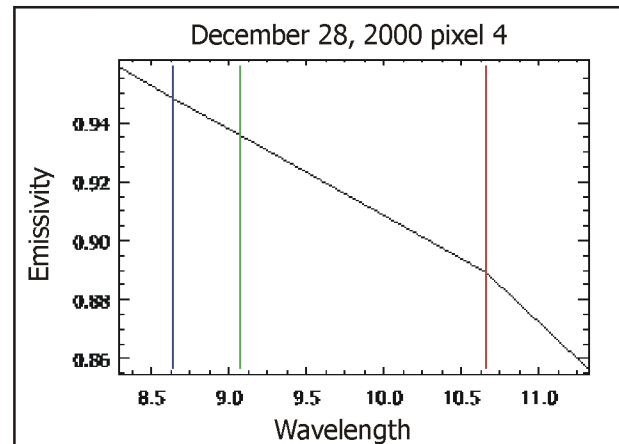
Pixel 1, T= 111°C



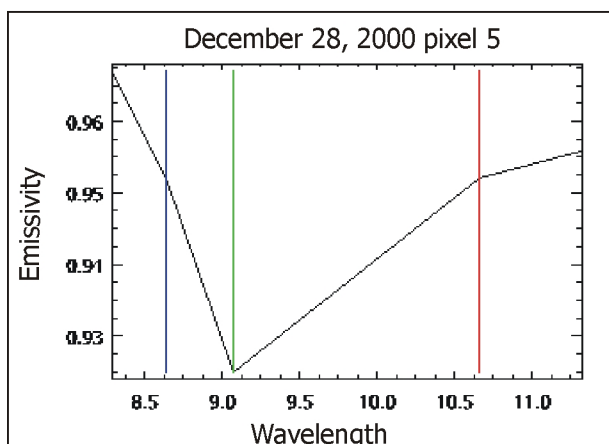
Pixel 2, T= 109°C



Pixel 3, T= 109°C

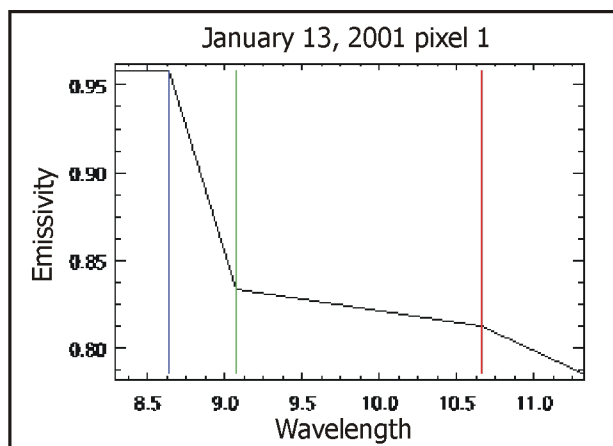


Pixel 4, T= 107°C

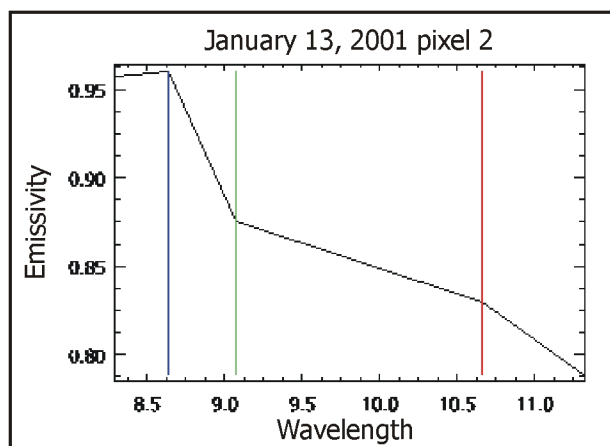


Pixel 5, off dome, T= 21°C

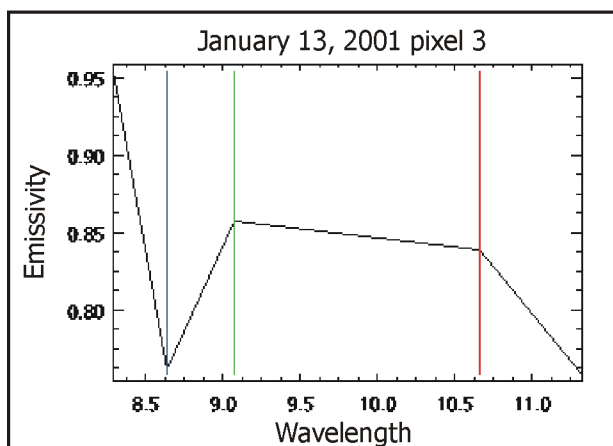
**Figure 30.** December 28, 2000. Emission spectra from the Level 2 emissivity image for the four hottest temperature pixels (pixels 1-4) within the thermal anomaly. Pixel 5 is a location outside of the thermal anomaly and illustrates a near-ideal glassy spectrum at background temperature.



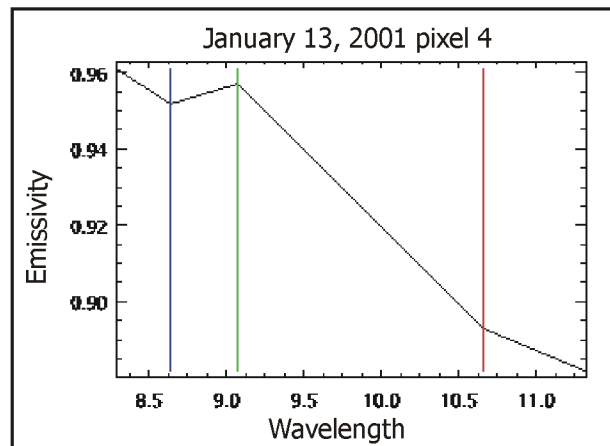
Pixel 1,  $T = 109^{\circ}\text{C}$



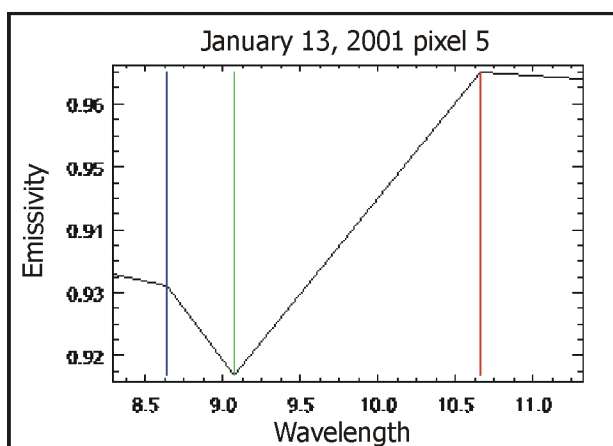
Pixel 2,  $T = 106^{\circ}\text{C}$



Pixel 3,  $T = 100^{\circ}\text{C}$

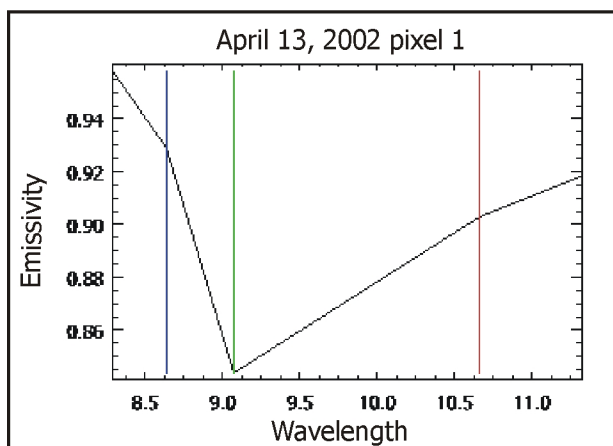


Pixel 4,  $T = 81^{\circ}\text{C}$

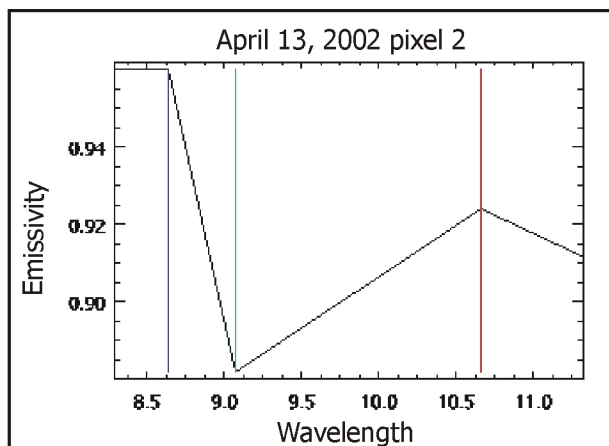


Pixel 5, off dome,  $T = 23^{\circ}\text{C}$

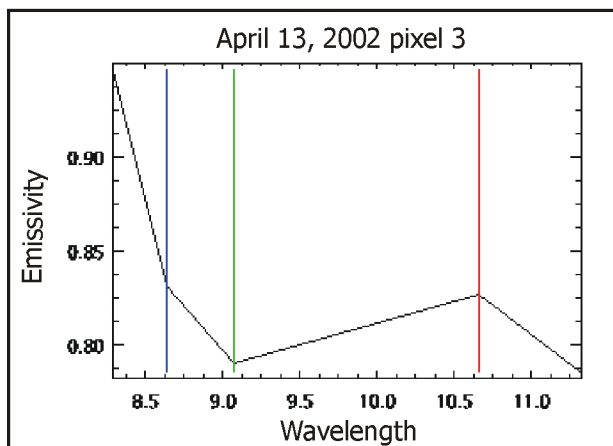
**Figure 31.** January 13, 2001. Emission spectra from the Level 2 emissivity image for the four hottest temperature pixels (pixels 1-4) within the thermal anomaly. Pixel 5 is a location outside of the thermal anomaly and illustrates a near-ideal glassy spectrum at background temperature.



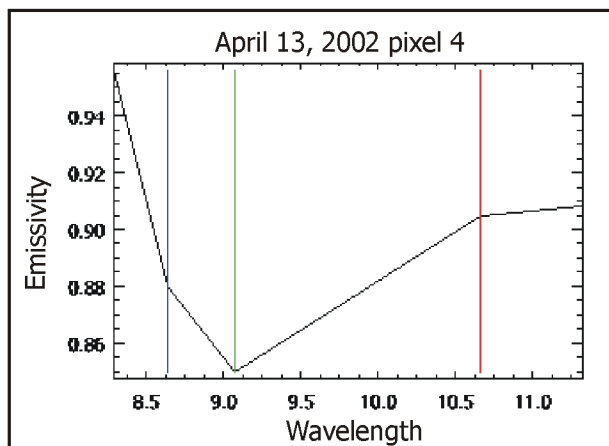
Pixel 1,  $T = 109^{\circ}\text{C}$



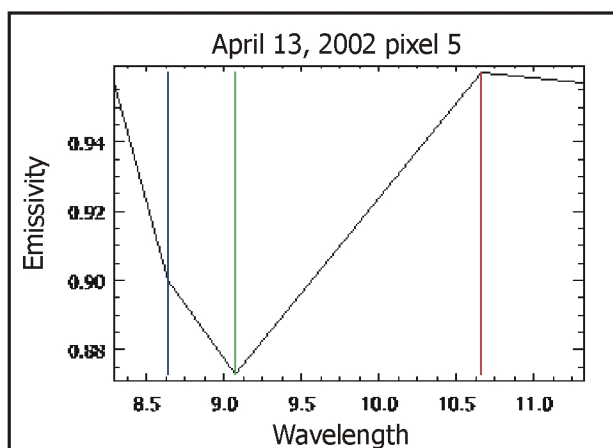
Pixel 2,  $T = 109^{\circ}\text{C}$



Pixel 3,  $T = 109^{\circ}\text{C}$

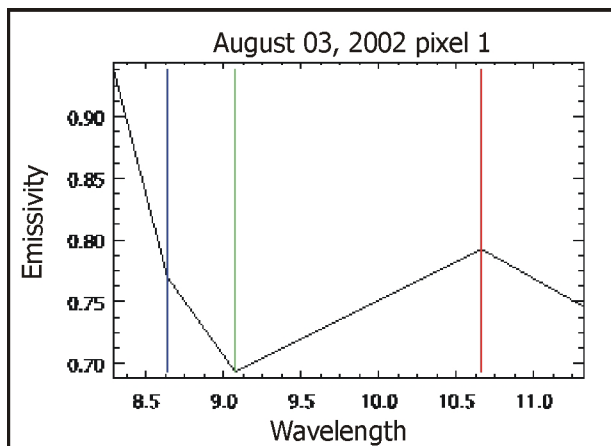


Pixel 4,  $T = 109^{\circ}\text{C}$

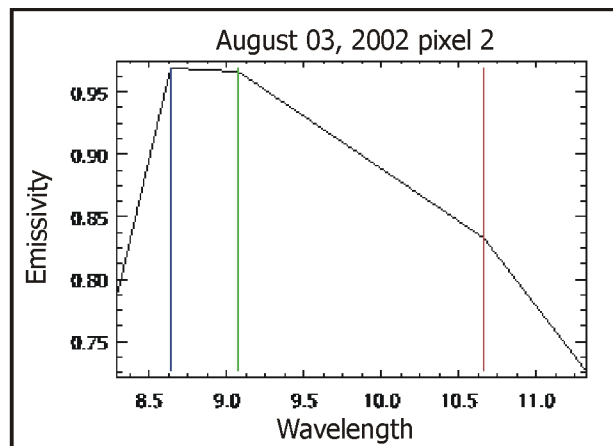


Pixel 5, off dome,  $T = 40^{\circ}\text{C}$

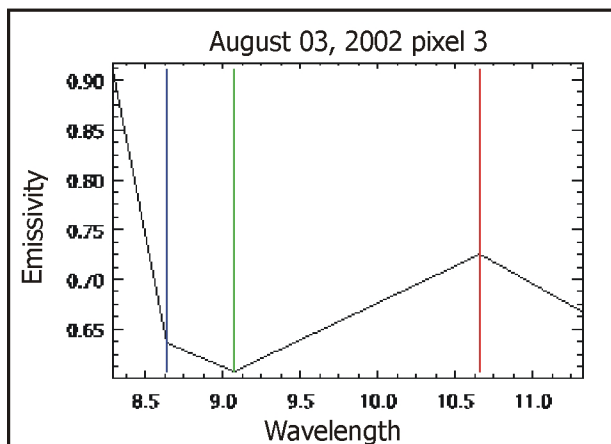
**Figure 32.** April 13, 2002. Emission spectra from the Level 2 emissivity image for the four hottest temperature pixels (pixels 1-4) within the thermal anomaly. Pixel 5 is a location outside of the thermal anomaly and illustrates a near-ideal glassy spectrum at background temperature.



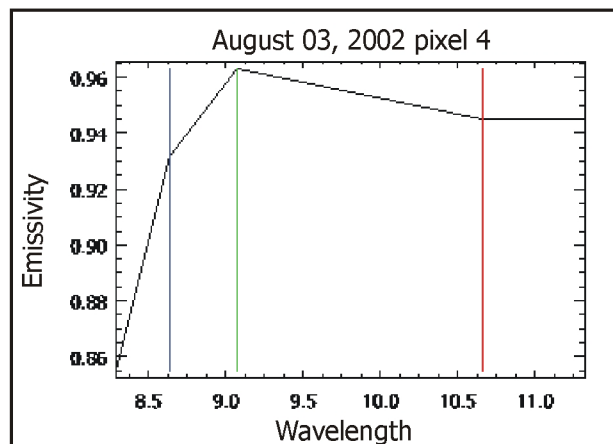
Pixel 1, T= 109°C



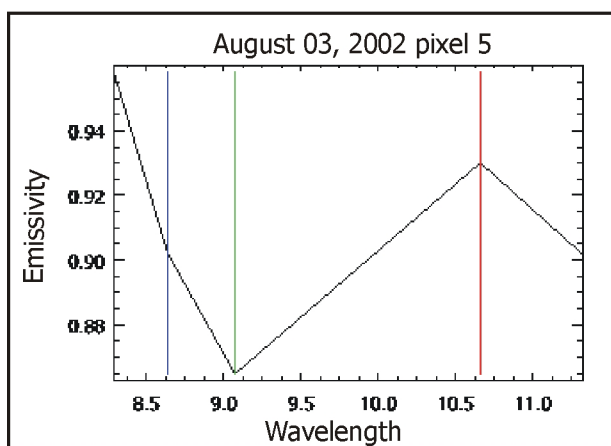
Pixel 2, T= 102°C



Pixel 3, T= 89°C

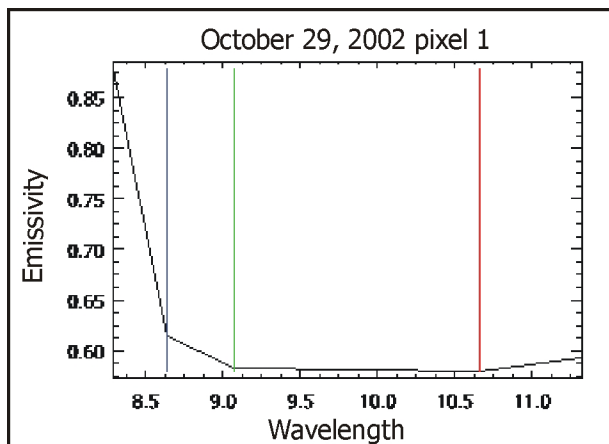


Pixel 4, T= 87°C

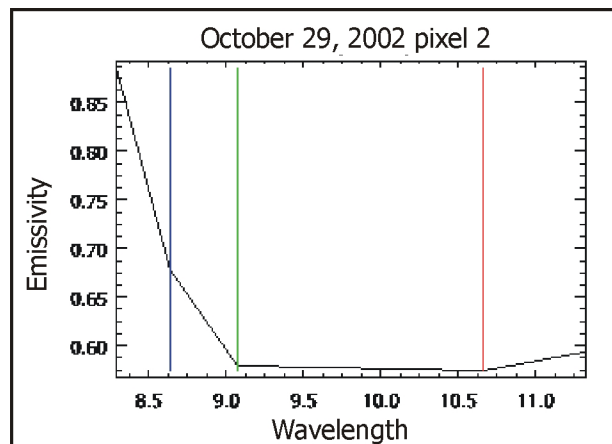


Pixel 5, off dome, T= 41°C

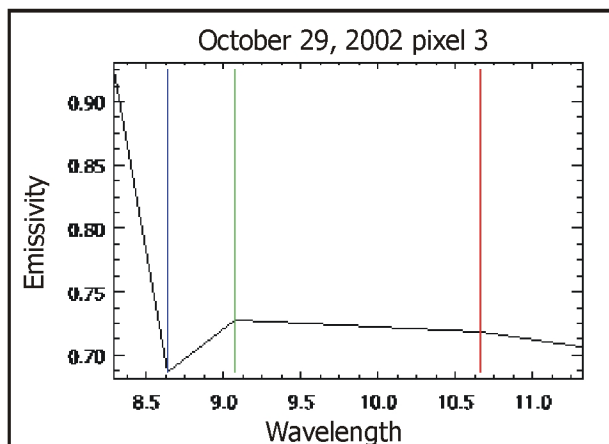
**Figure 33.** August 03, 2002. Emission spectra from the Level 2 emissivity image for the four hottest temperature pixels (pixels 1-4) within the thermal anomaly. Pixel 5 is a location outside of the thermal anomaly and illustrates a near-ideal glassy spectrum at background temperature.



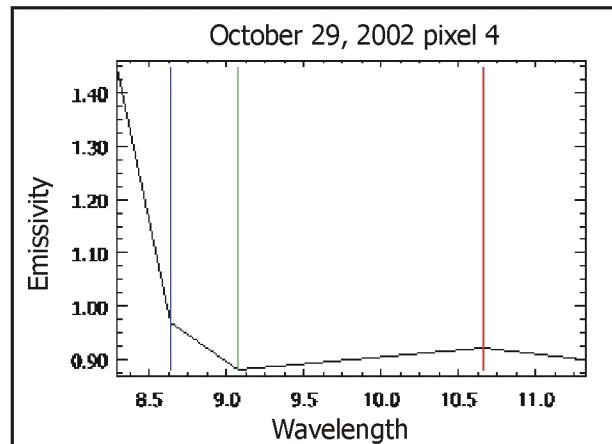
Pixel 1,  $T = 79^{\circ}\text{C}$



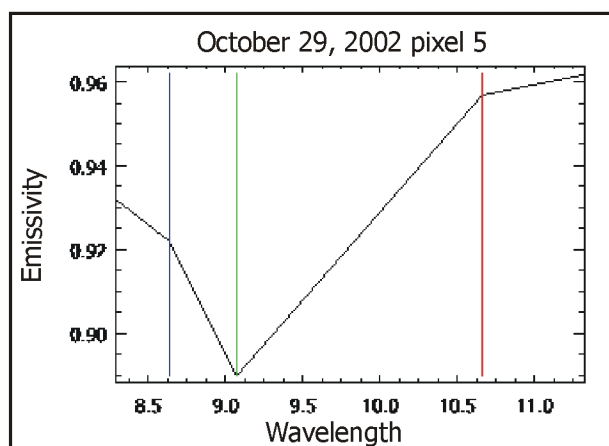
Pixel 2,  $T = 76^{\circ}\text{C}$



Pixel 3,  $T = 70^{\circ}\text{C}$



Pixel 4,  $T = 64^{\circ}\text{C}$



Pixel 5, off dome,  $T = 37^{\circ}\text{C}$

**Figure 34.** October 29, 2002. Emission spectra from the Level 2 emissivity image for the four hottest temperature pixels (pixels 1-4) within the thermal anomaly. Pixel 5 is a location outside of the thermal anomaly and illustrates a near-ideal glassy spectrum at background temperature.



April 13, 2002

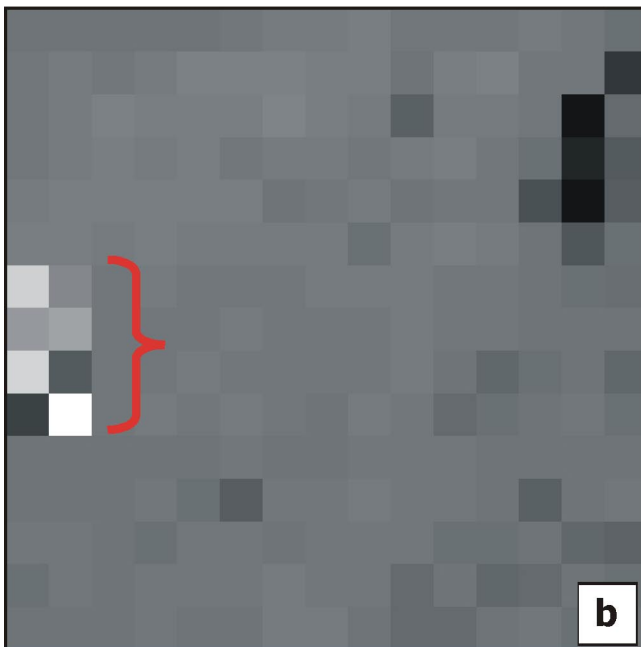
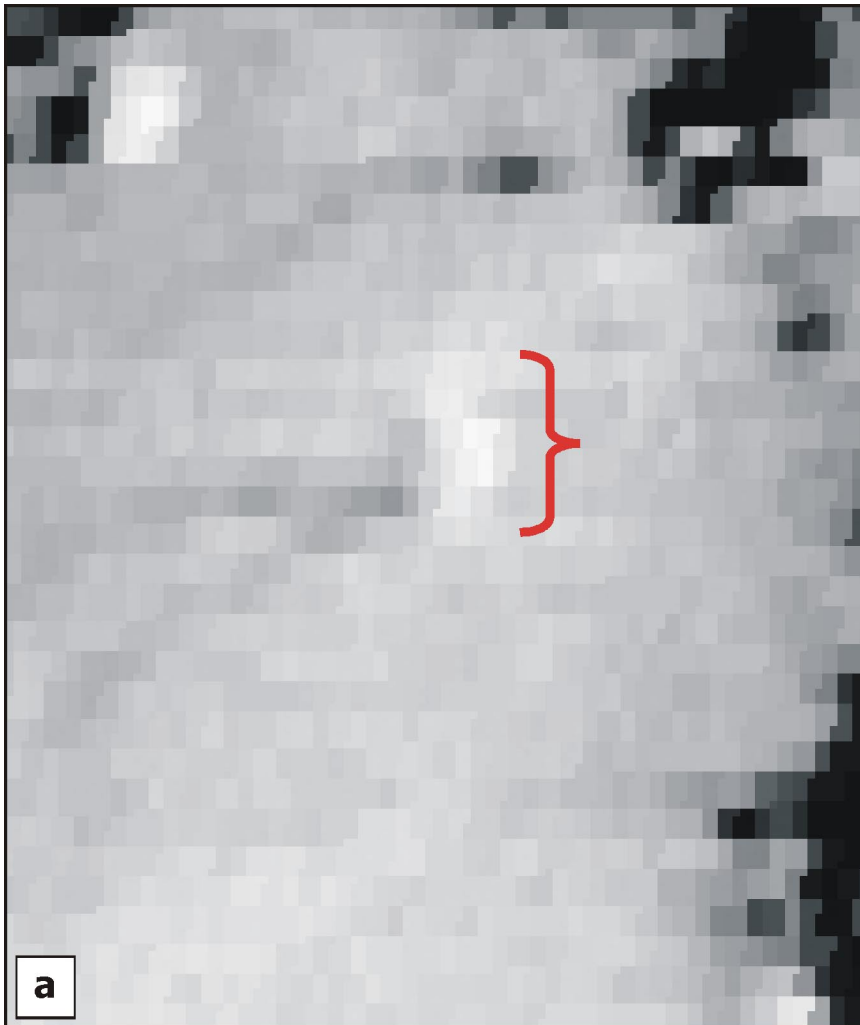


**Figure 35.** (a) Subset of GOES satellite image with the island of Montserrat at the image center. GOES 4x4 km pixels are resampled to 1x1 km (to visually increase spatial resolution) and the original pixel value is assigned to each of the four new pixels. (b) ASTER image resampled to 4x4 km pixels to mimic the GOES spatial resolution. (a, b) The red bracket indicates the northern and southern boundaries of the island.

## Weekly Occurrences of Rockfall

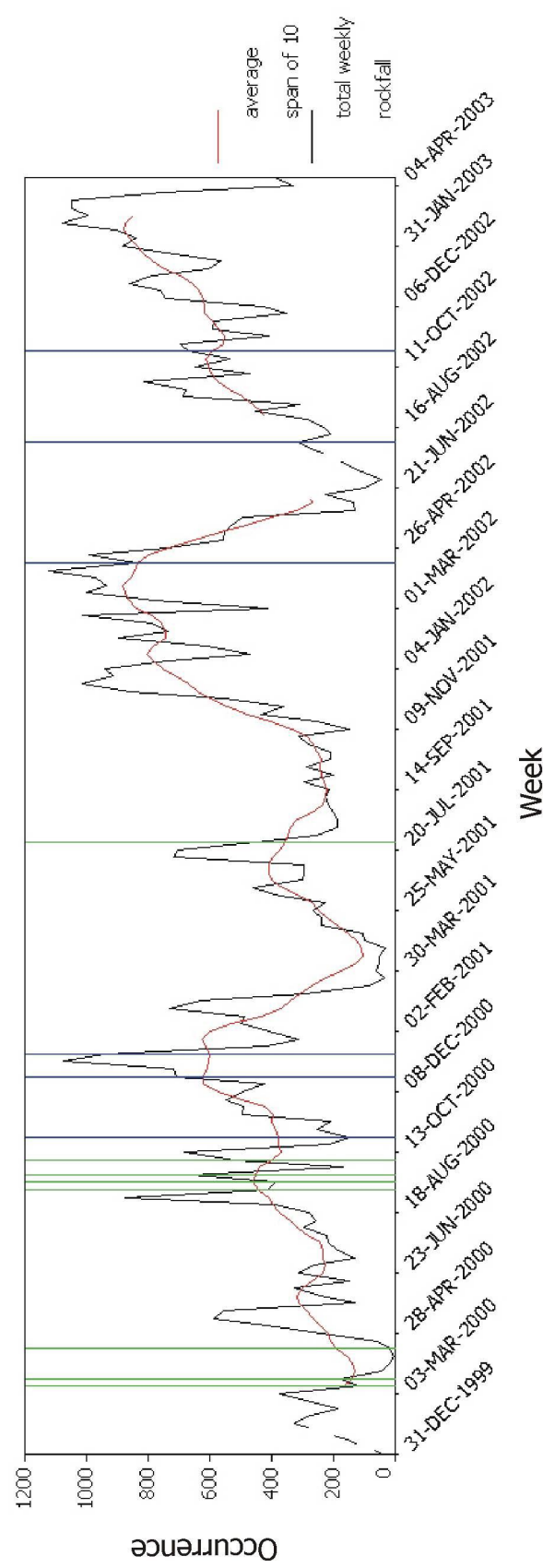


**Figure 36.** Rockfall Signals. Graphic representation of the weekly occurrences of rockfall signals derived from the database of Soufrière Hills volcanic activity (Appendix 1). Green bars denote weeks with explosive volcanic activity. Blue bars represent ASTER image acquisition.

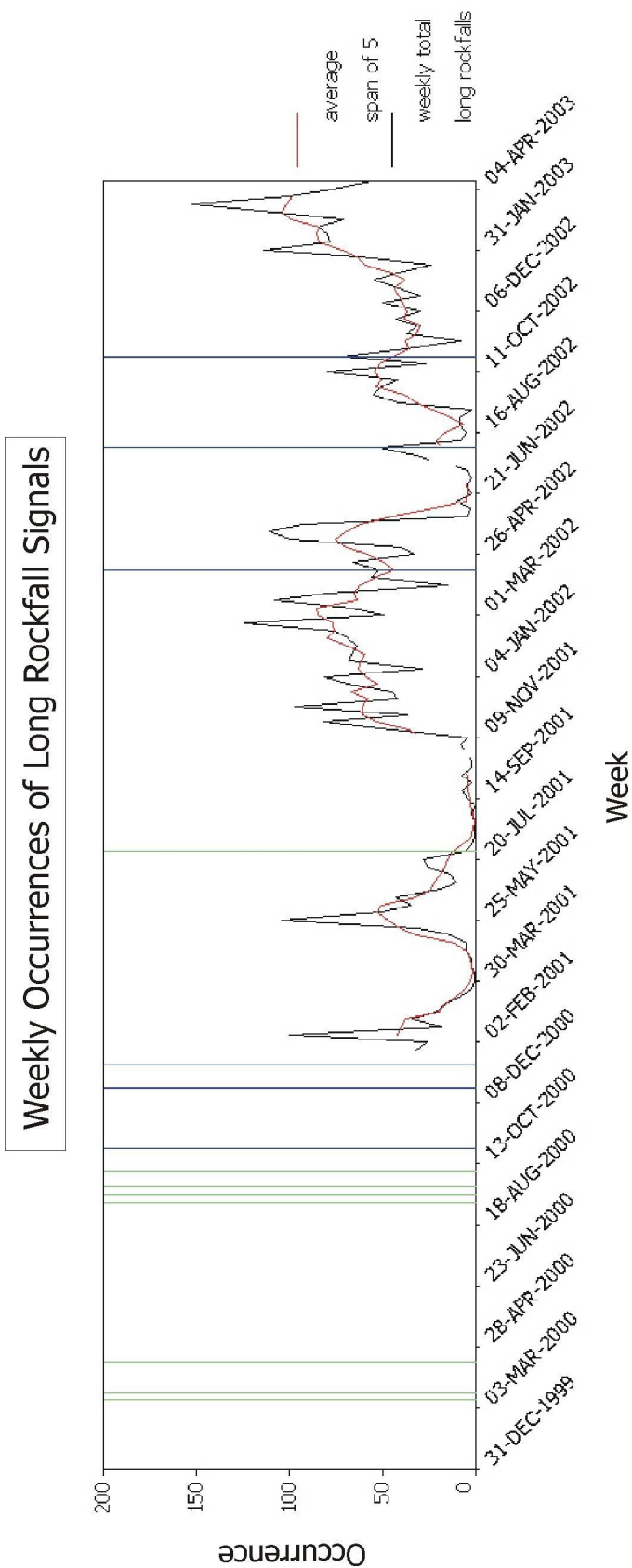


**Figure 37.** Long Rockfall Signals. Graphic representation of the weekly occurrences of long rockfall seismic signals derived from the database of Soufrière Hills volcanic activity (Appendix 1). Green bars denote weeks with explosive volcanic activity. Blue bars represent ASTER image acquisition.

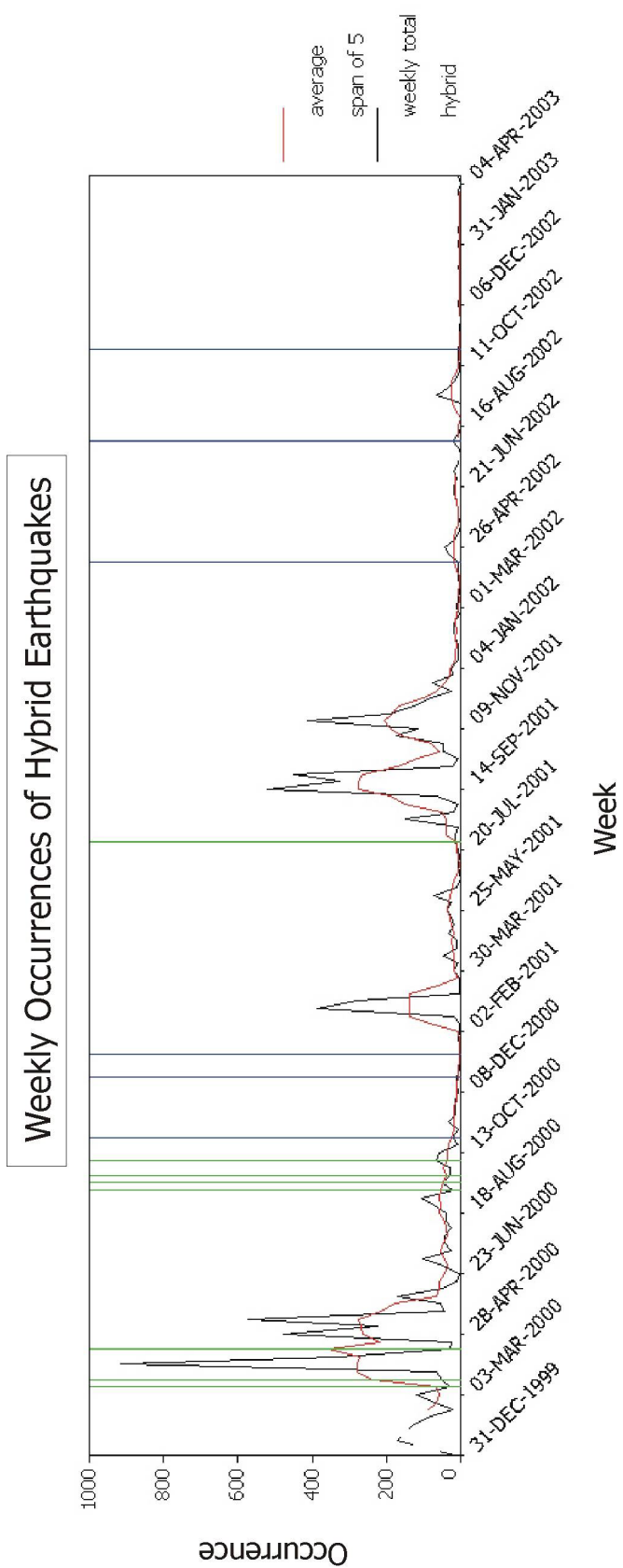


**Figure 38.** Hybrid Earthquakes. Graphic representation of the weekly occurrences of hybrid earthquakes derived from the database of Soufrière Hills volcanic activity (Appendix 1). Green bars denote weeks with explosive volcanic activity. Blue bars represent ASTER image acquisition.

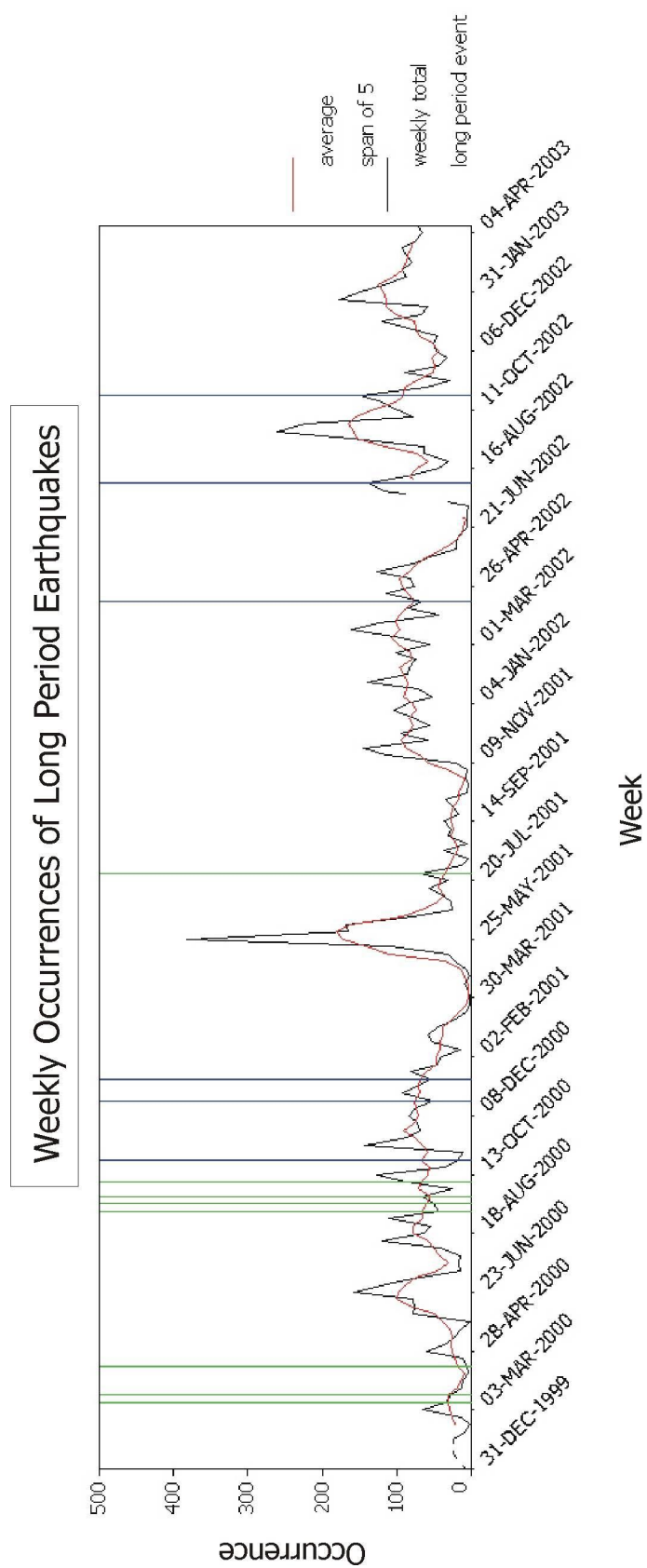


**Figure 39.** Long Period Earthquakes. Graphic representation of the weekly occurrences of long period earthquakes derived from the database of Soufrière Hills volcanic activity (Appendix 1). Green bars denote weeks with explosive volcanic activity. Blue bars represent ASTER image acquisition.

## Weekly Occurrences of Volcano-tectonic Earthquakes

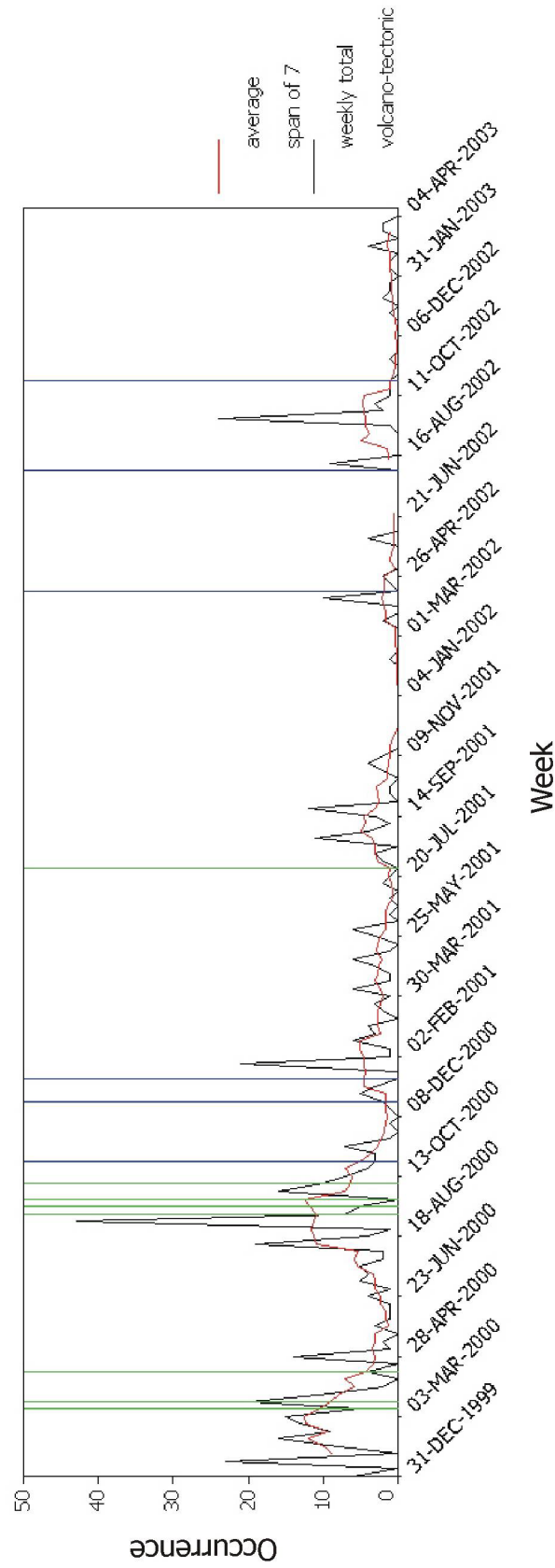


**Figure 40.** Volcano-tectonic Earthquakes. Graphic representation of the weekly occurrences of volcano-tectonic earthquakes derived from the database of Soufrière Hills volcanic activity (Appendix 1). Green bars denote weeks with explosive volcanic activity. Blue bars represent ASTER image acquisition.

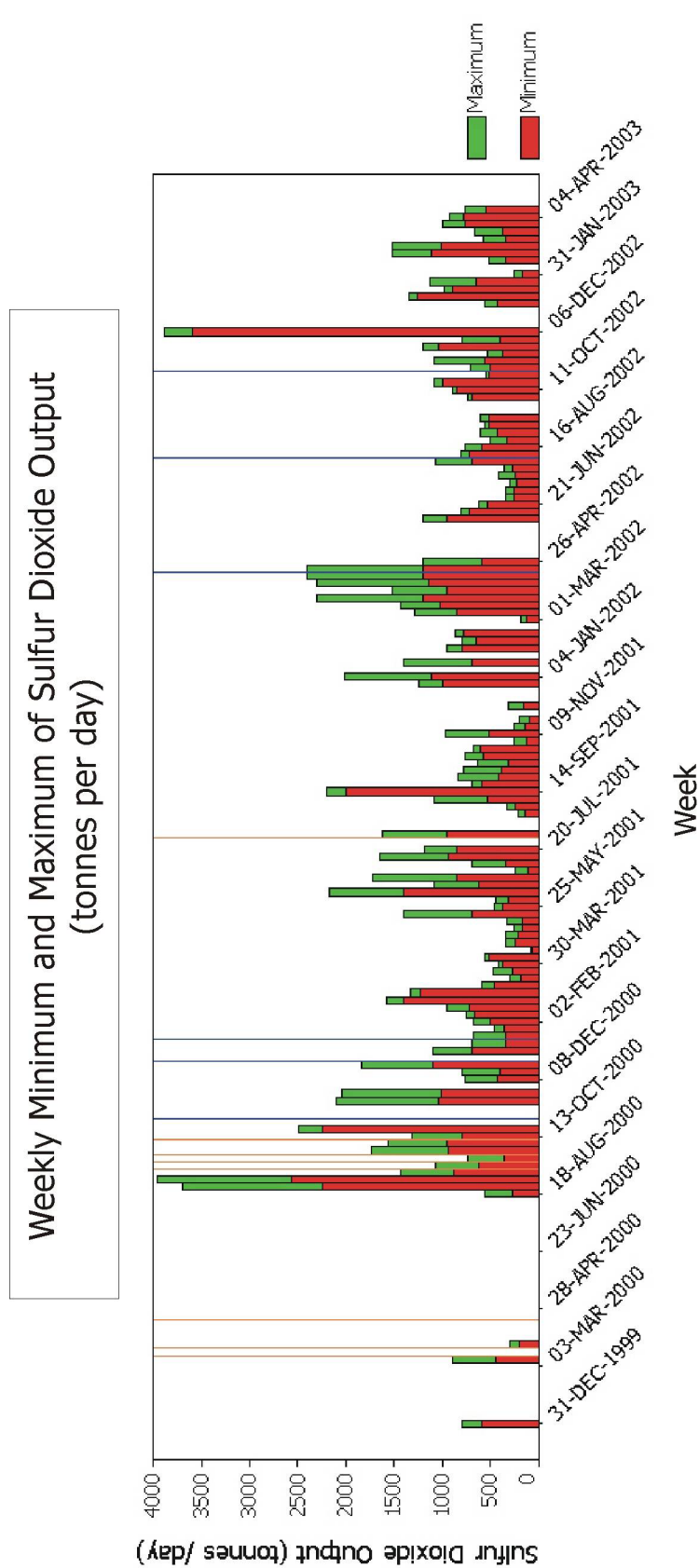
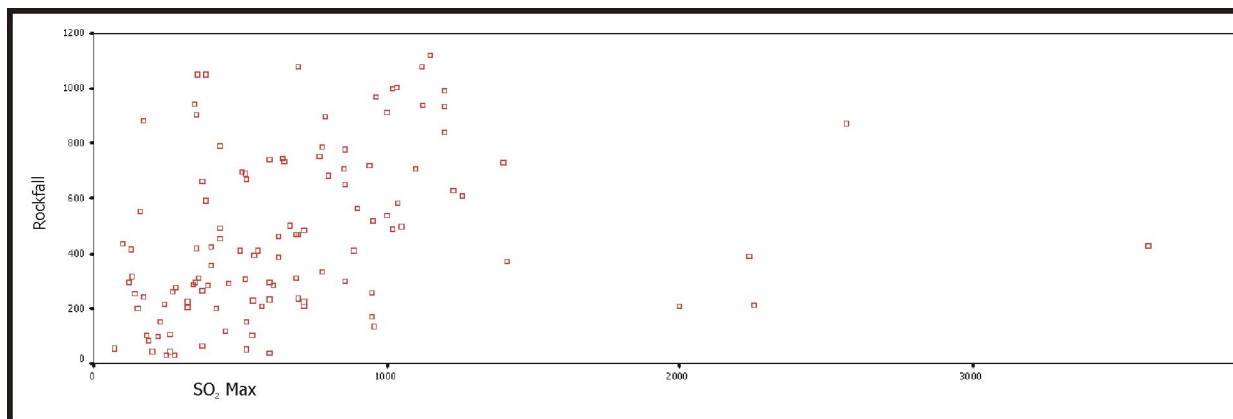


**Figure 41.** Sulfur Dioxide Output. Graphic representation of the weekly maximum and minimum sulfur dioxide output, in tonnes per day, derived from the database of Soufrière Hills volcanic activity (Appendix 1). Orange bars denote weeks with explosive volcanic activity. Blue bars represent ASTER image acquisition.



ANOVA<sup>b</sup>

Model		Sum of Squares	df	Mean Square	F	Sig.
1	Regression	841385.2	1	841385.192	10.375	.002 <sup>a</sup>
	Residual	9163953	113	81096.927		
	Total	10005338	114			

a. Predictors: (Constant), MAX

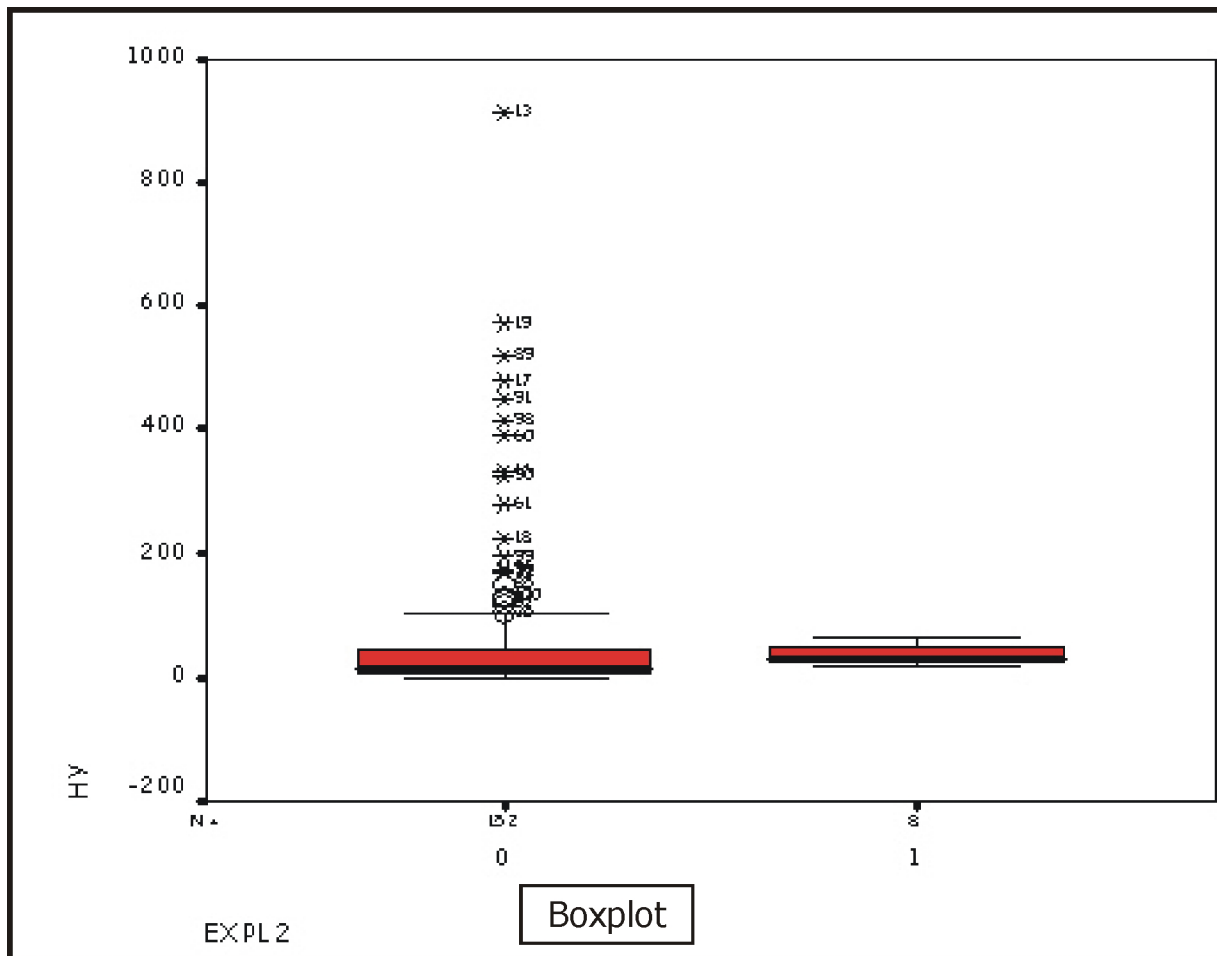
b. Dependent Variable: RKFL

Coefficients <sup>a</sup>						
Model		Unstandardized Coefficients		Standardized Coefficients	t	Sig.
		B	Std. Error	Beta		
1	(Constant)	353.986	43.998		8.045	.000
	MAX	.164	.051	.290	3.221	.002

a. Dependent Variable: RKFL

**Figure 42.** Statistical analysis and plot of sulfur dioxide and rockfall occurrence.





Chi-Square Tests					
	Value	df	Asymp. Sig. (2-sided)	Exact Sig. (2-sided)	Exact Sig. (1-sided)
Pearson Chi-Square	7.621 <sup>b</sup>	1	.006	.008	.008
Continuity Correction <sup>a</sup>	5.720	1	.017		
Likelihood Ratio	7.968	1	.005	.022	.008
Fisher's Exact Test				.008	.008
N of Valid Cases	162				

a. Computed only for a 2x2 table

b. 2 cells (50.0%) have expected count less than 5. The minimum expected count is 3.26.

**Figure 43.** Boxplot and chi-square analysis of explosive occurrence versus total hybrid earthquake events per week.

Independent Samples Test									
		Levene's Test for Equality of Variances		t-test for Equality of Means					
		F	Sig.	t	df	Sig. (2-tailed)	Mean Difference	Std. Error Difference	95% Confidence Interval of the Difference
RKFL	Equal variances assumed	3.859	.051	-3.200	165	.002	-142.49	44.527	-230.401 -54.569
	Equal variances not assumed			-3.299	155.226	.001	-142.49	43.192	-227.804 -57.166

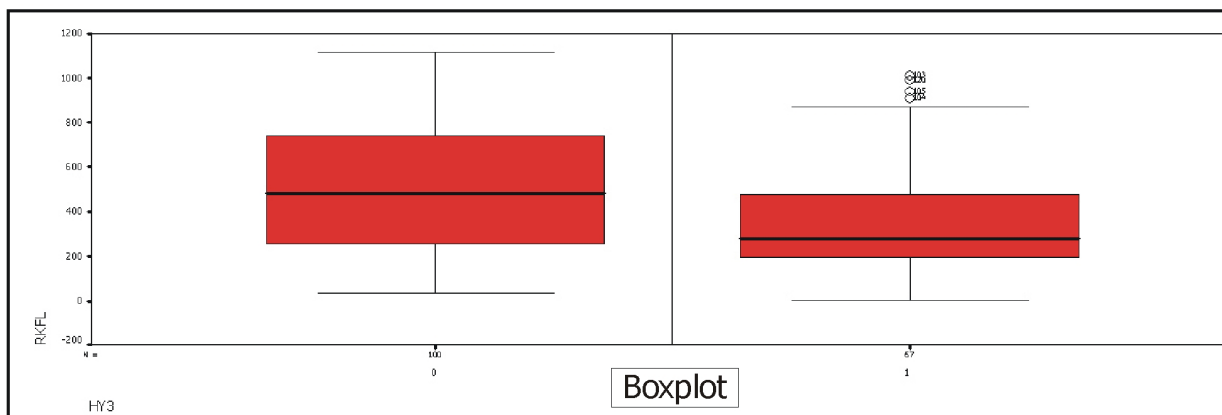


**Figure 44.** Independent sample tests and boxplot analysis for hybrid seismic signals versus rockfall occurrence.

## GOES and ASTER Temperature Comparison

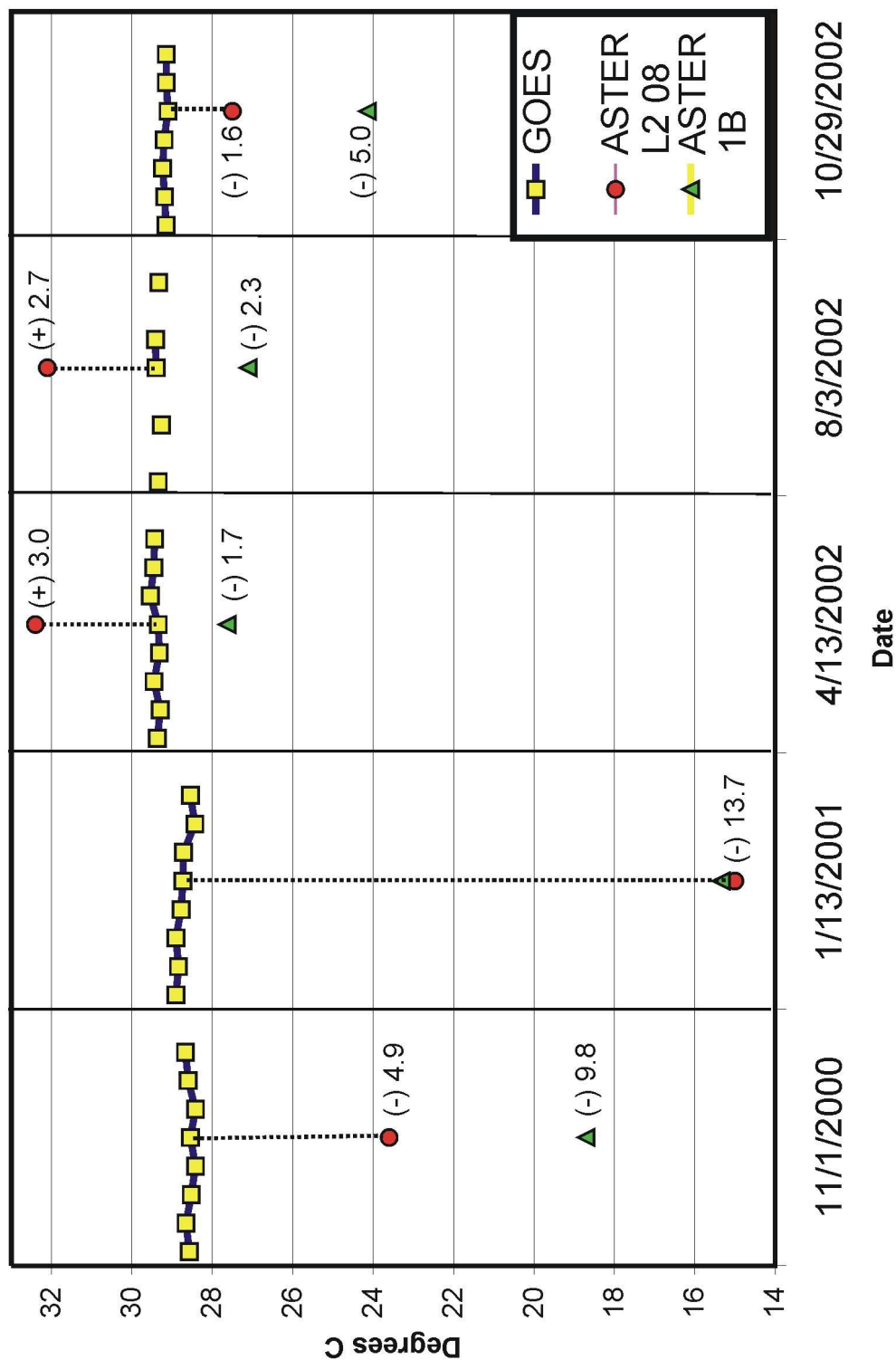


**Figure 45.** GOES versus ASTER temperature graph. Two hours of GOES temperature data, acquired every 15 minutes, were compared to ASTER Level 2 and Level 1B derived temperatures. GOES data was unavailable for 12/28/2000.

<b>ASTER</b>	<b><math>\lambda</math> region</b>	<b>band</b>	<b>spectral range, <math>\mu\text{m}</math></b>	<b>peak <math>\lambda</math>, <math>\mu\text{m}</math></b>	<b>spatial resolution, m</b>
	<b>VNIR</b>	1	0.520-0.600	0.556	15
		2	0.630-0.690	0.661	15
		3	0.760-0.860	0.807	15
	<b>SWIR</b>	4	1.600-1.700	1.656	30
		5	2.145-2.185	2.167	30
		6	2.185-2.225	2.209	30
		7	2.235-2.285	2.262	30
		8	2.295-2.365	2.336	30
		9	2.360-2.430	2.400	30
	<b>TIR</b>	10	8.125-8.475	8.291	90
		11	8.475-8.825	8.634	90
		12	8.925-9.275	9.075	90
		13	10.250-10.950	10.657	90
		14	10.950-11.650	11.318	90
<b>GOES</b>	<b><math>\lambda</math> region</b>	<b>band</b>	<b>spectral range, <math>\mu\text{m}</math></b>	<b>peak <math>\lambda</math>, <math>\mu\text{m}</math></b>	<b>spatial resolution, km</b>
	<b>VNIR</b>	1	0.520-0.720	0.620	1
	<b>SWIR</b>	2	3.780-4.030	3.905	4
		3	6.470-7.020	6.745	8
	<b>TIR</b>	4	10.300-11.300	10.800	4
		5	11.500-12.500	12.000	4
<b>AVHRR</b>	<b><math>\lambda</math> region</b>	<b>band</b>	<b>spectral range, <math>\mu\text{m}</math></b>	<b>peak <math>\lambda</math>, <math>\mu\text{m}</math></b>	<b>spatial resolution, km</b>
	VNIR	1	0.580-0.680	0.630	1.1 at nadir
	VNIR,SWR	2	0.725-1.100	0.913	1.1 at nadir
	SWIR	3	3.550-3.930	3.740	1.1 at nadir
	TIR	4	10.300-11.300	10.800	1.1 at nadir
		5	11.400-12.400	11.900	1.1 at nadir
<b>Landsat 7 ETM+</b>	<b><math>\lambda</math> region</b>	<b>band</b>	<b>spectral range, <math>\mu\text{m}</math></b>	<b>peak <math>\lambda</math>, <math>\mu\text{m}</math></b>	<b>spatial resolution, m</b>
	VNIR	1	0.450-0.515	0.482	30
		2	0.525-0.605	0.565	30
		3	0.630-0.690	0.660	30
		4	0.750-0.900	0.825	30
	SWIR	5	1.550-1.750	1.650	30
	TIR	6	10.400-12.500	11.450	60
	SWIR	7	2.090-2.350	2.220	30
	VNIR	8	0.520-0.900	0.710	15

**Table 1.** Instrument Specifications. Spatial and spectral resolutions of the ASTER, GOES, AVHRR, and Landsat 7 ETM + instruments.

Date	Goes ID	GOES acq. time	ASTER acq. time	GOES °C	ASTER L1B °C	L2 08 °C	L2 TES °C
1-Nov-00	20001101.0145.g08.5	1:45		28.57			
	20001101.0202.g08.5	2:02		28.66			
	20001101.0215.g08.5	2:15		28.52			
	20001101.0232.g08.5	2:32		28.42			
	20001101.0245.g08.5	2:45	2:44	28.54	18.7	23.6	23.77
	20001101.0315.g08.5	3:15		28.42			
	20001101.0332.g08.5	3:32		28.59			
	20001101.0345.g08.5	3:45		28.67			
13-Jan-01	20010113.0132.g08.5	1:32		28.90			
	20010113.0145.g08.5	1:45		28.84			
	20010113.0202.g08.5	2:02		28.90			
	20010113.0215.g08.5	2:15		28.78			
	20010113.0232.g08.5	2:32	2:37	28.73	15.34	15	22.16
	20010113.0245.g08.5	2:45		28.71			
	20010113.0315.g08.5	3:15		28.43			
	20010113.0332.g08.5	3:32		28.55			
13-Apr-02	20020413.1345.g08.5	13:45		29.36			
	20020413.1402.g08.5	14:02		29.29			
	20020413.1415.g08.5	14:15		29.45			
	20020413.1432.g08.5	14:32		29.32			
	20020413.1445.g08.5	14:45	14:45	29.34	27.63	32.4	33.11
	20020413.1515.g08.5	15:15		29.54			
	20020413.1532.g08.5	15:32		29.46			
	20020413.1545.g08.5	15:45		29.43			
3-Aug-02	20020803.1345.g08.5	13:45		29.34			
	20020803.1402.g08.5	14:02		no data			
	20020803.1415.g08.5	14:15		29.27			
	20020803.1432.g08.5	14:32		no data			
	20020803.1445.g08.5	14:45	14:45	29.40	27.11	32.1	31.85
	20020803.1515.g08.5	15:15		29.41			
	20020803.1532.g08.5	15:32		no data			
	20020803.1545.g08.5	15:45		29.33			
29-Oct-02	20021029.1345.g08.5	13:45		29.15			
	20021029.1402.g08.5	14:02		29.19			
	20021029.1415.g08.5	14:15		29.24			
	20021029.1432.g08.5	14:32		29.20			
	20021029.1445.g08.5	14:45	14:50	29.11	24.14	27.5	0
	20021029.1515.g08.5	15:15		29.14			
	20021029.1532.g08.5	15:32		29.14			

**Table 2.** GOES and ASTER temperature data.

<b>EOS/DAAC SEARCH ID#</b>	<b>time</b>	<b>Level 2 ID</b>	<b>acquisition date</b>	<b>Time</b>
SC:AST_L1B.002:2002055921	night	AST_(05,08,09T)_002110120000244250030000.hdf	11/1/2000	`02:44:25.798
SC:AST_L1B.002:2002223440	night	AST_(05,08,09T)_003122820000237350000000.hdf	12/28/2000	`02:37:35.707
SC:AST_L1B.002:2002324250	night	AST_(05,08,09T)_002011320010237010000000.hdf	1/13/2001	`02:37:01.773
SC:AST_L1B.003:2006733777	day	AST_(05,08,09T)_003041320021444500010000.hdf	4/13/2002	`14:44:50.132
SC:AST_L1B.003:2007995109	day	AST_(05,08,09T)_003080320021445040010000.hdf	8/3/2002	`14:45:04.7
SC:AST_L1B.003:2009032131	day	AST_(05,08,09T)_003102920021450520000000.hdf	10/29/2002	`14:50:52.95

<b>EOS/DAAC SEARCH ID#</b>	<b>Scene orientation ----&gt;</b>	<b><math>\Delta</math></b>	<b>upper left</b>	<b>upper right</b>
SC:AST_L1B.002:2002055921	(+) 8.602965		16.406209, -62.026485	16.307261, -62.718334
SC:AST_L1B.002:2002223440	(+) 9.01326		16.206934, -61.856423	16.103735, -62.546877
SC:AST_L1B.002:2002324250	(+) 9.031917		16.267002, -61.449878	16.16493, -62.140641
SC:AST_L1B.003:2006733777	(+) 7.986423	(-)	17.049520, -62.247559	16.352391, -62.4056
SC:AST_L1B.003:2007995109	(+) 7.986423	(-)	17.059518, -62.319809	16.962208, -61.62542
SC:AST_L1B.003:2009032131	(+) 8.427692	(-)	16.870429, -62.530713	16.768721, -61.837667

**Table 3.** Metadata for the six ASTER study images. Table shows separate identification numbers, acquisition date and time, scene orientation angle, and upper left and upper right geographic information for each image.

<b>image ID</b>	<b>pixel</b>	<b>location</b>	<b>temp °C</b>	<b>blackbody</b>	<b>glass</b>	<b>RMS error</b>
Nov. 1, 2000	1	704,306	109.05	86.8	9.2	0.029431
	2	704,305	109.05	-40.2	134.7	0.063197
	3	705,306	97.75	-44.0	141.3	0.054084
	4	703,306	97.55	53.1	41.5	0.04531
	5	702,309	22.35	48.1	50.8	0.009089
Dec. 28, 2000	1	543,30	110.75	66.5	22.6	0.177808
	2	544,31	109.05	-21.2	111.1	0.11375
	3	545,32	109.05	71.5	22.4	0.054509
	4	546,32	107.35	73.9	20.6	0.045859
	5	557,17	20.75	50.7	48.4	0.007894
Jan. 13, 2001	1	54,33	109.05	19.5	74.6	0.076313
	2	53,34	106.45	46.6	46.7	0.07328
	3	55,34	99.65	8.5	83.2	0.082537
	4	53,35	81.45	84.1	10.7	0.040647
	5	79,26	22.75	41.8	57.1	0.012682
Apr. 13, 2002	1	145,397	109.05	-0.4	99.6	0.020984
	2	146,397	109.05	31.0	67.4	0.024798
	3	147,397	109.05	-29.4	123.9	0.060481
	4	150,403	109.05	-2.5	100.8	0.022461
	5	155,391	39.85	8.3	91.9	0.013800
Aug. 3, 2002	1	228,399	109.05	-95.9	190.9	0.070578
	2	229,398	101.95	124.3	-38.8	0.102181
	3	227,399	88.75	-160.6	253.1	0.096624
	4	228,396	86.95	77.5	17.6	0.043045
	5	239,385	41.45	12.4	85.9	0.022669
Oct. 29, 2002	1	443,132	79.25	-168.8	256.7	0.124764
	2	443,131	75.65	-161.0	249.4	0.124885
	3	442,131	70.35	-80.3	171.0	0.096466
	4	442,132	64.15	21.1	86.7	0.191299
	5	430,160	37.15	22.8	76.7	0.009618

**Table 4.** Spectral deconvolution results. The Level 2 temperature image was used to locate the four highest temperature pixels and one pixel at background temperature. The pixel location and temperature for each is included. The results for each end-member are reported as aerial percentages.

## Appendix 1 - Database

row	date	days	aster	dgrowth	dsize	dpat	directio	pyrsize	pyrsourc	dir2	ash	exp12	expl	fume	glow	rkfl	lonrk	hy	loneq	teceq	min	max	nhy	hy2	hy3	mud
1	31-Dec-99	1	.	1	2	.	.	0	0	0	0	0	0	0	0	38	.	19	8	6	200	600	2	0	0	0
2	7-Jan-00	8	.	0	.	.	.	0	0	0	0	0	0	0	0	.	.	.	.	0	.	.	.	1	1	0
3	14-Jan-00	15	.	1	2	.	.	1	0	1	1	0	0	0	1	156	.	169	24	23	.	.	2	1	1	0
4	21-Jan-00	22	.	0	.	.	.	0	0	0	0	0	0	0	0	.	.	.	.	0	.	.	.	1	1	0
5	28-Jan-00	29	.	1	2	.	.	1	2	1	2	0	0	0	0	326	.	127	23	8	.	.	2	1	1	0
6	11-Feb-00	43	.	1	2	.	5	1	0	0	1	0	0	0	0	288	.	89	9	16	.	.	2	1	1	0
7	18-Feb-00	50	.	1	2	.	.	0	0	0	1	0	0	0	1	188	.	23	2	9	.	.	2	0	1	0
8	25-Feb-00	57	.	1	2	.	.	0	0	0	0	0	0	2	1	271	.	70	12	13	.	.	2	1	1	0
9	3-Mar-00	64	.	1	2	.	2	0	0	0	0	0	0	1	0	376	.	119	65	15	.	.	2	1	1	0
10	10-Mar-00	71	.	-1	1	1	3	2	0	1	3	1	1	2	0	119	.	29	35	5	450	450	2	1	1	1
11	17-Mar-00	78	.	0	.	.	.	1	3	.	3	1	3	1	0	180	.	49	27	20	.	.	2	1	1	1
12	24-Mar-00	85	.	1	.	.	.	0	0	0	1	0	0	1	0	43	.	64	12	9	100	200	2	1	1	1
13	31-Mar-00	92	.	1	2	.	.	0	0	0	1	0	0	0	0	17	.	916	11	2	.	.	2	1	1	0
14	7-Apr-00	99	.	1	2	.	.	0	0	0	0	0	0	0	0	3	.	331	4	0	.	.	2	1	1	0
15	14-Apr-00	106	.	1	2	.	32	0	0	0	0	1	3	0	0	17	.	29	5	4	.	.	2	1	1	0
16	21-Apr-00	113	.	1	2	.	2	0	0	0	1	0	0	0	0	56	.	27	10	0	.	.	2	1	1	0
17	28-Apr-00	120	.	1	2	.	5	1	0	1	1	0	0	0	0	238	.	480	60	14	.	.	2	1	1	0
18	5-May-00	127	.	-1	.	1	.	1	0	1	1	0	0	0	0	417	.	223	33	1	.	.	2	1	1	0
19	12-May-00	134	.	1	2	.	2	1	0	0	0	0	0	0	0	589	.	572	21	2	.	.	2	1	1	0
20	19-May-00	141	.	1	2	.	56	1	0	1	1	0	0	0	0	557	.	45	12	0	.	.	2	1	1	0
21	26-May-00	148	.	1	2	.	34	0	0	0	0	0	0	0	0	131	.	54	2	3	.	.	2	1	1	0
22	2-Jun-00	155	.	0	.	.	.	1	0	1	1	0	0	0	0	243	.	172	78	1	.	.	2	1	1	0
23	9-Jun-00	162	.	1	2	.	.	1	0	1	2	0	0	0	0	326	.	49	76	1	.	.	2	1	1	0
24	16-Jun-00	169	.	1	2	.	.	1	0	2	0	0	0	0	0	147	.	11	77	1	.	.	1	0	0	0
25	23-Jun-00	176	.	1	3	.	2	1	0	0	0	0	0	0	0	315	.	4	157	4	.	.	1	0	0	0
26	30-Jun-00	183	.	1	.	2	.	0	0	0	0	0	0	1	0	264	.	47	114	1	.	.	2	1	1	0
27	7-Jul-00	190	.	1	2	.	5	0	0	0	1	0	0	0	0	131	.	103	68	5	.	.	2	1	1	0
28	14-Jul-00	197	.	1	2	.	34	1	0	0	0	0	0	0	0	189	.	24	15	4	.	.	2	0	1	0
29	21-Jul-00	204	.	1	2	.	.	1	0	13	0	0	0	0	0	217	.	45	17	5	.	.	2	1	1	0
30	28-Jul-00	211	.	1	2	.	.	1	0	13	1	0	0	0	0	220	.	44	14	2	.	.	2	1	1	0
31	4-Aug-00	218	.	1	3	.	3	1	0	1	1	0	0	0	1	296	.	24	42	2	.	.	2	0	1	0
32	11-Aug-00	225	.	1	2	.	3	0	0	0	1	0	0	0	0	257	.	41	119	19	.	.	2	1	1	0
33	18-Aug-00	232	.	1	2	.	23	0	0	0	1	0	0	0	1	277	.	39	63	4	280	280	2	1	1	1
34	25-Aug-00	239	.	0	.	.	23	0	0	0	1	0	0	0	0	390	.	71	55	1	1460	2240	2	1	1	0
35	1-Sep-00	246	.	0	.	.	23	0	0	0	1	0	0	0	0	872	.	106	110	43	1390	2570	2	1	1	0



## Appendix 1 - Database

row	date	days	aster	dgrowth	dsize	dpat	directio	pyrsize	pyrsource	dir2	ash	expl2	expl	fume	glow	rkfl	lonrk	hy	loneq	teceq	min	max	nhy	hy2	hy3	mud
36	8-Sep-00	253	.	1	2	.	.	1	2	.	1	1	1	0	1	411	.	21	44	7	541	890	2	0	1	0
37	15-Sep-00	260	.	1	2	.	.	1	2	1	1	1	2	0	1	386	.	50	50	5	446	630	2	1	1	0
38	22-Sep-00	267	.	1	.	1	2	0	0	0	1	1	2	0	1	665	.	28	66	0	369	369	2	1	1	0
39	29-Sep-00	274	.	1	.	1	24	1	0	1	1	0	0	0	1	169	.	29	25	16	790	948	2	1	1	0
40	6-Oct-00	281	.	1	.	1	2	1	0	1	1	1	2	0	1	517	.	66	87	10	619	953	2	1	1	0
41	13-Oct-00	288	.	1	.	1	124	0	0	0	1	0	0	0	1	683	.	58	126	7	516	803	2	1	1	0
42	20-Oct-00	295	.	1	.	1	124	0	0	0	1	0	0	0	1	214	.	9	35	4	235	2252	1	0	0	0
43	27-Oct-00	302	1	1	.	1	124	0	0	0	1	0	0	0	1	146	.	20	19	3	.	.	2	0	0	0
44	3-Nov-00	309	.	1	.	1	2	1	3	1	1	0	0	0	1	252	.	9	11	3	.	.	1	0	0	1
45	10-Nov-00	316	.	1	.	1	2	1	0	345	1	0	0	0	0	207	.	33	144	7	.	.	2	1	1	0
46	17-Nov-00	323	.	-1	.	1	.	1	0	134	1	0	0	0	0	497	.	16	85	1	1050	1050	2	0	0	0
47	24-Nov-00	330	.	1	.	1	.	0	0	0	0	0	0	0	1	491	.	13	69	0	1020	1020	1	0	0	0
48	1-Dec-00	337	.	-1	.	1	2	1	0	4	0	0	0	0	0	547	.	15	72	1	.	.	2	0	0	0
49	8-Dec-00	344	.	1	.	1	23	0	0	0	1	0	0	0	0	494	.	7	84	0	340	430	1	0	0	0
50	15-Dec-00	351	.	1	2	.	2	0	0	0	1	0	0	0	0	423	.	12	74	1	400	400	1	0	0	0
51	22-Dec-00	358	1	1	.	1	.	0	0	0	1	0	0	0	0	708	.	10	53	2	745	1100	1	0	0	0
52	29-Dec-00	365	.	1	.	1	.	0	0	0	0	0	0	0	1	717	.	3	92	5	.	.	1	0	0	0
53	5-Jan-01	372	.	1	2	.	.	0	0	0	0	0	0	0	1	1076	.	3	74	3	400	700	1	0	0	0
54	12-Jan-01	379	1	1	2	.	6	1	0	4	0	0	0	0	0	943	.	0	54	0	345	345	1	0	0	0
55	19-Jan-01	386	.	1	2	.	6	0	0	0	0	0	0	0	0	417	.	1	82	0	330	350	1	0	0	0
56	26-Jan-01	393	.	1	1	.	6	1	0	3	1	0	0	0	0	313	32	8	45	21	105	360	1	0	0	0
57	2-Feb-01	400	.	1	.	1	2	1	0	4	0	0	0	0	0	409	26	5	40	1	180	500	1	0	0	0
58	9-Feb-01	407	.	1	.	2	2	1	0	134	0	0	0	0	0	500	100	2	15	1	80	670	1	0	0	0
59	16-Feb-01	414	.	1	.	1	3	1	0	13	0	0	0	0	0	486	18	18	53	6	240	720	2	0	0	0
60	23-Feb-01	421	.	-1	2	.	3	1	0	34	1	0	0	0	0	729	34	388	58	3	180	1400	2	1	1	0
61	2-Mar-01	428	.	1	2	.	3	0	0	0	1	0	0	0	0	629	22	280	45	4	100	1230	2	1	1	0
62	9-Mar-01	435	.	1	2	.	.	0	0	0	0	0	0	0	0	294	16	4	23	0	130	460	1	0	0	0
63	16-Mar-01	442	.	1	1	.	3	0	0	0	0	0	0	0	0	84	8	5	8	2	120	190	1	0	0	0
64	23-Mar-01	449	.	1	1	.	3	0	0	0	0	0	0	0	0	33	2	5	1	3	200	275	1	0	0	0
65	30-Mar-01	456	.	1	1	.	3	0	0	0	0	0	0	0	0	62	1	18	1	1	50	370	2	0	0	0
66	6-Apr-01	463	.	1	1	.	3	0	0	0	0	0	0	0	0	52	1	9	3	6	40	520	1	0	0	0
67	13-Apr-01	470	.	1	1	.	3	0	0	0	1	0	0	0	0	54	2	48	9	1	20	70	2	1	1	0
68	20-Apr-01	477	.	1	1	.	3	0	0	0	1	0	0	0	0	31	2	10	2	1	100	250	1	0	0	0
69	27-Apr-01	484	.	1	1	.	3	0	0	0	1	0	0	0	0	98	5	10	7	3	130	220	1	0	0	0
70	4-May-01	491	.	1	1	.	3	1	0	3	0	0	0	0	0	104	5	34	22	6	80	180	2	1	1	0

## Appendix 1 - Database

row	date	days after	dgrowth	dsize	dpat	directio	pyrsize	pyrsrc	dir2	ash	expl2	expl	fume	glow	rkfl	lonrk	hy	loneq	teceq	min	max	nhy	hy2	hy3	mud
71	11-May-01	498	1	1	.	3	0	0	0	0	0	0	0	0	240	13	17	31	1	170	170	2	0	0	0
72	18-May-01	505	1	2	.	3	1	0	3	1	0	0	0	0	237	31	26	109	0	700	700	2	1	1	0
73	25-May-01	512	1	1	.	3	0	0	0	0	0	0	0	0	266	104	36	383	3	90	370	2	1	1	0
74	1-Jun-01	519	1	1	.	3	0	0	0	0	0	0	0	0	224	51	25	164	6	130	320	2	0	1	0
75	8-Jun-01	526	1	3	.	3	0	0	0	0	0	0	0	0	373	35	71	169	0	770	1410	2	1	1	0
76	15-Jun-01	533	1	2	.	3	0	0	0	0	0	0	0	0	462	43	11	77	1	460	630	1	0	0	0
77	22-Jun-01	540	1	2	.	3	0	0	0	0	0	0	0	0	299	19	1	26	0	860	860	1	0	0	0
78	29-Jun-01	547	1	2	.	3	2	0	6	0	0	0	0	0	295	10	4	28	1	120	120	1	0	0	0
79	6-Jul-01	554	1	2	.	3	0	0	0	0	0	0	0	0	297	14	7	38	0	347	347	1	0	0	0
80	13-Jul-01	561	1	2	.	3	1	0	12	1	0	0	0	0	719	25	5	57	2	709	943	1	0	0	0
81	20-Jul-01	568	1	2	.	3	1	0	1	1	0	0	1	0	706	28	8	30	1	339	854	1	0	0	0
82	27-Jul-01	575	-1	3	.	3	2	0	1	3	1	1	0	0	453	6	15	67	0	.	.	2	0	0	1
83	3-Aug-01	582	1	.	.	.	1	0	0	0	0	0	0	0	258	2	13	13	2	680	950	1	0	0	1
84	10-Aug-01	589	1	2	.	.	1	0	0	0	0	0	0	0	186	1	6	3	3	.	.	1	0	0	0
85	17-Aug-01	596	0	.	.	.	1	0	1	0	0	0	0	0	189	1	149	36	0	.	.	2	1	1	0
86	24-Aug-01	603	1	3	.	.	1	0	1	1	0	0	0	0	200	1	19	6	11	68	151	2	0	0	0
87	31-Aug-01	610	1	3	.	.	1	0	1	0	0	0	0	1	218	2	8	31	4	86	242	1	0	0	0
88	7-Sep-01	617	1	3	.	.	1	0	1	1	0	0	0	0	228	0	65	28	1	543	543	2	1	1	0
89	14-Sep-01	624	1	2	.	.	1	0	1	2	0	0	0	0	211	4	522	36	3	200	2000	2	1	1	0
90	21-Sep-01	631	1	2	.	.	1	0	1	1	0	0	0	0	297	7	326	16	12	100	600	2	1	1	0
91	28-Sep-01	638	1	2	.	.	1	2	1	1	0	0	0	0	202	2	451	26	0	418	418	2	1	1	1
92	5-Oct-01	645	1	2	.	.	1	2	13	1	0	0	0	0	285	7	20	34	1	388	388	2	0	0	1
93	12-Oct-01	652	-1	2	.	.	2	0	13	1	0	0	0	0	207	2	9	6	1	320	320	1	0	0	1
94	19-Oct-01	659	1	2	.	.	1	2	1	0	0	0	0	0	208	2	46	3	0	200	574	2	1	1	1
95	26-Oct-01	666	1	3	.	25	1	2	1	1	0	0	0	0	284	.	46	8	2	77	611	2	1	1	1
96	2-Nov-01	673	1	2	.	2	1	1	.	1	0	0	0	0	314	8	174	5	4	134	134	2	1	1	1
97	9-Nov-01	680	1	2	.	2	1	2	1	1	0	0	0	0	149	4	116	20	2	450	521	2	1	1	0
98	16-Nov-01	687	1	.	1	4	0	0	0	0	0	0	0	1	251	45	413	115	0	119	140	2	1	1	0
99	23-Nov-01	694	1	.	1	24	0	0	0	0	0	0	0	0	435	82	193	145	0	100	100	2	1	1	0
100	30-Nov-01	701	-1	2	.	2	2	0	13	0	0	0	0	0	363	37	128	58	0	.	.	2	1	1	0
101	7-Dec-01	708	0	.	.	.	0	0	0	1	0	0	0	0	551	97	80	95	0	158	158	2	1	1	0
102	14-Dec-01	715	0	.	.	234	1	0	13	1	0	0	0	0	858	42	25	57	0	.	.	2	0	1	1
103	21-Dec-01	722	1	2	.	2	0	0	0	0	0	0	0	1	1012	45	75	75	0	.	.	2	1	1	0
104	28-Dec-01	729	-1	2	.	2	1	0	1	1	0	0	0	0	911	69	21	103	0	250	1000	2	0	1	0
105	4-Jan-02	736	1	.	1	2	1	0	1	1	0	0	0	1	939	81	24	87	0	898	1122	2	0	1	0

## Appendix 1 - Database

row	date	days	aster	dgrowth	dsize	dpat	directio	pyrsize	pyrsource	dir2	ash	expl2	expl	fume	glow	rfl	lonrk	hy	loneq	teceq	min	max	nhy	hy2	hy3	mud
106	11-Jan-02	743	.	1	2	.	2	1	0	1	1	0	0	0	0	741	29	7	52	0	.	.	1	0	0	1
107	18-Jan-02	750	.	1	.	1	2	1	0	0	0	0	0	0	0	471	68	9	70	0	700	700	1	0	0	0
108	25-Jan-02	757	.	1	2	.	2	1	0	1	1	0	0	0	0	610	67	8	140	0	.	.	1	0	0	0
109	1-Feb-02	764	.	1	.	1	25	2	0	13	0	0	0	0	0	897	64	16	85	0	160	790	2	0	0	0
110	8-Feb-02	771	.	1	2	.	25	1	0	1	1	0	0	0	0	734	69	17	83	1	150	650	2	0	0	0
111	15-Feb-02	778	.	1	.	1	26	1	0	4	1	0	0	0	1	786	75	17	74	0	90	780	2	0	0	0
112	22-Feb-02	785	.	1	.	1	2	1	0	1	1	0	0	0	1	1013	124	5	101	0	.	.	1	0	0	0
113	1-Mar-02	792	.	1	.	1	2	1	2	1	1	0	0	0	1	415	49	10	56	0	60	130	1	0	0	0
114	8-Mar-02	799	.	1	.	1	.	1	2	1	1	0	0	0	1	779	67	6	92	0	430	860	1	0	0	0
115	15-Mar-02	806	.	1	.	1	2	1	2	1	1	0	0	0	0	1002	108	3	162	2	395	1035	1	0	0	0
116	22-Mar-02	813	.	1	2	.	2	1	2	.	1	0	0	0	0	935	80	3	123	0	1100	1200	1	0	0	0
117	29-Mar-02	820	.	1	2	.	256	1	0	1	1	0	0	0	0	968	15	6	44	0	558	963	1	0	0	0
118	5-Apr-02	827	.	1	.	2	6	0	0	0	0	0	0	0	0	1120	56	6	85	10	1150	1150	1	0	0	0
119	12-Apr-02	834	1	1	.	1	6	0	0	0	0	0	0	0	0	841	52	6	65	0	1200	1200	1	0	0	0
120	19-Apr-02	841	.	1	2	.	26	1	0	17	0	0	0	0	0	990	66	31	114	1	1200	1200	2	1	1	0
121	26-Apr-02	848	.	1	.	2	2	1	2	1	0	0	0	0	0	741	33	42	76	2	600	600	2	1	1	0
122	3-May-02	855	.	1	2	.	2	1	2	.	0	0	0	0	1	557	40	13	82	0	.	.	1	0	0	0
123	10-May-02	862	.	0	.	.	25	1	2	1	0	0	0	0	0	532	99	5	127	0	.	.	1	0	0	0
124	17-May-02	869	.	0	.	.	2	1	2	1	0	0	0	0	0	532	111	1	77	0	.	.	1	0	0	0
125	24-May-02	876	.	1	2	.	6	1	2	.	0	0	0	0	0	497	93	6	57	0	.	.	1	0	0	0
126	31-May-02	883	.	1	.	1	246	0	0	0	0	0	0	0	0	129	4	6	20	4	.	.	1	0	0	0
127	7-Jun-02	890	.	1	.	1	6	0	0	0	0	0	0	0	0	135	3	12	20	0	247	955	1	0	0	0
128	14-Jun-02	897	.	1	.	1	6	1	0	4	0	0	0	0	0	226	10	17	14	0	90	720	2	0	0	0
129	21-Jun-02	904	.	1	.	2	6	0	0	0	0	0	0	0	0	102	2	19	6	0	90	540	2	0	0	0
130	28-Jun-02	911	.	0	.	.	.	0	0	0	0	0	0	0	0	42	5	11	6	0	90	260	1	0	0	1
131	5-Jul-02	918	.	0	.	.	.	0	0	0	0	0	0	0	0	108	2	17	6	0	90	260	2	0	0	0
132	12-Jul-02	925	.	1	1	2	6	1	0	1	0	0	0	0	0	151	4	8	3	0	80	225	1	0	0	0
133	19-Jul-02	932	.	1	3	2	12	2	1	134	0	0	0	0	0	250	28	15	92	0	175	250	2	1	1	0
134	26-Jul-02	939	.	1	3	2	1	1	1	34	0	0	0	0	0	260	32	3	118	0	90	270	1	0	0	1
135	2-Aug-02	946	1	1	3	2	1	1	1	5	0	0	0	0	0	313	52	23	138	0	380	690	2	0	1	0
136	9-Aug-02	953	.	1	3	2	1	1	1	345	0	0	0	0	0	209	8	5	87	9	86	720	1	0	0	0
137	16-Aug-02	960	.	1	2	.	1	0	0	0	0	0	0	0	0	231	5	1	44	0	170	600	1	0	0	0
138	23-Aug-02	967	.	1	2	.	1	1	.	1	0	0	0	0	0	287	9	0	31	0	170	340	1	0	0	0
139	30-Aug-02	974	.	1	2	.	1	1	0	14	0	0	0	0	0	453	9	1	63	0	170	432	1	0	0	0
140	6-Sep-02	981	.	1	2	.	2	1	0	14	0	0	0	0	0	308	2	0	63	0	42	518	1	0	0	0

## Appendix 1 - Database

row	date	days	aster	dgrowth	dsize	dpat	directio	pyrsize	pyrsource	dir2	ash	expl2	expl	fume	glow	rfl	lonrk	hy	lonrk	teceq	min	max	nhy	hy2	hy3	mud
141	13-Sep-02	988	.	1	2	2	12	1	1	14	0	0	0	0	0	689	41	67	162	1	85	518	2	1	1	0
142	20-Sep-02	995	.	1	2	1	124	1	2	2	0	0	0	0	1	680	55	36	260	24	.	.	2	1	1	0
143	27-Sep-02	1002	.	1	.	2	124	2	0	34	3	0	0	0	0	811	51	15	223	2	.	.	2	0	0	1
144	4-Oct-02	1009	.	1	2	2	8	1	0	4	0	0	0	0	0	468	42	3	77	3	43	691	1	0	0	1
145	11-Oct-02	1016	.	1	.	2	1	1	0	18	0	0	0	0	0	650	80	2	98	1	43	860	1	0	0	0
146	18-Oct-02	1023	.	1	.	2	8	1	0	134	0	0	0	0	0	536	27	6	120	1	85	1000	1	0	0	1
147	25-Oct-02	1030	1	1	.	2	8	2	0	14	0	0	0	0	0	670	72	9	148	1	25	520	1	0	0	0
148	1-Nov-02	1037	.	1	.	2	1	1	0	0	0	0	0	0	0	694	38	3	60	0	200	508	1	0	0	0
149	8-Nov-02	1044	.	1	1	.	8	2	0	145	0	0	0	0	0	409	8	1	29	0	520	560	1	0	0	0
150	15-Nov-02	1051	.	.	.	.	.	1	0	134	0	0	0	0	0	592	37	2	88	1	160	380	1	0	0	0
151	22-Nov-02	1058	.	1	1	.	1	1	0	134	0	0	0	0	0	586	32	0	44	0	170	1040	1	0	0	0
152	29-Nov-02	1065	.	1	2	.	1	1	0	134	0	0	0	0	0	354	43	0	33	0	400	400	1	0	0	0
153	6-Dec-02	1072	.	-1	.	1	5	2	0	134	2	0	0	0	0	427	30	6	47	0	280	3600	1	0	0	1
154	13-Dec-02	1079	.	1	3	.	5	2	0	134	0	0	0	0	1	742	50	2	50	0	.	.	1	0	0	0
155	20-Dec-02	1086	.	1	.	1	5	2	0	134	0	0	0	0	1	760	30	5	45	0	.	.	1	0	0	0
156	27-Dec-02	1093	.	1	.	1	5	3	4	134	0	0	0	0	0	863	41	3	86	1	.	.	1	0	0	0
157	3-Jan-03	1100	.	1	2	.	5	2	0	134	0	0	0	0	0	789	54	0	120	0	130	430	1	0	0	0
158	10-Jan-03	1107	.	1	2	.	5	1	0	134	0	0	0	0	0	606	42	7	67	2	90	1260	1	0	0	0
159	17-Jan-03	1114	.	1	2	.	5	1	0	134	0	0	0	0	0	566	24	0	58	1	90	900	1	0	0	0
160	24-Jan-03	1121	.	1	2	.	5	2	0	134	0	0	0	0	0	745	62	2	177	1	480	648	1	0	0	0
161	31-Jan-03	1128	.	-1	.	.	5	1	0	134	0	0	0	0	0	882	114	6	148	0	90	170	1	0	0	0
162	7-Feb-03	1135	.	1	2	.	5	2	0	134	0	0	0	0	0	840	78	3	117	1	.	.	1	0	0	0
163	14-Feb-03	1142	.	1	2	.	5	2	0	14	0	0	0	0	0	905	80	8	87	1	170	350	1	0	0	0
164	21-Feb-03	1149	.	1	2	.	5	2	0	14	0	0	0	0	0	1078	85	1	92	0	400	1120	1	0	0	0
165	28-Feb-03	1156	.	1	2	.	5	3	2	4	0	0	0	0	0	997	71	0	79	4	500	1020	1	0	0	0
166	7-Mar-03	1163	.	1	2	.	0	1	0	124	1	0	0	0	1	1050	108	5	87	0	220	355	1	0	0	0
167	14-Mar-03	1170	.	1	2	1	0	1	1	1345	1	0	0	0	0	1050	152	2	93	2	285	380	1	0	0	0
168	28-Mar-03	1184	.	1	.	3	26	1	0	1345	0	0	0	0	0	754	101	7	74	2	230	770	1	0	0	0
169	4-Apr-03	1191	.	1	2	.	0	1	0	134	0	0	0	0	0	332	77	1	66	0	151	780	1	0	0	1
170	11-Apr-03	1198	.	1	2	2	26	1	0	15	0	0	0	0	0	393	56	7	72	0	220	550	1	0	0	0

## Appendix 2 - Database Variable Explanation

	variable	explanation of variable	value	label	original data
1	date	date- first day of reporting week	day/month/year	N/A	quantitative
2	days	days- number of days of study	none	N/A	N/A
3	aster	ASTER image capture during week	0	no	quantitative
			1	yes	
4	dgrowth	growth or collapse of the dome	-1	collapse	categorical
			0	no	
			1	growth	
5	dsize	amount of dome growth or extrusion	1	small	categorical
			2	moderate	
			3	high	
6	dpattern	characteristics of dome growth	1	spines	categorical
	dpat		2	lobes/slabs	
7	directio	prominent direction of dome growth	1	N	categorical
		using azimuthal direction	2	E	
			3	S	
			4	W	
			5	NE-SE	
			6	SE	
			7	SW	
			8	NW	
			12	NE	
			23	E-S	
			24	E-W	
			25	E-NE	
			26	E-SE	
			32	S-E	
			34	S-W	
			56	NE-SE	
			124	N-E-W	
			234	E-S-W	
			246	E-W-SE	
			256	E-NE-SE	
8	pyrsize	size or duration of pyroclastic flows	0	no	categorical
			1	small(light)	
			2	moderate(steady)	
			3	intense	
9	pyrsourc	source of pyroclastic flow	1	from dome	categorical
			2	from rockfall	
			3	from rain	

## Appendix 2 - Database Variable Explanation

10	dir2	direction of pyroclastic flow	0	no	categorical
			1	(TRV)Tar River Valley	
			2	(G) Gages	
			3	(W) White	
			4	(T) Tuitt	
			5	(Ty) Tyre	
			6	(A) Amersham	
			7	(D) Dry	
			8	(FG) Fort Ghaut	
			12	TRV-G	
			13	TRV-W	
			14	TRV-T	
(10)	(dir2)	(direction of pyroclastic flow)	15	TRY-Ty	(categorical)
			17	TRV-D	
			18	TRV-FG	
			34	W-T	
			124	TRV-G-T	
			134	TRV-W-T	
			145	TRV-T-Ty	
			345	W-T-Ty	
			1345	TRV-W-T-Ty	
11	ash	ash fall	0	no	both
			1	light <10,000 ft	
			2	medium >10,000-20,000 ft	
			3	heavy >20,000	
12	expl2	explosive behavior / explosions	0	no	categorical
			1	yes	
13	expl	explosive behavior / explosions	0	no	categorical
			1	small / magmatic	
			2	small but several	
			3	vulcanian	
14	fume	fumarolic activity	0	no	categorical
			1	yes / steaming	
			2	vigorous	
15	glow	observed incandescence	0	no	categorical
			1	yes	
16	rkfl	total weekly rockfall events	total value	N/A	quantitative
17	lonrk	total weekly long rockfall events	total value	N/A	quantitative
18	hy	total weekly hybrid eq. events	total value	N/A	quantitative
19	loneq	total weekly long eq. Events	total value	N/A	quantitative

## Appendix 2 – Database Variable Explanation

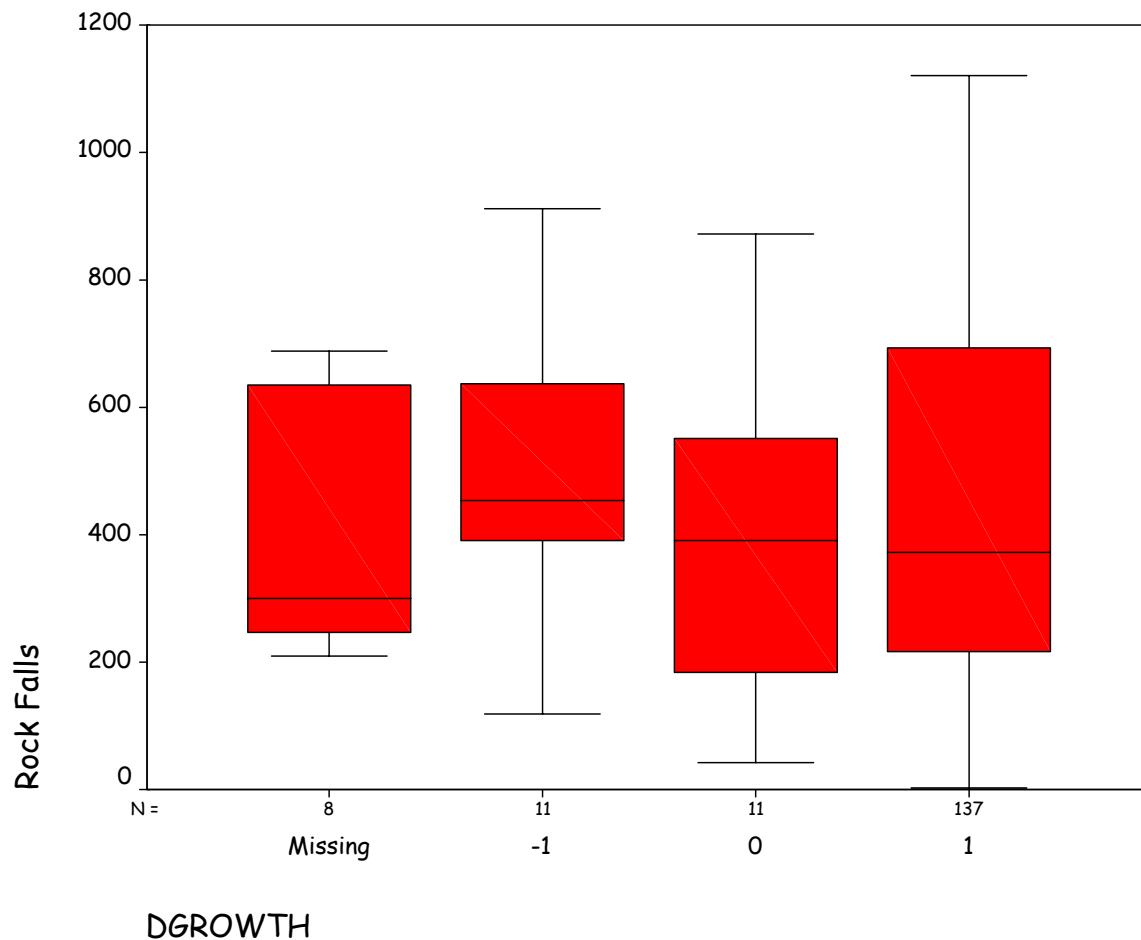
20	teceq	total weekly tectonic eq. Events	total value	N/A	quantitative
21	min	minimum SO2 for week	tonnes / day	N/A	quantitative
22	max	maximum SO2 for week	tonnes / day	N/A	quantitative
23	nhy	total weekly hybrid eq. events	1	14 events and below	categorical
			2	above 14 events	
24	hy2	total weekly hybrid eq. events	0	25 events and below	categorical
			1	above 25 events	
25	hy3	total weekly hybrid eq. events	0	20 events and below	categorical
			1	above 21 events	
26	mud	lahars	0	no	categorical
			1	yes	

## Appendix 3 – Statistical Analysis of Selected Variables from Database

### DGROWTH and RKFL

Case Processing Summary

		Cases					
		Valid		Missing		Total	
DGROWTH		N	Percent	N	Percent	N	Percent
RKFL	. (Missing)	8	88.9%	1	11.1%	9	100.0%
	-1	11	100.0%	0	.0%	11	100.0%
	0	11	84.6%	2	15.4%	13	100.0%
	1	137	100.0%	0	.0%	137	100.0%

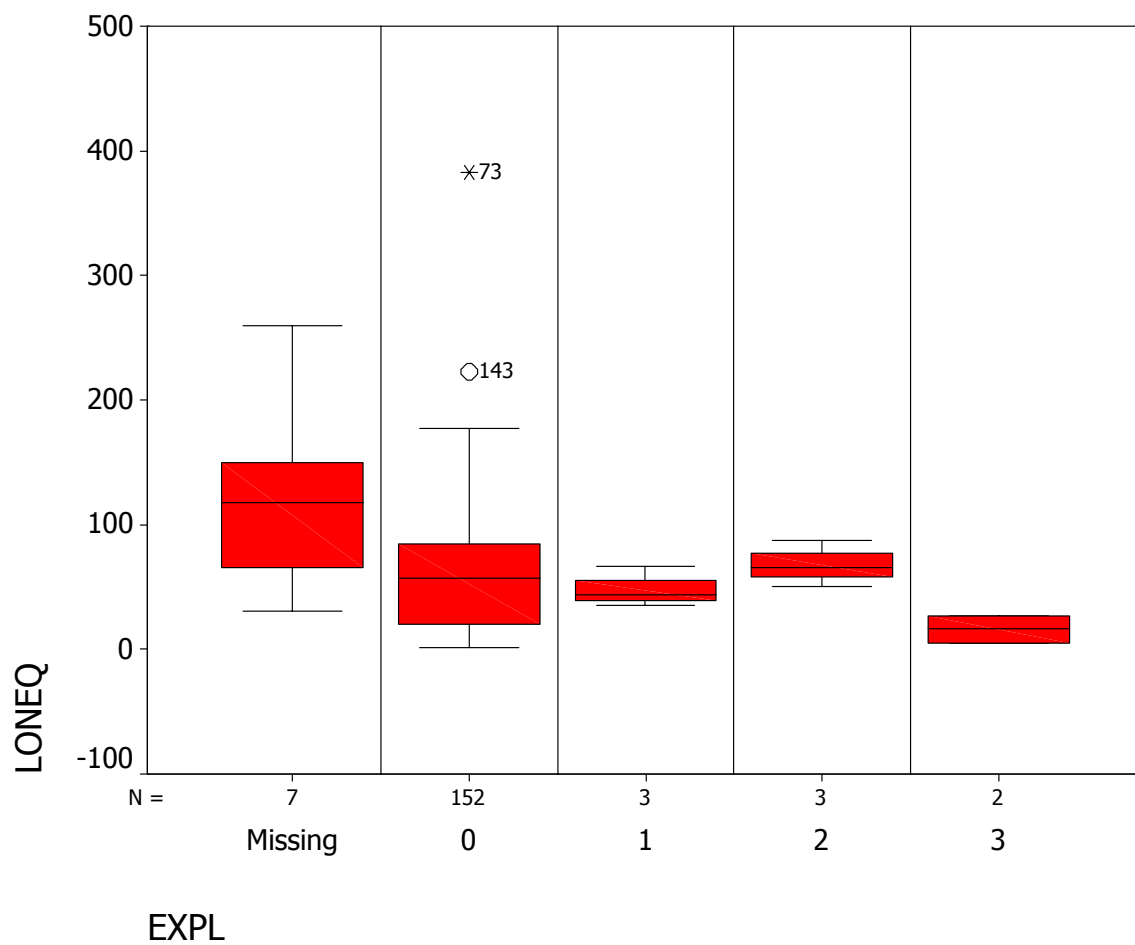




## EXPL and LONEQ

Case Processing Summary

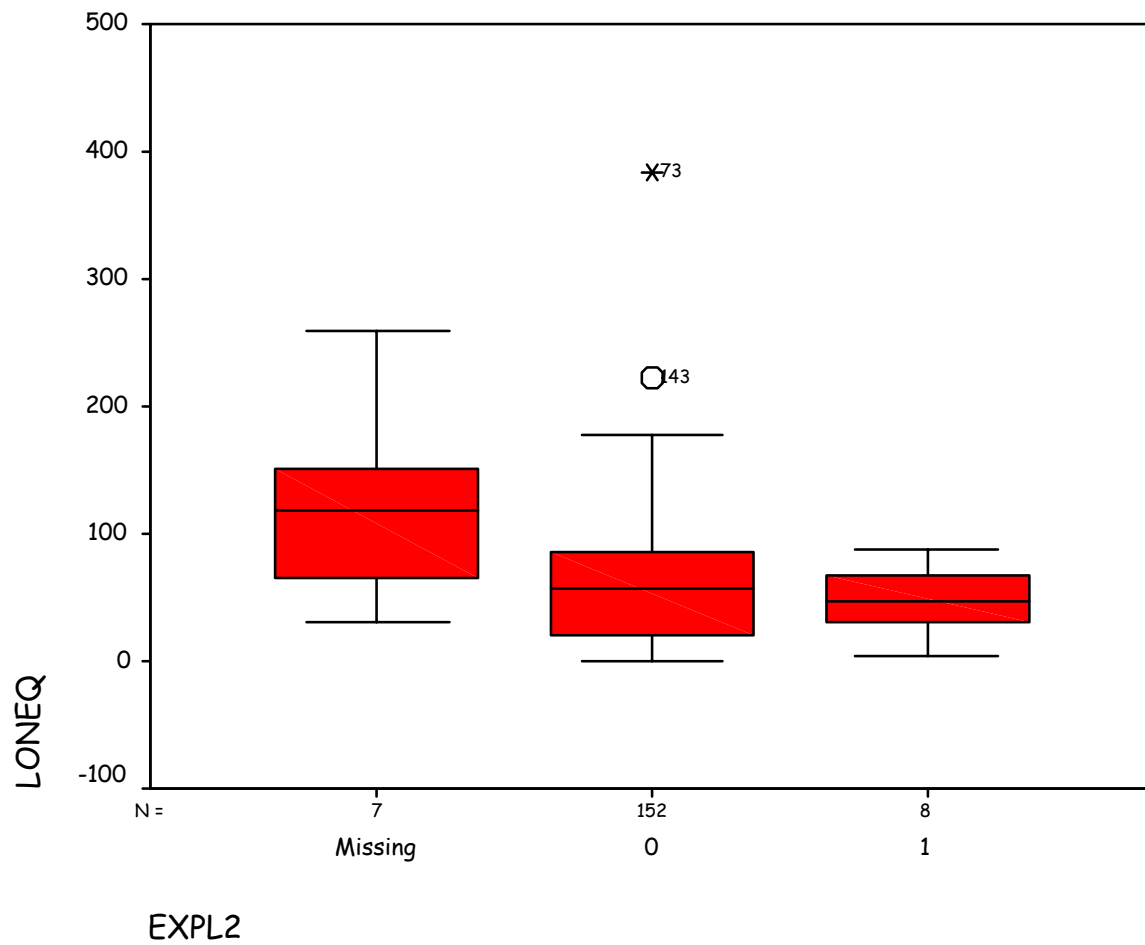
EXPL	Cases					
	Valid		Missing		Total	
	N	Percent	N	Percent	N	Percent
LONEQ . (Missing)	7	87.5%	1	12.5%	8	100.0%
0	152	98.7%	2	1.3%	154	100.0%
1	3	100.0%	0	.0%	3	100.0%
2	3	100.0%	0	.0%	3	100.0%
3	2	100.0%	0	.0%	2	100.0%



## EXPL2 and LONEQ

Case Processing Summary

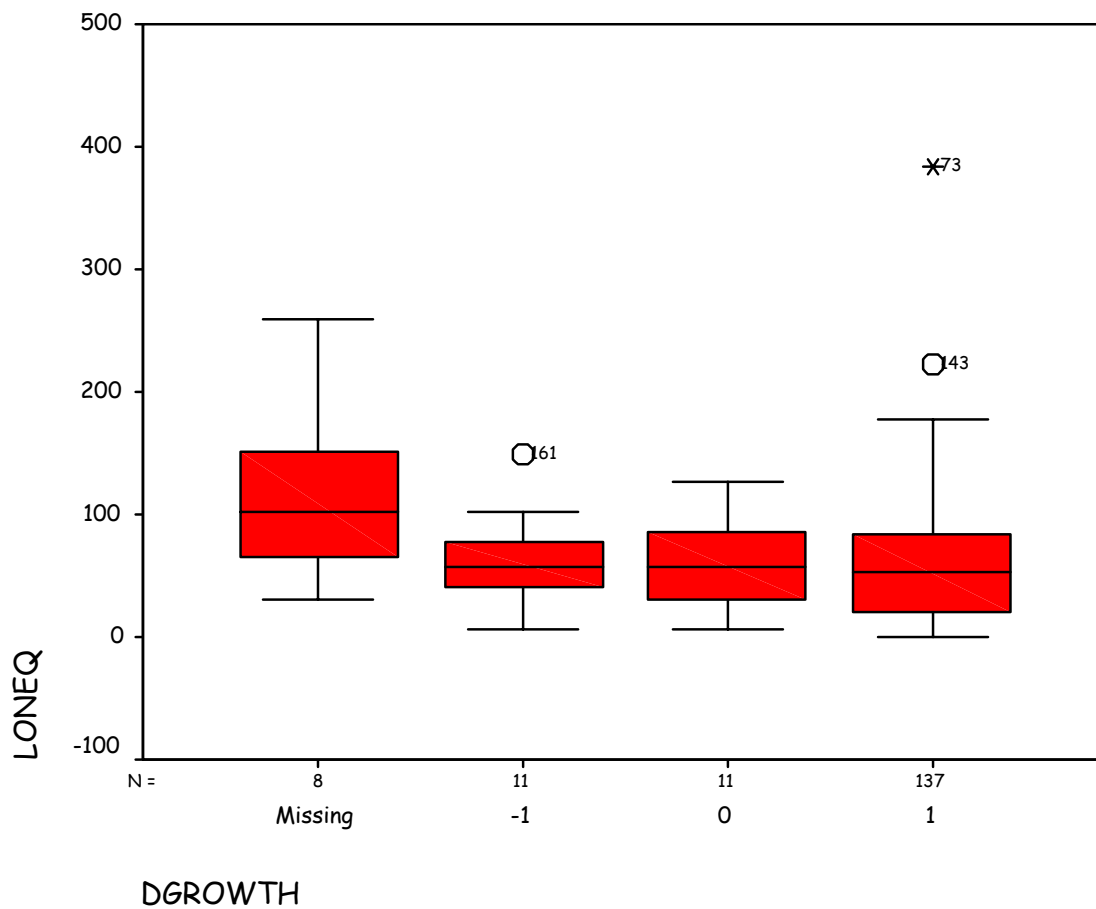
	EXPL2	Cases					
		Valid		Missing		Total	
		N	Percent	N	Percent	N	Percent
LONEQ	. (Missing)	7	87.5%	1	12.5%	8	100.0%
	0	152	98.7%	2	1.3%	154	100.0%
	1	8	100.0%	0	.0%	8	100.0%



## DGROWTH and LONEQ

Case Processing Summary

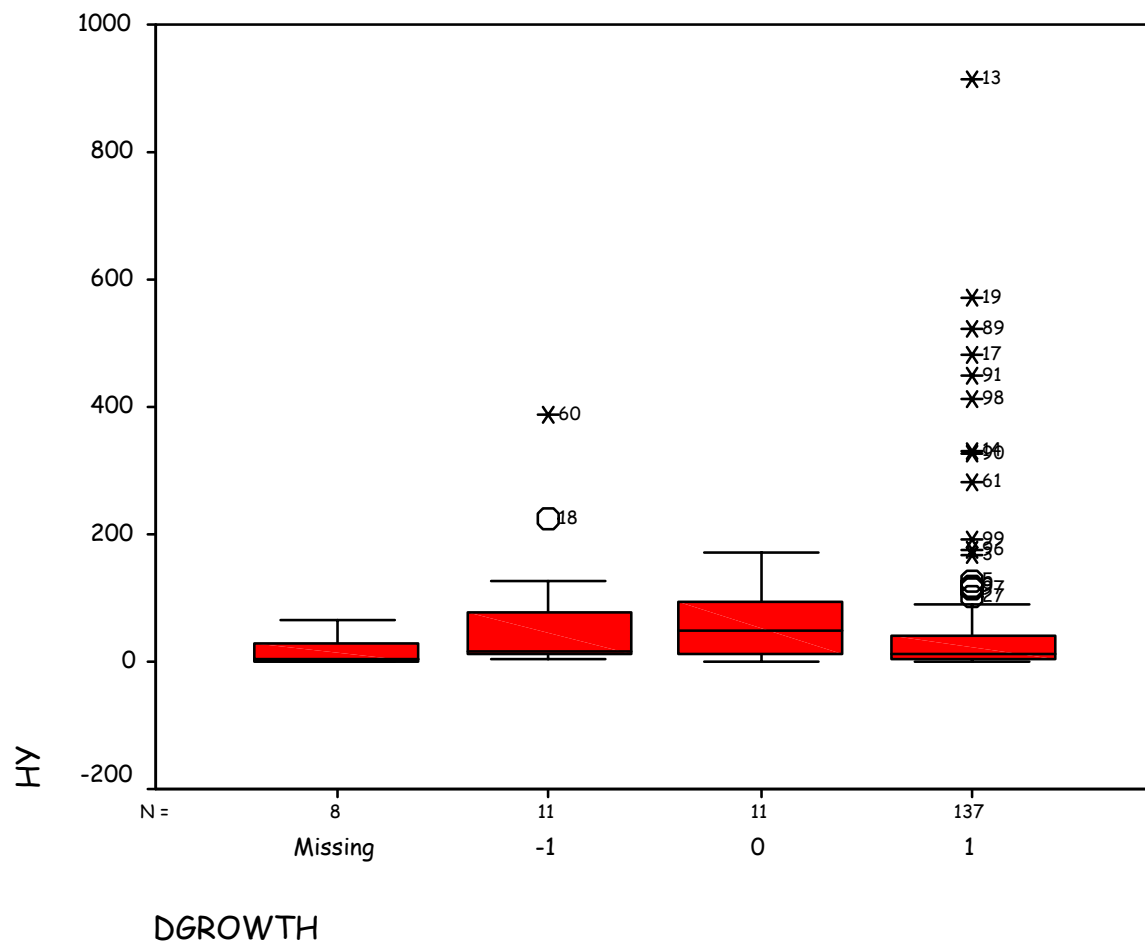
		Cases					
		Valid		Missing		Total	
		N	Percent	N	Percent	N	Percent
LONEQ	.	8	88.9%	1	11.1%	9	100.0%
	-1	11	100.0%	0	.0%	11	100.0%
	0	11	84.6%	2	15.4%	13	100.0%
	1	137	100.0%	0	.0%	137	100.0%



## DGROWTH and HY

Case Processing Summary

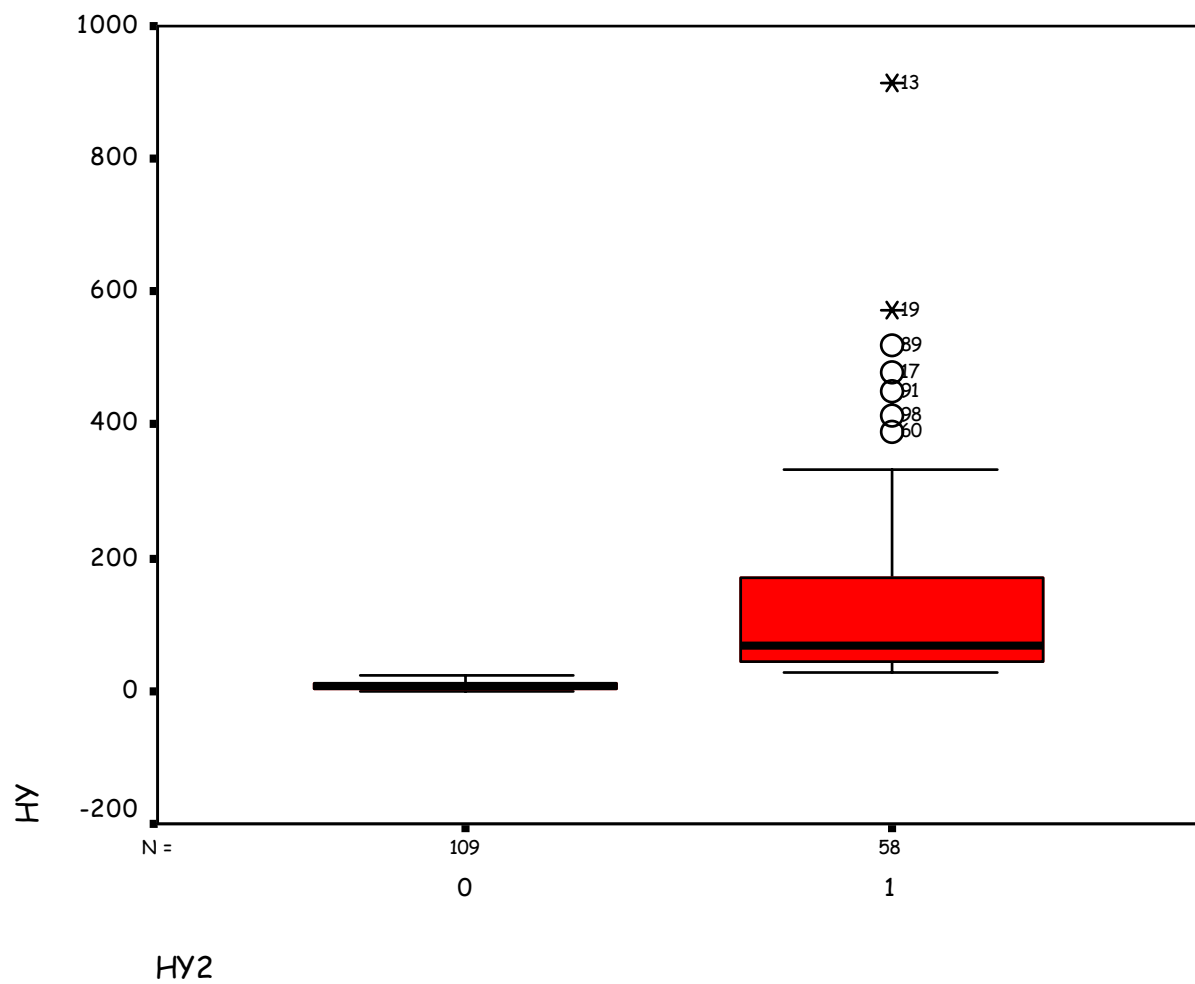
DGROWTH		Cases					
		Valid		Missing		Total	
		N	Percent	N	Percent	N	Percent
HY	.(Missing)	8	88.9%	1	11.1%	9	100.0%
	-1	11	100.0%	0	.0%	11	100.0%
	0	11	84.6%	2	15.4%	13	100.0%
	1	137	100.0%	0	.0%	137	100.0%



## HY2 and HY

Case Processing Summary

		Cases					
		Valid		Missing		Total	
	HY2	N	Percent	N	Percent	N	Percent
HY	0	109	100.0%	0	.0%	109	100.0%
	1	58	95.1%	3	4.9%	61	100.0%



## NPar Tests

### Chi-Square Test

### Frequencies

#### EXPL2

	Observed N	Expected N	Residual
0	154	81.0	73.0
1	8	81.0	-73.0
Total	162		

#### NTILES of HY

	Observed N	Expected N	Residual
1	83	83.5	-.5
2	84	83.5	.5
Total	167		

### Test Statistics

	EXPL2	NTILES of HY
Chi-Square <sup>a,b</sup>	131.580	.006
df	1	1
Asymp. Sig.	.000	.938

a. 0 cells (.0%) have expected frequencies less than 5. The minimum expected cell frequency is 81.0.

b. 0 cells (.0%) have expected frequencies less than 5. The minimum expected cell frequency is 83.5.

### Tables

0	0
1	0

### Crosstabs

#### Case Processing Summary

	Cases					
	Valid		Missing		Total	
	N	Percent	N	Percent	N	Percent
EXPL2 * HY2	162	95.3%	8	4.7%	170	100.0%

#### EXPL2 \* HY2 Crosstabulation

Count		HY2		Total
		0	1	
		102	52	154
EXPL2	0			
	1	2	6	8
Total		104	58	162

### Chi-Square Tests

	Value	df	Asymp. Sig. (2-sided)	Exact Sig. (2-sided)	Exact Sig. (1-sided)
Pearson Chi-Square	5.626 <sup>b</sup>	1	.018		
Continuity Correction <sup>a</sup>	3.975	1	.046		
Likelihood Ratio	5.382	1	.020		
Fisher's Exact Test				.025	.025
N of Valid Cases	162				

a. Computed only for a 2x2 table

b. 1 cells (25.0%) have expected count less than 5. The minimum expected count is 2.86.

## Crosstabs

### Case Processing Summary

	Cases					
	Valid		Missing		Total	
	N	Percent	N	Percent	N	Percent
EXPL2 * HY2	162	95.3%	8	4.7%	170	100.0%

### EXPL2 \* HY2 Crosstabulation

		HY2		Total
		0	1	
EXPL2 0	Count	102	52	154
	Expected Count	98.9	55.1	154.0
1	Count	2	6	8
	Expected Count	5.1	2.9	8.0
Total	Count	104	58	162
	Expected Count	104.0	58.0	162.0

### Chi-Square Tests

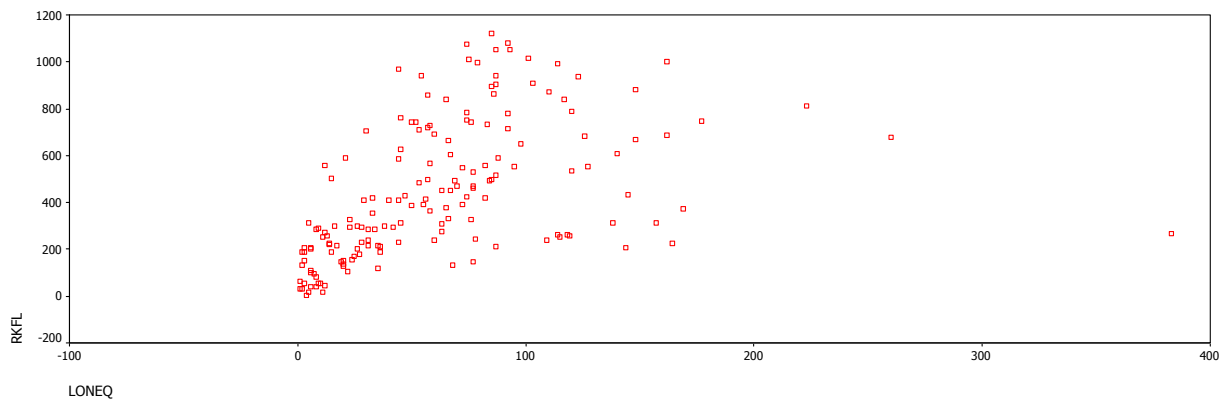
	Value	df	Asymp. Sig. (2-sided)	Exact Sig. (2-sided)	Exact Sig. (1-sided)
Pearson Chi-Square	5.626 <sup>b</sup>	1	.018	.025	.025
Continuity Correction <sup>a</sup>	3.975	1	.046		
Likelihood Ratio	5.382	1	.020	.051	.025
Fisher's Exact Test				.025	.025
N of Valid Cases	162				

a. Computed only for a 2x2 table

b. 1 cells (25.0%) have expected count less than 5. The minimum expected count is 2.86.



# Graph



# Regression

**Variables Entered/Removed<sup>a</sup>**

Model	Variables Entered	Variables Removed	Method
1	RKFL <sup>a</sup>	.	Enter

a. All requested variables entered.

b. Dependent Variable: LONEQ

**Model Summary<sup>b</sup>**

Model	R	R Square	Adjusted R Square	Std. Error of the Estimate
1	.459 <sup>a</sup>	.210	.206	47.757

a. Predictors: (Constant), RKFL

b. Dependent Variable: LONEQ

**ANOVA<sup>b</sup>**

Model		Sum of Squares	df	Mean Square	F	Sig.
1	Regression	100325.0	1	100324.969	43.988	.000 <sup>a</sup>
	Residual	376325.0	165	2280.758		
	Total	476650.0	166			

a. Predictors: (Constant), RKFL

b. Dependent Variable: LONEQ

**Coefficients<sup>a</sup>**

Model		Unstandardized Coefficients		Standardized Coefficients	t	Sig.
		B	Std. Error	Beta		
1	(Constant)	25.294	6.791		3.725	.000
	RKFL	8.484E-02	.013	.459	6.632	.000

a. Dependent Variable: LONEQ

**Casewise Diagnostics<sup>a</sup>**

Case Number	Std. Residual	LONEQ
73	7.018	383
142	3.707	260

a. Dependent Variable: LONEQ

**Residuals Statistics<sup>a</sup>**

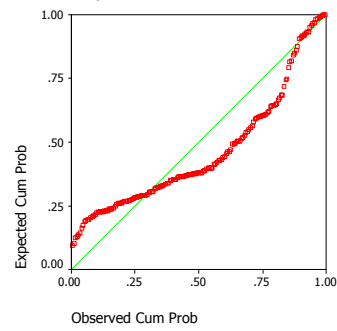
	Minimum	Maximum	Mean	Std. Deviation	N
Predicted Value	25.55	120.31	63.08	24.584	167
Residual	-63.42	335.14	.00	47.613	167
Std. Predicted Value	-1.527	2.328	.000	1.000	167
Std. Residual	-1.328	7.018	.000	.997	167

a. Dependent Variable: LONEQ

# Charts

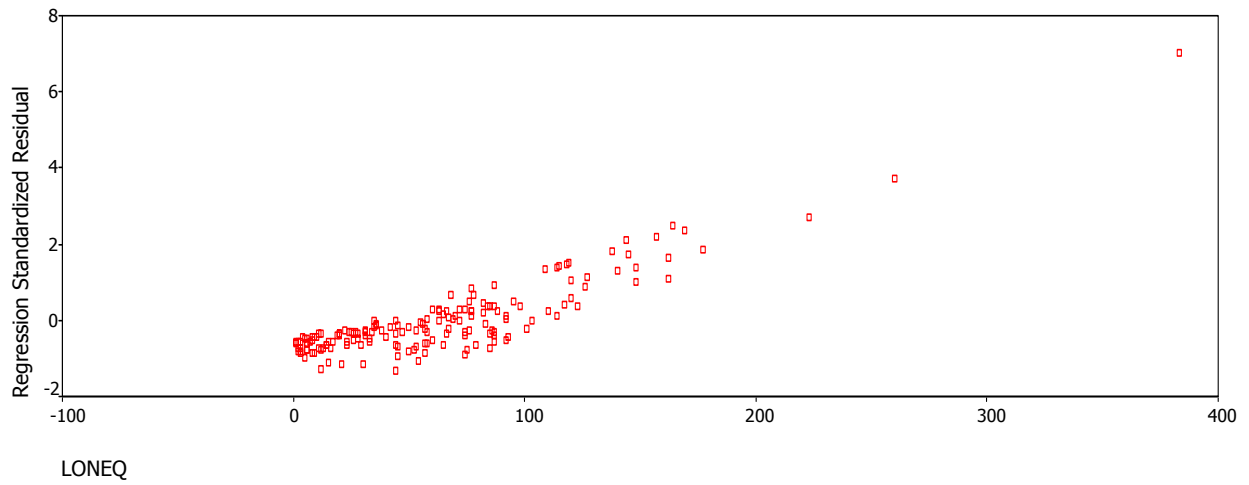
Normal P-P Plot of Regression Standardized Residual

Dependent Variable: LONEQ

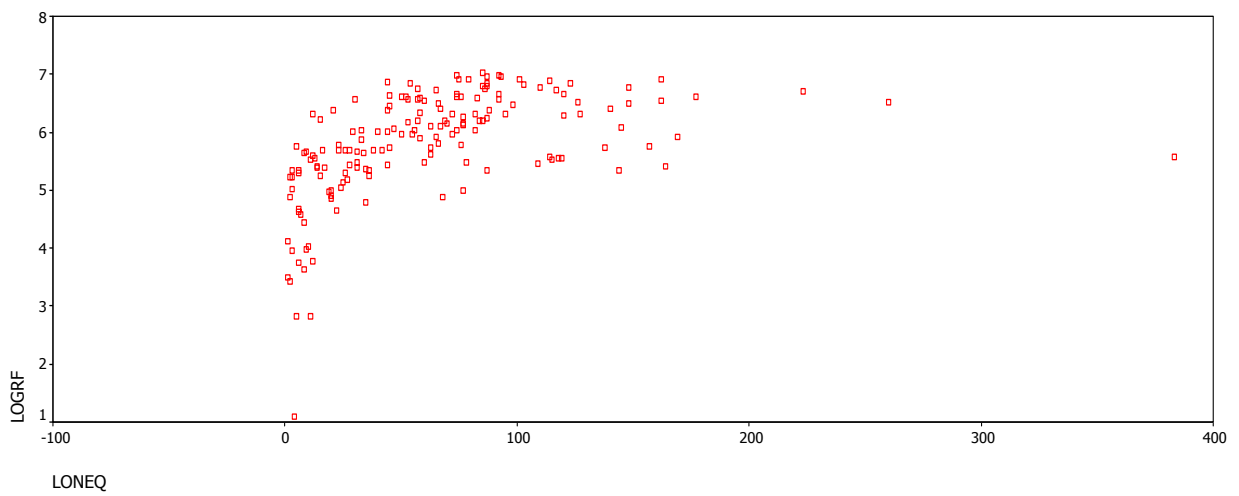
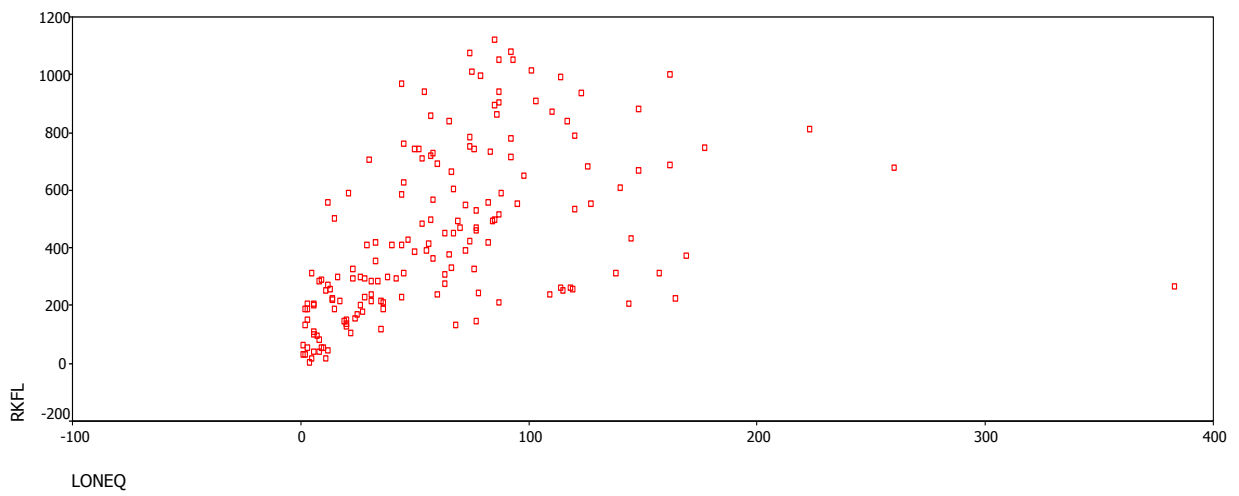
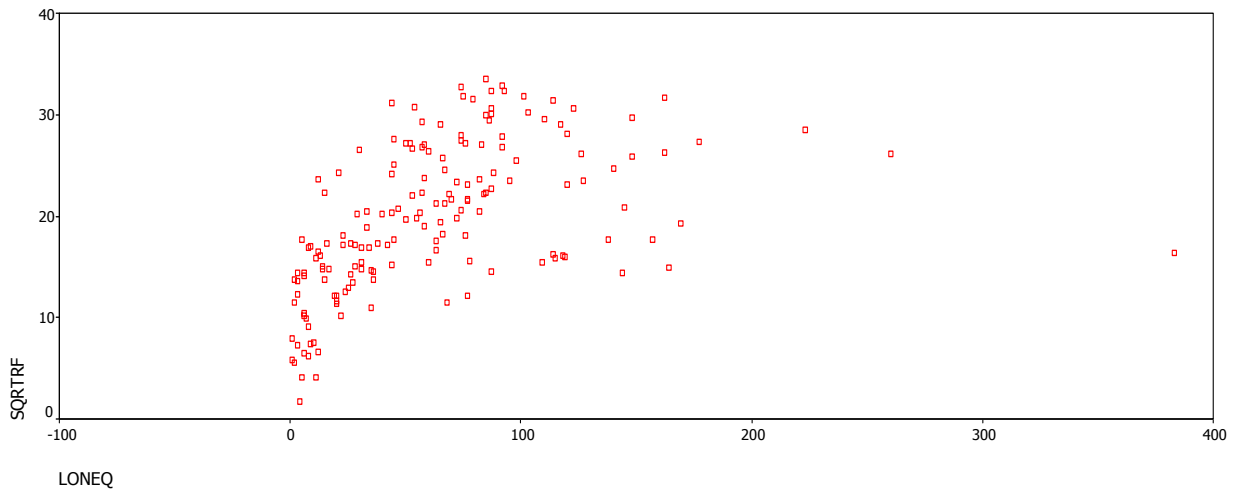


Scatterplot

Dependent Variable: LONEQ



Graph



# Correlations

### Correlations

		LONEQ	RKFL
LONEQ	Pearson Correlation	1	.459**
	Sig. (2-tailed)	.	.000
	N	167	167
RKFL	Pearson Correlation	.459**	1
	Sig. (2-tailed)	.000	.
	N	167	167

\*\* . Correlation is significant at the 0.01 level

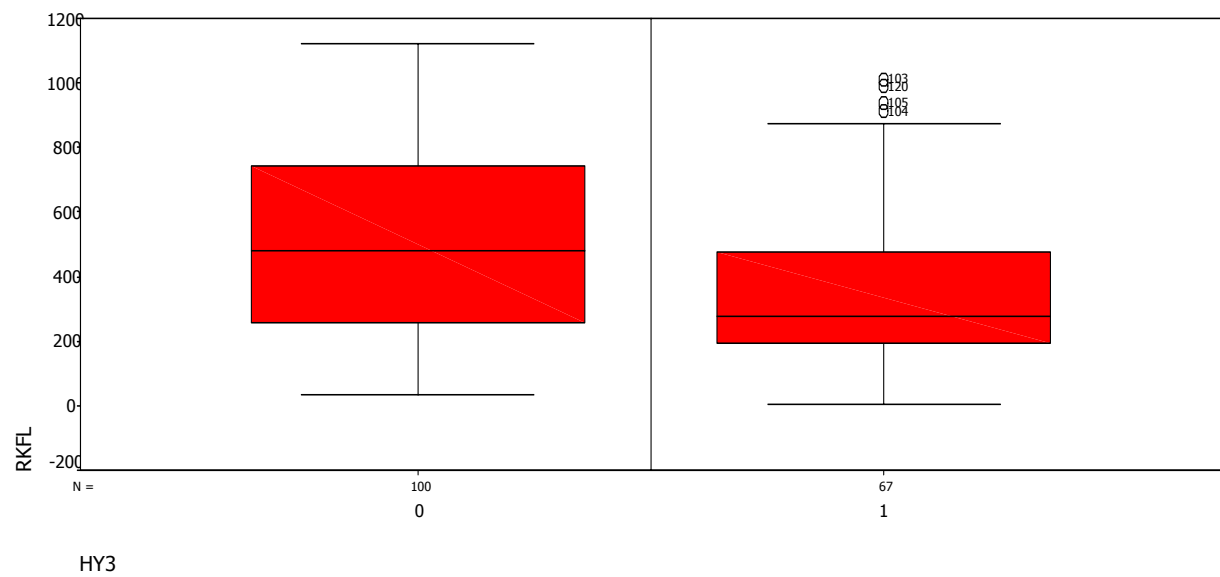
### Correlations

		LONEQ	SQRTRF
LONEQ	Pearson Correlation	1	.488
	Sig. (2-tailed)	.	.000
	N	167	167
SQRTRF	Pearson Correlation	.488	1
	Sig. (2-tailed)	.000	.
	N	167	167

### Correlations

		LONEQ	LOGRF
LONEQ	Pearson Correlation	1	.479
	Sig. (2-tailed)	.	.000
	N	167	167
LOGRF	Pearson Correlation	.479	1
	Sig. (2-tailed)	.000	.
	N	167	167

# HY3 and RKFL



## HY3

Case Processing Summary

		Cases					
		Valid		Missing		Total	
		N	Percent	N	Percent	N	Percent
RKFL	0	100	100.0%	0	.0%	100	100.0%
	1	67	95.7%	3	4.3%	70	100.0%

### Descriptives

HY3				Statistic	Std. Error
RKFL	0	Mean		502.53	29.833
		95% Confidence Interval for Mean	Lower Bound	443.34	
			Upper Bound	561.72	
		5% Trimmed Mean		496.48	
		Median		478.50	
		Variance		88998.332	
		Std. Deviation		298.326	
		Minimum		31	
		Maximum		1120	
		Range		1089	
		Interquartile Range		488.25	
		Skewness		.271	.241
		Kurtosis		-.954	.478
	1	Mean		360.04	31.233
		95% Confidence Interval for Mean	Lower Bound	297.69	
			Upper Bound	422.40	
		5% Trimmed Mean		345.13	
		Median		277.00	
		Variance		65360.165	
		Std. Deviation		255.656	
		Minimum		3	
		Maximum		1012	
		Range		1009	
		Interquartile Range		328.00	
		Skewness		1.009	.293
		Kurtosis		.214	.578

# RKFL

## Stem-and-Leaf Plots

### RKFL Stem-and-Leaf Plot for HY3= 0

Frequency	Stem & Leaf
8.00	0 . 33345689
8.00	1 . 00234458
17.00	2 . 00011234556889999
6.00	3 . 011359
16.00	4 . 0011225566789999
9.00	5 . 033455689
5.00	6 . 01579
13.00	7 . 0011344456788
6.00	8 . 144689
5.00	9 . 03469
6.00	10 . 015577
1.00	11 . 2

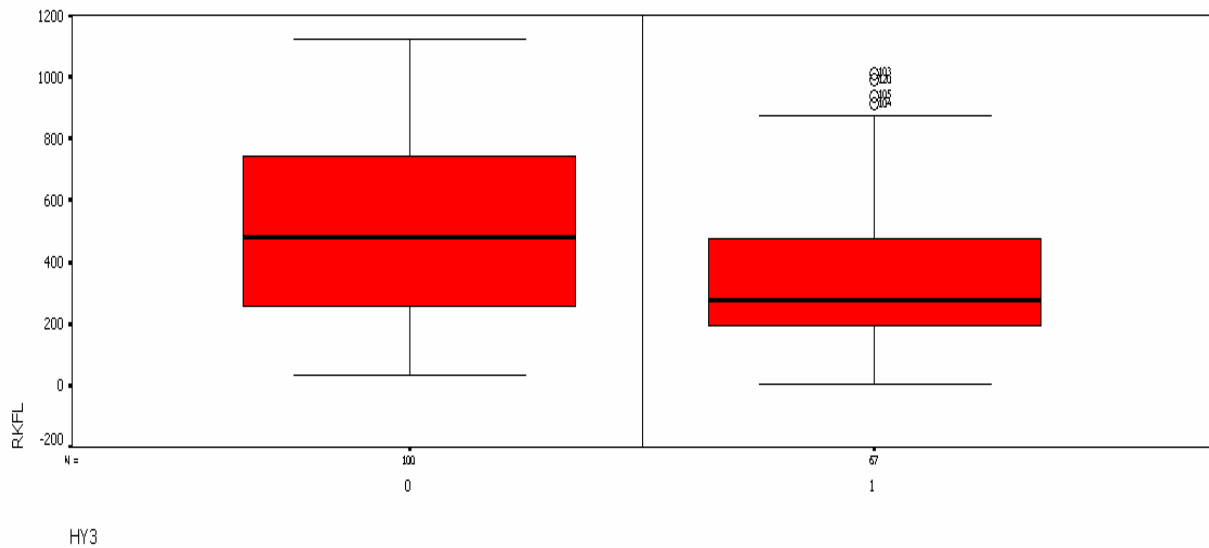
Stem width: 100  
Each leaf: 1 case(s)

### RKFL Stem-and-Leaf Plot for HY3= 1

Frequency	Stem & Leaf
6.00	0 . 011455
11.00	1 . 01334568888
21.00	2 . 000112223345566778899
9.00	3 . 112267789
3.00	4 . 113
4.00	5 . 1558
5.00	6 . 26888
2.00	7 . 24
2.00	8 . 57
4.00	Extremes (>=911)

Stem width: 100  
Each leaf: 1 case(s)





## Oneway

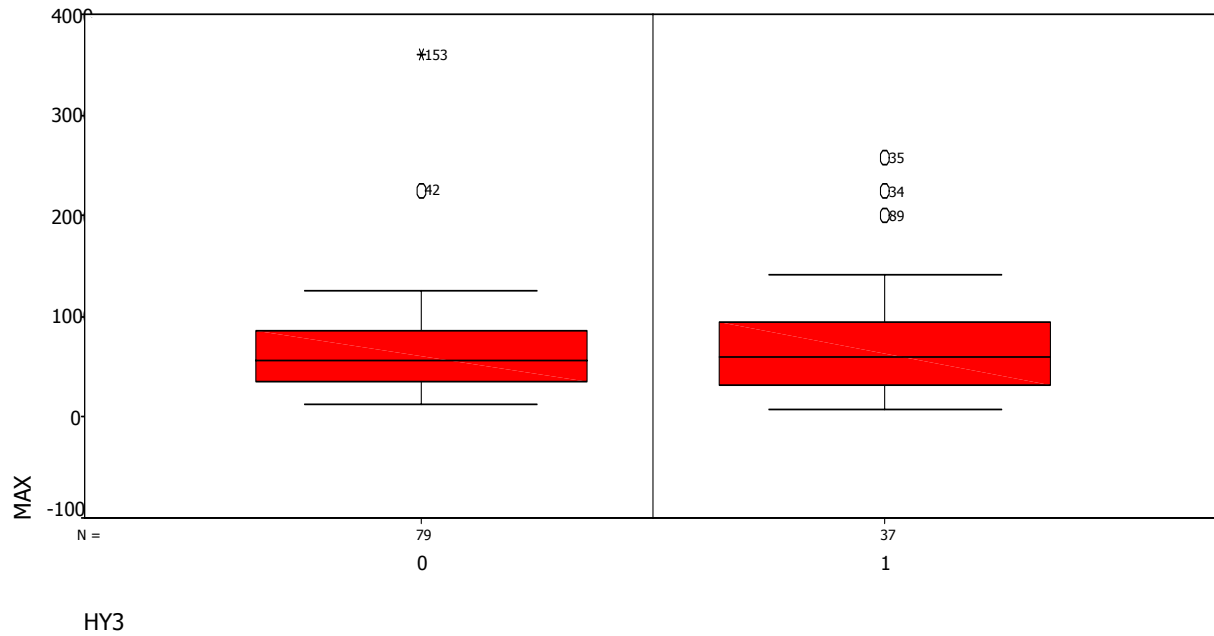
### ANOVA

RKFL					
	Sum of Squares	df	Mean Square	F	Sig.
Between Groups	814512.9	1	814512.943	10.240	.002
Within Groups	13124606	165	79543.065		
Total	13939119	166			

## HY3 and MAX

### Case Processing Summary

		Cases					
		Valid		Missing		Total	
		N	Percent	N	Percent	N	Percent
MAX	0	79	79.0%	21	21.0%	100	100.0%
	1	37	52.9%	33	47.1%	70	100.0%



## T-Test

### Group Statistics

	HY3	N	Mean	Std. Deviation	Std. Error Mean
RKFL	1	67	360.04	255.656	31.233
	0	100	502.53	298.326	29.833

### Independent Samples Test

		Levene's Test for Equality of Variances		t-test for Equality of Means						
		F	Sig.	t	df	Sig. (2-tailed)	Mean Difference	Std. Error Difference	95% Confidence Interval of the Difference	
RKFL	Equal variances assumed	3.859	.051	-3.200	165	.002	-142.49	44.527	-230.401	-54.569
	Equal variances not assumed			-3.299	155.226	.001	-142.49	43.192	-227.804	-57.166

# T-Test

**Group Statistics**

	HY3	N	Mean	Std. Deviation	Std. Error Mean
MAX	1	37	734.92	594.094	97.668
	0	79	662.62	489.360	55.057

**Independent Samples Test**

		Levene's Test for Equality of Variances		t-test for Equality of Means						
		F	Sig.	t	df	Sig. (2-tailed)	Mean Difference	Std. Error Difference	95% Confidence Interval of the Difference	
									Lower	Upper
MAX	Equal variances assumed	2.697	.103	.692	114	.491	72.30	104.526	-134.766	279.363
	Equal variances not assumed			.645	59.731	.521	72.30	112.118	-151.991	296.589

# T-Test

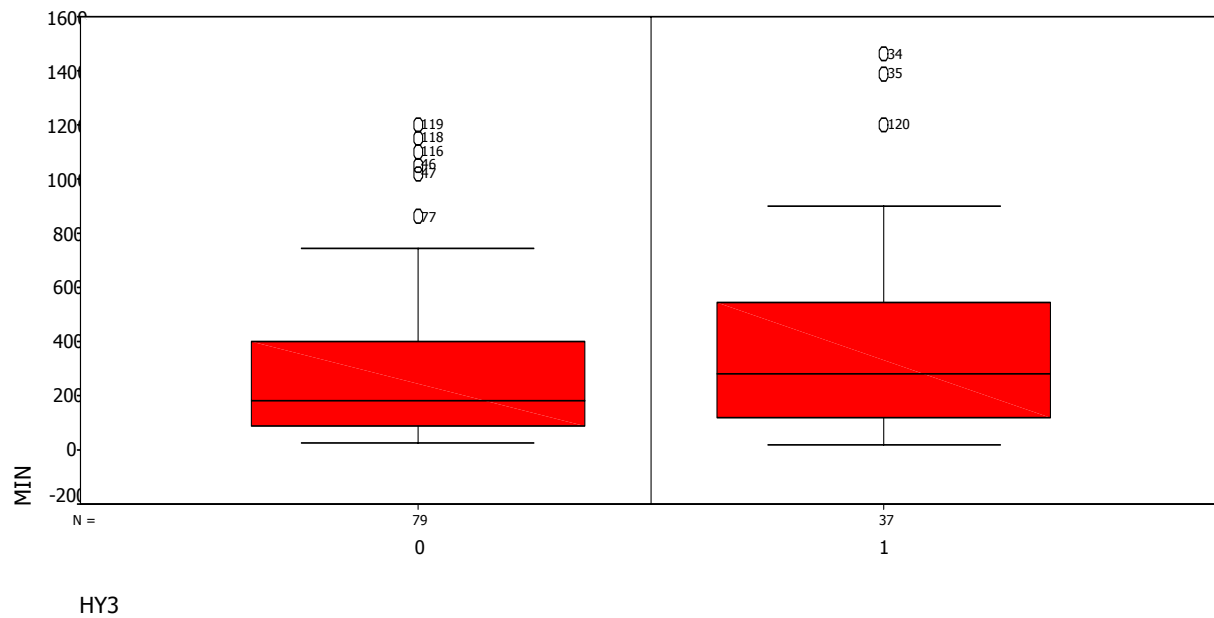
**Group Statistics**

	HY3	N	Mean	Std. Deviation	Std. Error Mean
MIN	1	37	408.59	369.763	60.789
	0	79	295.91	281.165	31.634

**Independent Samples Test**

		Levene's Test for Equality of Variances		t-test for Equality of Means						
		F	Sig.	t	df	Sig. (2-tailed)	Mean Difference	Std. Error Difference	95% Confidence Interval of the Difference	
									Lower	Upper
MIN	Equal variances assumed	3.427	.067	1.814	114	.072	112.68	62.129	-10.394	235.760
	Equal variances not assumed			1.644	56.234	.106	112.68	68.527	-24.580	249.946

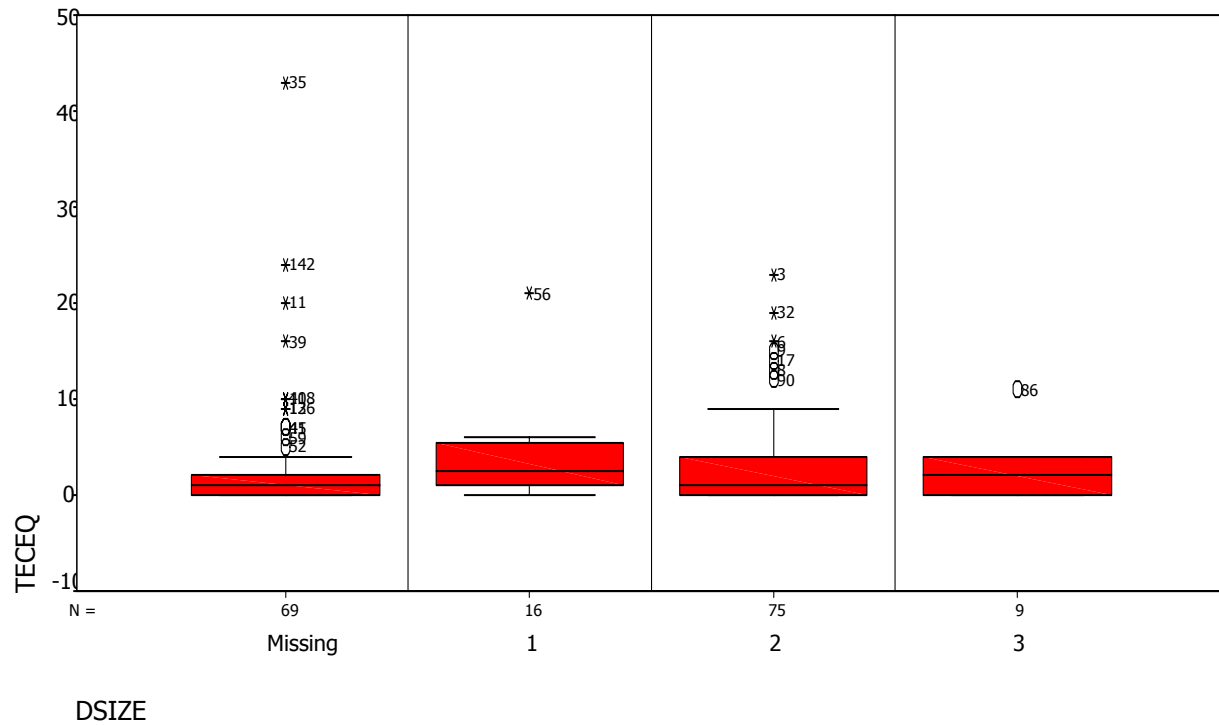
## HY3 and MIN



## DSIZE and TECEQ

Case Processing Summary

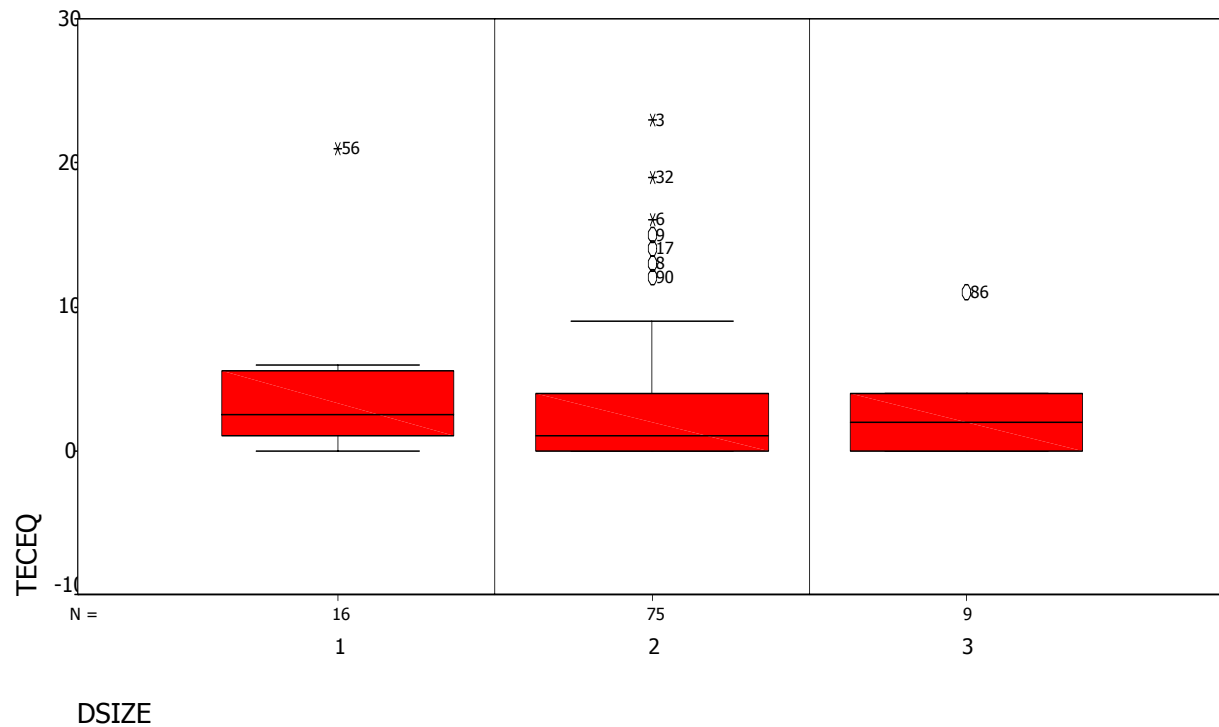
DSIZE		Cases					
		Valid		Missing		Total	
		N	Percent	N	Percent	N	Percent
TECEQ	.(Missing)	69	98.6%	1	1.4%	70	100.0%
	1	16	100.0%	0	.0%	16	100.0%
	2	75	100.0%	0	.0%	75	100.0%
	3	9	100.0%	0	.0%	9	100.0%



## DSIZE and TECEQ

Case Processing Summary

		Cases					
		Valid		Missing		Total	
		N	Percent	N	Percent	N	Percent
TECEQ	1	16	100.0%	0	.0%	16	100.0%
	2	75	100.0%	0	.0%	75	100.0%
	3	9	100.0%	0	.0%	9	100.0%



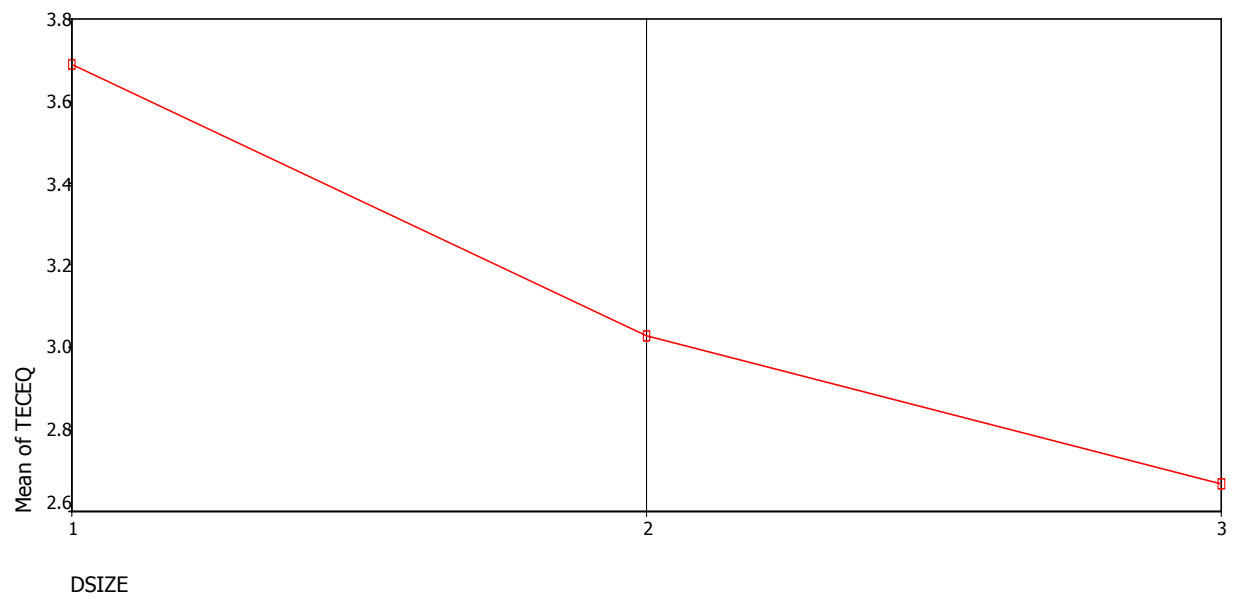
## Oneway

### Descriptives

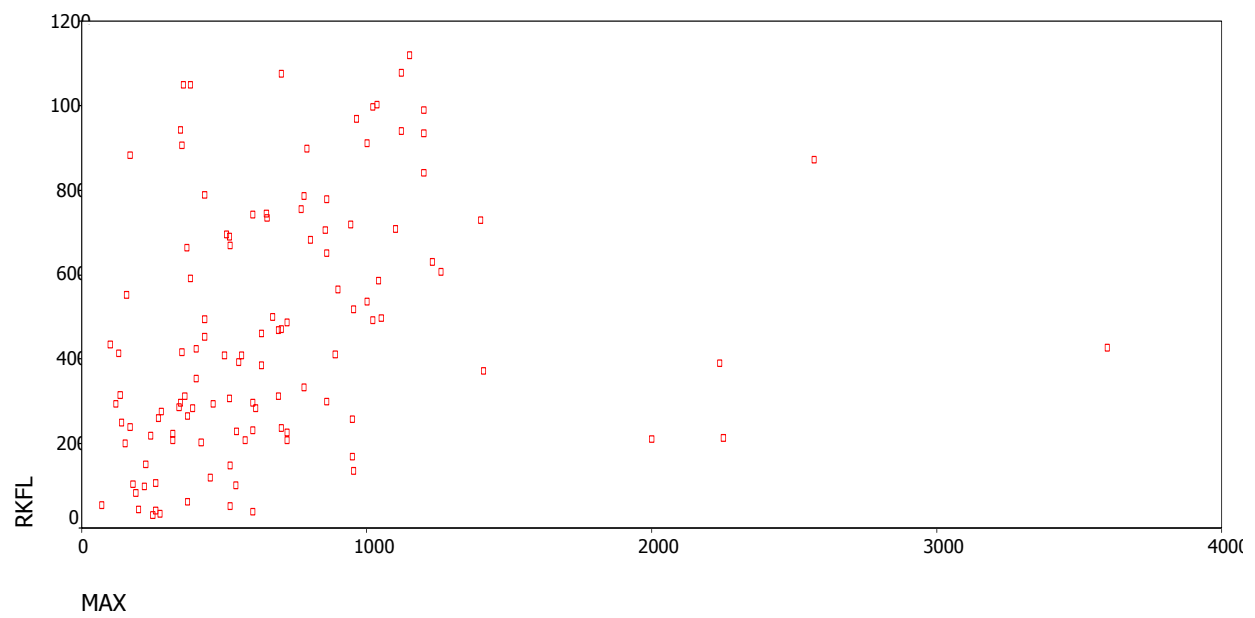
TECEQ								
	N	Mean	Std. Deviation	Std. Error	95% Confidence Interval for Mean		Minimum	Maximum
					Lower Bound	Upper Bound		
1	16	3.69	5.108	1.277	.97	6.41	0	21
2	75	3.03	4.779	.552	1.93	4.13	0	23
3	9	2.67	3.500	1.167	-.02	5.36	0	11
Total	100	3.10	4.700	.470	2.17	4.03	0	23

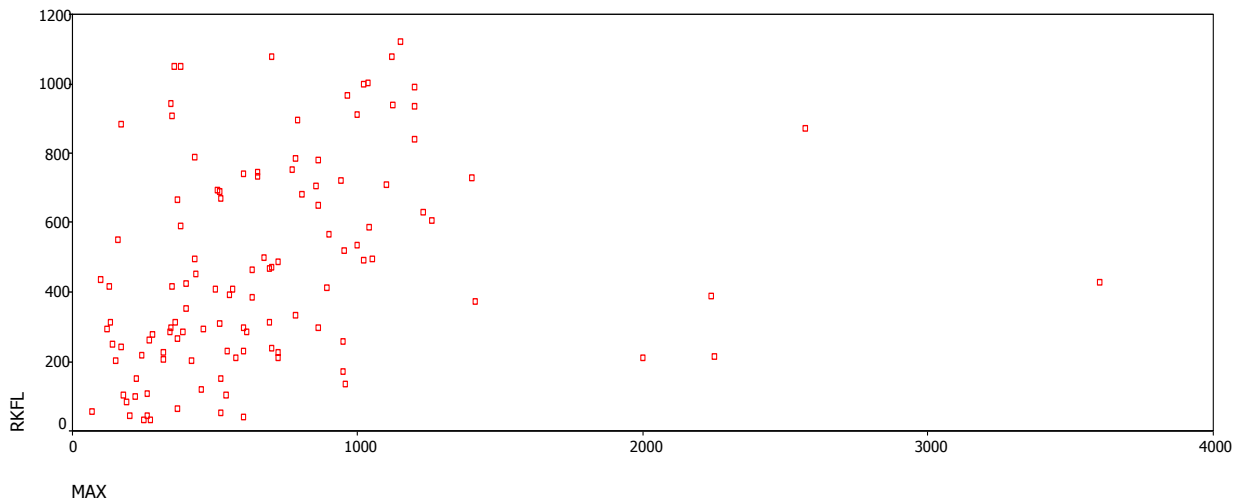
### ANOVA

TECEQ					
	Sum of Squares	df	Mean Square	F	Sig.
Between Groups	7.616	2	3.808	.169	.844
Within Groups	2179.384	97	22.468		
Total	2187.000	99			



## Graph





# Regression

**Variables Entered/Removed<sup>a</sup>**

Model	Variables Entered	Variables Removed	Method
1	MAX <sup>a</sup>	.	Enter

a. All requested variables entered.

b. Dependent Variable: RKFL

**Model Summary<sup>b</sup>**

Model	R	R Square	Adjusted R Square	Std. Error of the Estimate
1	.290 <sup>a</sup>	.084	.076	284.775

a. Predictors: (Constant), MAX

b. Dependent Variable: RKFL

**ANOVA<sup>b</sup>**

Model		Sum of Squares	df	Mean Square	F	Sig.
1	Regression	841385.2	1	841385.192	10.375	.002 <sup>a</sup>
	Residual	9163953	113	81096.927		
	Total	10005338	114			

a. Predictors: (Constant), MAX

b. Dependent Variable: RKFL



**Coefficients<sup>a</sup>**

Model	Unstandardized Coefficients		Standardized Coefficients	t	Sig.
	B	Std. Error	Beta		
1 (Constant)	353.986	43.998		8.045	.000
MAX	.164	.051	.290	3.221	.002

a. Dependent Variable: RKFL

**Residuals Statistics<sup>a</sup>**

	Minimum	Maximum	Mean	Std. Deviation	N
Predicted Value	365.46	943.99	466.98	85.910	115
Residual	-516.99	637.83	.00	283.523	115
Std. Predicted Value	-1.182	5.552	.000	1.000	115
Std. Residual	-1.815	2.240	.000	.996	115

a. Dependent Variable: RKFL

## CHARTS

### HY2 and EXPL2

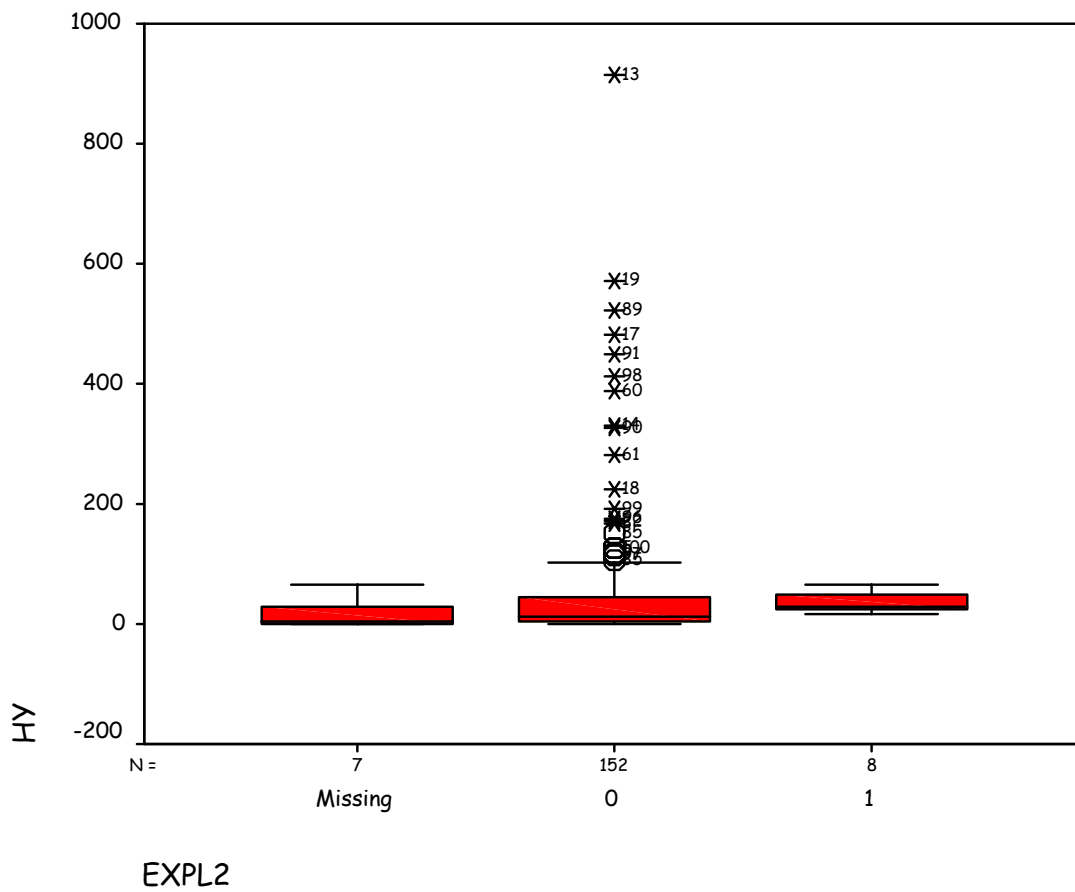
**Case Processing Summary**

		Cases					
		Valid		Missing		Total	
		N	Percent	N	Percent	N	Percent
EXPL2	0	104	95.4%	5	4.6%	109	100.0%
	1	58	95.1%	3	4.9%	61	100.0%

### HY and EXPL2

**Case Processing Summary**

		Cases					
		Valid		Missing		Total	
		N	Percent	N	Percent	N	Percent
HY	. (Missing)	7	87.5%	1	12.5%	8	100.0%
	0	152	98.7%	2	1.3%	154	100.0%
	1	8	100.0%	0	.0%	8	100.0%



Case Processing Summary

		Cases					
		Valid		Missing		Total	
	EXPL2	N	Percent	N	Percent	N	Percent
HY	0	152	98.7%	2	1.3%	154	100.0%
	1	8	100.0%	0	.0%	8	100.0%

### Descriptives

EXPL2				Statistic	Std. Error
HY	0	Mean		57.53	10.130
		95% Confidence Interval for Mean	Lower Bound	37.51	
			Upper Bound	77.54	
		5% Trimmed Mean		35.11	
		Median		12.50	
		Variance		15596.913	
		Std. Deviation		124.888	
		Minimum		0	
		Maximum		916	
		Range		916	
		Interquartile Range		40.00	
		Skewness		3.921	.197
		Kurtosis		18.442	.391
1		Mean		35.88	6.113
		95% Confidence Interval for Mean	Lower Bound	21.42	
			Upper Bound	50.33	
		5% Trimmed Mean		35.36	
		Median		29.00	
		Variance		298.982	
		Std. Deviation		17.291	
		Minimum		15	
		Maximum		66	
		Range		51	
		Interquartile Range		27.00	
		Skewness		.696	.752
		Kurtosis		-.527	1.481

## Stem-and-Leaf Plots

**HY**

### HY Stem-and-Leaf Plot for EXPL2= 0

Frequency	Stem & Leaf
67.00	0 . 00011122233334555566666777888999
26.00	1 . 00123567789
12.00	2 . 045&&
5.00	3 . &&
10.00	4 . 56&&&
2.00	5 . &
2.00	6 . &
4.00	7 . 1&
2.00	8 . &
.00	9 .
1.00	10 . &
21.00	Extremes (>=106)

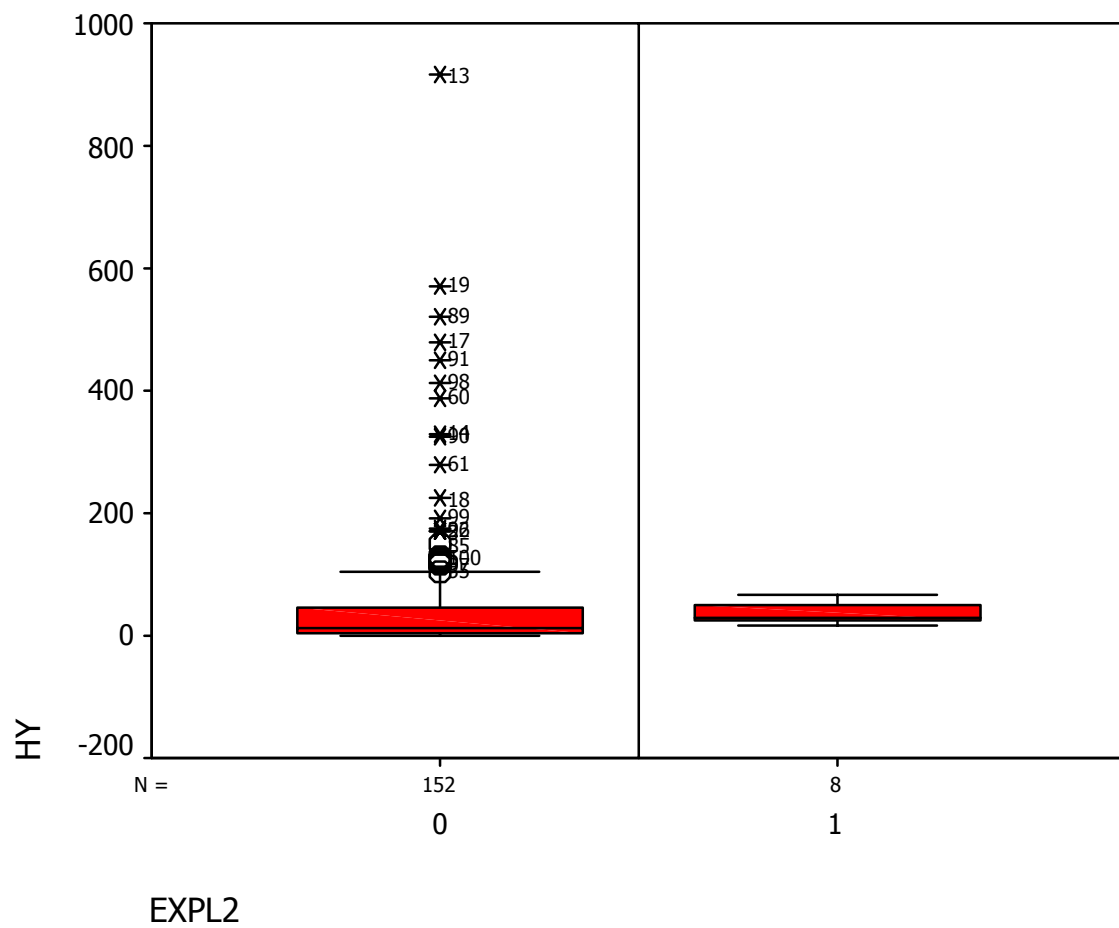
Stem width: 10  
Each leaf: 2 case(s)

& denotes fractional leaves.

### HY Stem-and-Leaf Plot for EXPL2= 1

Frequency	Stem & Leaf
6.00	0 . 122224
2.00	0 . 56

Stem width: 100  
Each leaf: 1 case(s)



## Crosstabs

Case Processing Summary

	Cases					
	Valid		Missing		Total	
	N	Percent	N	Percent	N	Percent
EXPL2 * HY3	162	95.3%	8	4.7%	170	100.0%

### EXPL2 \* HY3 Crosstabulation

			HY3		Total
			0	1	
EXPL2	0	Count	95	59	154
		Expected Count	91.3	62.7	154.0
	1	Count	1	7	8
		Expected Count	4.7	3.3	8.0
Total		Count	96	66	162
		Expected Count	96.0	66.0	162.0

### Chi-Square Tests

	Value	df	Asymp. Sig. (2-sided)	Exact Sig. (2-sided)	Exact Sig. (1-sided)
Pearson Chi-Square	7.621 <sup>b</sup>	1	.006	.008	.008
Continuity Correction <sup>a</sup>	5.720	1	.017		
Likelihood Ratio	7.968	1	.005	.022	.008
Fisher's Exact Test				.008	.008
N of Valid Cases	162				

a. Computed only for a 2x2 table

b. 2 cells (50.0%) have expected count less than 5. The minimum expected count is 3.26.

## Bibliography

- Abrams, M., 2000, The Advanced Spaceborne Thermal Emission and Reflection Radiometer (ASTER): data products for the high spatial resolution imager on NASA's Terra platform: *Int. J. Remote Sensing*, v. 21, p. 847-859.
- Abrams, M., Glaze, L.S., and Sheridan, M., 1991, Monitoring Colima Volcano, Mexico, using satellite data: *Bull Volcanol*, v. 53, p. 571-574.
- Abrams, M., and Hook, S.J., 1995, Simulated ASTER data for geologic studies.: *IEEE Transactions on Geoscience and Remote Sensing*, v. 33, p. 692-699.
- Adams, J., Smith, M., and Gillespie, A.R., 1993, Imaging spectroscopy: Interpretation based on spectral mixture analysis, *in* Pieters, C., and Englert, P., eds., *Remote Geochemical Analysis: Elemental and Mineralogical Composition*: New York, Cambridge University Press.
- Anderson, S.W., and Fink, J.H., 1990, The development and distribution of lava textures at the Mount St. Helens dome, *in* Fink, J.H., ed., *Lava flows and domes: emplacement mechanisms and hazard implications*, Volume 2, *IAVCEI Proc Volcanol*, p. 25-46.
- Aspinall, W.P., Loughlin, S., Michael, F.V., Miller, A., Norton, G., Rowley, K.C., Sparks, R.S.J., and Young, S.R., 2002, The Montserrat Volcano Observatory: its evolution, organization, role, and activities, *in* Druitt, T.H., and Kokelaar, B.P., eds., *The Eruption of Soufriere Hills Volcano, Montserrat, from 1995 to 1999*, Volume 21: London, Geological Society, p. 71-91.
- CALIPSO, 2003, Caribbean Andesite Lava Island-volcano Precision Seismo-geodetic Observatory, Volume 2003.
- Cole, P.D., Calder, E.S., Druitt, T.H., Hoblitt, R., Robertson, R., and Sparks, R.S.J., 1998, Pyroclastic flows generated by gravitational instability of the 1996-97 lava dome of Soufriere Hills Volcano, Montserrat: *Geophysical Research Letters*, v. 25, p. 3425-3428.
- De La Cruz-Reyna, S., Meli P., R., and Quass W., R., 2000, *Volcanic Crisis Management*: San Diego, Academic Press, 1417 p.
- Dozier, J., 1981, A Method for Satellite Identification of Surface Temperature Fields of Subpixel Resolution: *Remote Sens. Environ.*, v. 11, p. 221-229.
- Eichelberger, J.C., Carrigan, C.R., Westrich, H.R., and Price, R.H., 1986, Non-explosive silicic volcanism: *Nature*, v. 323, p. 598-602.

- Elsworth, D., and Voight, B., 2001, The mechanics of harmonic gas pressurization and failure of lava domes: *Geophysical Journal International*, v. 145, p. 187.
- Fink, J.H., and Anderson, S.W., 2000, *Lava Domes and Coulees*: San Diego, Academic Press, 1417 p.
- Fink, J.H., Anderson, S.W., and Manley, C.R., 1992, Textural Constraints on Effusive Silicic Volcanism: Beyond the Permeable Foam Model: *Journal of Geophysical Research*, v. 97, p. 9073-9083.
- Fink, J.H., Malin, M.C., and Anderson, S.W., 1990, Intrusive and Extrusive Growth of the Mount St. Helens Lava Dome: *Nature*, v. 348, p. 435.
- Fink, J.H., and Manley, C.R., 1987, Origin of pumiceous and glassy textures in rhyolite flows and domes, *in* Fink, J.H., ed., *The emplacement of silicic domes and lava flows*, Volume 212, Geological Society of America Special Papers, p. 77-88.
- Flynn, L.P., Harris, A.J.L., and Wright, R., 2001, Improved identification of volcanic features using Landsat 7 ETM +: *Remote Sens. Environ.*, v. 78, p. 180-193.
- Formenti, Y., and Druitt, T.H., 2003, Vesicle connectivity in pyroclastics and implications for the fluidisation of fountain-collapse pyroclastic flows, Montserrat (West Indies): *Earth and Planetary Science Letters*, v. 214, p. 561-574.
- Gillespie, A.R., 1992, Spectral mixture analysis of multispectral thermal infrared images: *Remote Sens. Environ.*, v. 42, p. 137-145.
- Gillespie, A.R., Rokugawa, S., Hook, S.J., Matsunaga, T., and Kahle, A.B., 1999, Temperature/Emissivity Separation Algorithm Theoretical Basis Document, Version 2.4, NASA Contract, p. 1-64.
- Glaze, L.S., Francis, P.W., and Rothery, D.A., 1989, Measuring thermal budgets of active volcanoes by satellite remote sensing: *Nature*, v. 338, p. 144-146.
- GOES, 2001, GOES-N/Q Project Brochure, Volume 2003, NASA Goddard Space Flight Center.
- Harris, A.J.L., Flynn, L.P., Dean, K.G., Pilger, E., Wooster, M., Okubu, C., Mougini-Mark, P., Garbeil, H., Thornber, C., De La Cruz-Reyna, S., Rothery, D.A., and Wright, R., 2000, Real-time monitoring of volcanic hot spots with satellites: *Remote Sensing of Active Volcanism*, AGU Geophysical Monograph Series, v. 116, p. 139-159.



- Harris, A.J.L., Flynn, L.P., Keszthelyi, P.J., Mougini-Mark, P., Rowland, S.K., and Resing, J.A., 1998, Calculation of lava effusion rates from Landsat TM data: *Bull Volcanol*, v. 60, p. 52-71.
- Harris, A.J.L., Flynn, L.P., Rothery, D.A., Oppenheimer, C., and Sherman, S., 1999, Mass flux measurements at active lava lakes: implications for magma recycling: *Journal of Geophysical Research*, v. 104, p. 7117-7136.
- Harris, A.J.L., Pilger, E., and Flynn, L.P., 2001a, Web-Based Hot Spot Monitoring using GOES: What it is and How it Works: *Advances in Environmental Monitoring and Modelling*, v. 1, p. 3-31.
- Kahle, A.B., and Alley, R.E., 1992, Separation of Temperature and Emittance in Remotely Sensed Radiance Measurements: *Remote Sens. Environ.*, p. 107-111.
- Kahle, A.B., Palluconi, F.D., Hook, S.J., Realmuto, V.J., and Bothwell, G., 1991, The Advanced Spaceborne Thermal Emission and Reflectance Radiometer (ASTER): *International Journal of Imaging Systems and Technology*, v. 3, p. 144-156.
- Kaneko, T., Wooster, M., and Nakada, S., 2002, Exogenous and endogenous growth of the Unzen lava dome examined by satellite infrared image analysis: *Journal of Volcanology and Geothermal Research*, v. 116, p. 151-160.
- Kearey, P., and Vine, F., 1996, *Global Tectonics*: Malden, Blackwell Science Ltd, 333 p.
- Kokelaar, B.P., 2002, Setting, chronology and consequences of the eruption of Soufriere Hills Volcano, Montserrat (1995-1999), *in* Druitt, T.H., and Kokelaar, B.P., eds., *The Eruption of Soufriere Hills Volcano, Montserrat, from 1995 to 1999, Volume 21*: London, Geological Society, p. 1-43.
- Kuhn, S., and Ramsey, M.S., 2002, Monitoring the Surface Changes and Growth of the Soufriere Hills Lava Dome: Thermal Infrared Analysis of Field and Spaceborne Data, *American Geophysical Union Fall Meeting, Volume abs. V12A-1407*.
- Lockett, R., Baptie, B., and Neuberg, J., 2002, The relationship between degassing and rockfall signals at Soufriere Hills Volcano, Montserrat, *in* Druitt, T.H., and Kokelaar, B.P., eds., *The Eruption of Soufriere Hills Volcano, Montserrat, from 1995-1999, Volume 21: Memoirs*: London, Geological Society, p. 595-602.
- Lyon, R., 1965, Analysis of rocks by spectral infrared emission (8 to 25 microns): *Economic Geology*, v. 60, p. 715-736.

- MacGregor, A.G., 1938, The Royal Society expedition to Montserrat, B.W.I.. The volcanic history and petrology of Montserrat with observations on Mt. Pelee in Martinique.: Philosophical Transactions of the Royal Society, London, v. B229, p. 1-90.
- Menand, T., and Tait, S., 2001, A phenomenological model for precursor volcanic eruptions: Nature, p. 678-680.
- Miller, A., Stewart, R., White, R., Lockett, R., Baptie, B., Aspinall, W.P., Latchman, J., and Voight, B., 1998, Seismicity associated with dome growth and collapse at the Soufriere Hills Volcano, Montserrat: Geophysical Research Letters, v. 25, p. 3401-3404.
- Moersch, J., and Christensen, P.R., 1995, Thermal emission from particulate surfaces: A comparison of scattering models with measured spectra: Journal of Geophysical Research, v. 100, p. 7465-7477.
- Nakada, S., 2000, Hazards from Pyroclastic Flows and Surges: San Diego, Academic Press, 1417 p.
- Neuberg, J., Baptie, B., Lockett, R., and Stewart, R., 1998, Results from the broadband seismic network on Montserrat: Geophysical Research Letters, v. 25, p. 3661-3664.
- Neuberg, J., Lockett, R., Baptie, B., and Olsen, K., 2000, Models of tremor and low-frequency earthquake swarms on Montserrat: J. Volcanol. Geotherm. Res., p. 83-104.
- Oppenheimer, C., 1998, Volcanological applications of meteorological satellites: Int. J. Remote Sensing, v. 19, p. 2829-2864.
- Perret, F.A., 1939, The volcano-seismic crisis at Montserrat, 1933-37: Publications of the Carnegie Institute, Washington, v. 512, p. 1-76.
- Ramsey, M.S., and Christensen, P.R., 1998, Mineral abundance determination: Quantitative deconvolution of thermal emission spectra: Journal of Geophysical Research, v. 103, p. 577-596.
- Ramsey, M.S., and Dehn, J., 2003, Spaceborne observations of the 2000 Bezymainny, Kamchatka eruption: The integration of high-resolution ASTER data into a near real-time monitoring using AVHRR: J. Volcanol. Geotherm. Res.

- Ramsey, M.S., and Fink, J.H., 1994, Remote monitoring of volcanic domes: detection of chemical, textural, and thermal heterogeneities: EOS Trans Am Geophys Union, v. 75.
- Ramsey, M.S., and Fink, J.H., 1999, Estimating silicic lava vesicularity with thermal remote sensing: a new technique for volcanic mapping and monitoring: Bull Volcanol, p. 32-39.
- Roobol, M.J., and Smith, A.L., 1998, Pyroclastic stratigraphy of the Soufriere Hills volcano, Montserrat - Implications for the present eruption: Geophysical Research Letters, v. 25, p. 3393-3396.
- Sabins, F., 1996, Remote sensing: principles and interpretation: New York, W. H. Freeman and Company, 494 p.
- Salisbury, J.W., and D'Aria, D.M., 1992, Emissivity of Terrestrial Materials in the 8-14 um Atmospheric Window: Remote Sens. Environ., p. 83-106.
- Salisbury, J.W., and Walter, L., 1989, Thermal Infrared (2.5-13.5 um) Spectroscopic Remote Sensing of Igneous Rock Types on Particulate Planetary Surfaces: Journal of Geophysical Research, v. 94, p. 9192-9202.
- Salisbury, J.W., Walter, L., Vergo, N., and D'Aria, D.M., Infrared (2.1-25 um) Spectra of Minerals: Baltimore, The Johns Hopkins University Press.
- Schmugge, T., Hook, S.J., and Coll, C., 1998, Recovering Surface Temperature and Emissivity from Thermal Infrared Multispectral Data: Remote Sens. Environ., p. 121-131.
- Shepherd, J.B., Tomblin, J.F., and Woo, D.A., 1971, Volcano-seismic crisis in Montserrat, West Indies, 1966-67: Bull Volcanol, v. 35, p. 143-163.
- Siegal, B., and Gillespie, A.R., 1980, Remote Sensing in Geology: New York, John Wiley and Sons, Inc., 702 p.
- Sigurdsson, H., and Carey, S., 1991, Caribbean Volcanoes: A Field Guide, Geological Association of Canada, Mineralogical Association of Canada, Society of Economic Geologists, Joint Annual Meeting: Field Trip B1: Guidebook: Toronto, Geological Association of Canada, p. 101.
- Small, C., and Naumann, T., 2001, Holocene Volcanism and the Global Distribution of Human Population: Environmental Hazards, v. 3, p. 93-109.

- Sparks, Murphy, Lejeune, Watts, Barclay, and Young, 2000, Control on the Emplacement of the andesite lava dome of the Soufriere Hills volcano, Montserrat by degassing-induced crystallization: *Terra Nova*, v. 12, p. 14.
- Sparks, R.S.J., and Young, S.R., 2002, The eruption of Soufriere Hills Volcano, Montserrat (1995-1999): overview of scientific results, *in* Druitt, T.H., and Kokelaar, B.P., eds., *The Eruption of Soufriere Hills Volcano, Montserrat, from 1995 to 1999*, Volume 21: London, Geological Society, p. 45-69.
- Tilling, R.I., 1989, *Volcanic Hazards*: Washington D.C., American Geophysical Union, 123 p.
- White, R., Miller, A., Lynch, L.L., Power, J., and Staff, M., 1998, Observations of hybrid seismic events at Soufriere Hills volcano, Montserrat: *Geophysical Research Letters*, v. 25, p. 3657-3660.
- Yamaguchi, Y., Kahle, A.B., Tsu, H., Kawakami, T., and Pniel, M., 1998, Overview of Advanced Spaceborne Thermal Emission and Reflection Radiometer (ASTER): *IEEE Transactions on Geoscience and Remote Sensing*, v. 36, p. 1062-1071.
- Young, S.R., Sparks, R.S.J., Aspinall, W.P., Lynch, L.L., Miller, A., Robertson, R., and Shepherd, J.B., 1998, Overview of the eruption of Soufriere Hills volcano, Montserrat, 18 July 1995 to December 1997: *Geophysical Research Letters*, v. 25, p. 3389-3392.